



**HAL**  
open science

# Design and control of a new pulsating power decoupling circuit for grid-connected photovoltaic systems

Elaheh Heydari

► **To cite this version:**

Elaheh Heydari. Design and control of a new pulsating power decoupling circuit for grid-connected photovoltaic systems. Electric power. Université Paris-Saclay; Tarbiat Modares university (Téhéran), 2022. English. NNT: 2022UPAST004 . tel-03663415

**HAL Id: tel-03663415**

**<https://theses.hal.science/tel-03663415>**

Submitted on 10 May 2022

**HAL** is a multi-disciplinary open access archive for the deposit and dissemination of scientific research documents, whether they are published or not. The documents may come from teaching and research institutions in France or abroad, or from public or private research centers.

L'archive ouverte pluridisciplinaire **HAL**, est destinée au dépôt et à la diffusion de documents scientifiques de niveau recherche, publiés ou non, émanant des établissements d'enseignement et de recherche français ou étrangers, des laboratoires publics ou privés.

# Design and Control of a New Pulsating Power Decoupling Circuit for Grid- Connected Photovoltaic Systems

**Thèse de doctorat de l'université Paris-Saclay et de l'université  
Tarbiat Modares**

École doctorale n° 575, Electrical, Optical, Bio-Physics and Engineering (EOBE)  
Spécialité de doctorat : Génie Electrique  
Graduate School : Sciences de l'ingénierie et des systèmes. Référent : CentraleSupélec

Thèse préparée dans le Laboratoire de Génie Electrique et Electronique de Paris  
(Université Paris Saclay, CentraleSupélec, CNRS), sous la direction de **Demba DIALLO**,  
Professeur des Universités, la co-direction de **Ali YAZDIAN**, Professor

**Thèse soutenue à Paris-Saclay, le 10 March 2022, par**

**Elaheh HEYDARI**

## Composition du Jury

**Eric LABOURE**

Professeur des Universités,  
Université Paris-Saclay, GeePs

Président du jury

**Mohamed BENBOUZID**

Professeur des Universités,  
Université de Bretagne  
Occidentale, IRDL

Rapporteur & Examineur

**Mohammad Reza ZOLGHADRI**

Professor, Sharif University of  
Technology, Iran

Rapporteur & Examineur

**Reza BEIRANVAND**

Professor, Tarbiat Modares  
University

Examineur

**Demba DIALLO**

Professeur des Universités,  
Université Paris-Saclay, GeePs

Directeur de thèse

**Ali YAZDIAN VARJANI**

Professor, Tarbiat Modares  
University

Co-Directeur de thèse

*I would like to thank the following people who have helped me undertake this research:*

*I would like to express my deep appreciation to my supervisors Prof. Demba Diallo and Prof. Ali Yazdian for the continuous support of my Ph.D study and related research, for their patience, motivation, and immense knowledge. It was my honor to learn from them. Thank you for all your help and support, both professional and human, which I needed in the most difficult moments.*

*I would also like to extend my deep gratitude to Prof. Mohammad Pichan for his precious help in my thesis. I learned a lot from him throughout my research. Thank you for all your help and support.*

*I would also like to thank the members of the jury who accepted to evaluate this thesis. In particular, I would like to thank Prof. Eric Laboure who did me the honor of chairing the jury. A big thank you to Prof. Mohamed Benbouzid and Prof. Mohammad Reza Zolghadri who accepted to evaluate this work and for the time they devoted to it. I also thank Prof. Reza Beiranvand for his participation as an examiner.*

*I extend my thanks to all members of Geeps and Industrial Electronics & Applications laboratories, and EOBE doctoral school.*

*Finally, my deep and sincere gratitude to my family for their continuous love, help and support. I am grateful to my dear parents for their patience, immense love, trust and support. Thank you for always believing me and standing by me. Thank you, my sister and brother for continuous love and encouragement. Thank you for always being there for me.*

**Titre :** Conception et contrôle d'un nouveau circuit de découplage de puissance pulsée pour les systèmes photovoltaïque connecté au réseau

**Mots clés:** Système PV connecté au réseau, convertisseur à un étage, compensation de la puissance pulsée, compensateur de chute de tension, diagnostic de défaut.

**Résumé:** Aujourd'hui, les systèmes photovoltaïques connectés au réseau sont de plus en plus utilisés parmi les systèmes à énergies renouvelables. L'élément clé du système de conversion de puissance est le convertisseur statique connecté au réseau. Pour les applications de faible puissance, le convertisseur monophasé est le meilleur compromis. Les structures de conversion mono-étage permettent d'avoir un rendement plus élevé ainsi qu'un coût et une taille réduits. Cependant, dans des conditions de faible irradiation la tension PV chute, ce qui entraîne l'arrêt de l'onduleur et la perte totale de puissance injectée. Par conséquent, les systèmes à un étage de conversion souffrent d'une plage de fonctionnement réduite. Dans ce travail, nous proposons des solutions pour améliorer le rendement et la fiabilité des systèmes mono-étage connectés au réseau. Pour cela, dans la première partie, un contrôleur basé sur le mode glissant terminal rapide est combiné à un contrôle direct de la puissance. Il est associé à un algorithme de suivi du point de puissance maximale. Les simulations et les résultats expérimentaux sur un banc d'essai de 1kW montrent l'efficacité de la proposition en termes de performance dynamique, de faible distorsion harmonique totale et de robustesse aux variations d'irradiance. Les systèmes mono-étage sont également confrontés à une ondulation de puissance sur le bus continu à la fréquence double de celle du réseau. Ces ondulations de puissance sont néfastes à la durée de vie des panneaux solaires. Ainsi, la deuxième partie de ce travail propose de développer un dispositif qui simultanément réduit les ondulations de puissance et compense la chute de tension. Le dispositif est constitué de deux convertisseurs statiques : un flyback à faible puissance et un pont complet (H-bridge). Le compensateur hybride augmente la plage de fonctionnement de l'onduleur, empêchant son arrêt. Il contribue aussi à augmenter la fiabilité du

système. Un banc expérimental de 1kW a été dimensionné et réalisé. Il a permis d'évaluer le dispositif sur plusieurs points de fonctionnement. Les résultats en régime permanent montrent que le compensateur hybride peut simultanément réaliser une atténuation de 85% des ondulations de puissance et une compensation de 20% de la chute de tension. Le dispositif a également de bonnes performances en régime transitoire. Dans la troisième partie de ce travail, la surveillance des modules PV est abordée afin d'augmenter la fiabilité. La méthode proposée est basée sur la spectroscopie d'impédance. Elle ne nécessite pas d'équipement supplémentaire car elle utilise le circuit qui permet d'atténuer les ondulations de puissance. De plus elle ne nécessite pas d'interrompre la production d'électricité. Les résultats de simulation, à l'aide de MATLAB-Simulink®, montrent une réduction de plus de 80% de l'amplitude des ondulations de la tension aux bornes des modules PV. Les résultats montrent que la spectroscopie d'impédance permet d'estimer les paramètres de l'impédance du module PV avec une erreur relative inférieure à 5%. L'évolution de ces paramètres en cours de fonctionnement devrait permettre de surveiller l'état de santé du panneau.

**Title:** Design and control of a new pulsating power decoupling circuit for grid-connected photovoltaic systems

**Keywords:** Grid-connected PV system, Single-stage converter, Pulsating power decoupling, Voltage drop compensator, Fault diagnosis.

Today, grid-connected photovoltaic systems are becoming an increasingly important part of renewable energy. The power conversion system's heart is the grid-connected interface converter based on power electronics. The single-phase inverter is the best compromise for low power applications as an interface for power conversion. Single-stage systems offer higher efficiency and lower cost and size. However, the PV voltage drops under low irradiance conditions, leading to inverter shut down and the total injected power loss.

Consequently, single-stage systems suffer from a low operating range. This work addresses the critical issues of the single-stage single-phase grid-connected PV system, including reliability and efficiency. A fast terminal sliding mode combined with direct power control is proposed in the first part. It is associated with a maximum power point tracking algorithm with power output. Simulations and

experimental results on a 1kW test bench show the proposal's effectiveness in terms of dynamic performance, low total harmonic distortion and robustness to irradiance variations. Single-phase power systems also face pulsating power at twice the mains frequency on the DC bus. This pulsating power should not be transferred to the PV side as it reduces the efficiency of the solar panel. Thus, the second part of this work proposes a dual-function decoupling circuit: it mitigates pulsating power and compensates for the voltage drop. Thanks to the following additional power converters, these objectives are fulfilled: a low power flyback and an H-bridge. The hybrid compensator increases the inverter's operating range, prevents its shutdown, and increases the system reliability. A 1kW experimental bench has been designed to evaluate the proposal for several operating points. The steady-state results show that the hybrid compensator can simultaneously achieve 85% compensation of the pulsating power and 20% compensation of the voltage drop. The circuit also shows good transient responses. In the third part of this work, monitoring and fault diagnosis of PV modules are addressed to increase system reliability, efficiency, and safety. The proposed fault diagnosis method is based on online PV impedance spectroscopy without additional equipment. It does not require interrupting the power production and uses the pulsating power decoupling circuit as an impedance spectroscopy tool. The simulation results, using MATLAB-Simulink®, show more than 80% ripples amplitude of the PV modules terminal voltage. The results also show that impedance spectroscopy can estimate the PV module impedance parameters with a lower than 5% relative error. The evolution of these parameters during operation should make it possible to monitor the health of the panel.

## Table of Contents

<b>Chapter 1</b>	<b>General introduction.....</b>	<b>1</b>
1.1	Context of the study.....	2
1.2	Objectives .....	3
1.3	Contributions and outline .....	7
<b>Chapter 2</b>	<b>Literature review on single-phase grid-connected PV systems.....</b>	<b>9</b>
2.1	Control systems for single-phase PV systems .....	10
2.1.1	Maximum power point tracking algorithms .....	10
2.1.2	Grid-connected inverter control methods .....	13
2.2	Pulsating power decoupling circuits and PV voltage drop in single-stage systems .	19
2.2.1	Independent pulsating power decoupling circuits .....	20
2.2.2	Dependent pulsating power decoupling circuits.....	22
2.2.3	PV voltage drop.....	25
2.3	Fault diagnosis methods in PV systems.....	26
2.4	Problem statement .....	30
<b>Chapter 3</b>	<b>Proposed control system for single-phase PV systems.....</b>	<b>32</b>
3.1	Modified P&O algorithm.....	33
3.2	Power Control Strategy .....	34
3.2.1	System description.....	34
3.2.2	Fast terminal sliding mode control .....	36
3.2.2.1	General description.....	36
3.2.2.2	Stability analysis .....	41
3.3	Simulation results of the control system.....	42
3.3.1	Simulation results in steady state condition .....	43
3.3.2	Simulation results in transient conditions.....	44
3.4	Experimental results of the control system.....	46
3.4.1	Experimental results in steady state.....	47
3.4.2	Experimental results in transient operation .....	48
3.4.3	Comparison of experimental performance .....	50
3.5	Conclusion .....	51
<b>Chapter 4</b>	<b>Proposed dual- function pulsating power and voltage drop compensator for single-stage PV systems.....</b>	<b>53</b>
4.1	Dual-Function Power Decoupling Circuit .....	54
4.1.1	Operating Modes of the system.....	54

4.1.1.1	Pulsating power compensation mode: $V_{dc} > \frac{V_o}{m_a}$ .....	56
4.1.1.2	Hybrid compensator (pulsating power and voltage drop compensator) under mismatching conditions: $V_{dc} < \frac{V_o}{m_a}$ .....	56
4.2	Control System .....	57
4.3	The characteristics of the compensator.....	59
4.4	Experimental bench and results of the dual-function power decoupling circuit .....	62
4.4.1	Design of the test bench components .....	62
4.4.2	Power losses and cost calculation.....	65
4.4.3	Experimental results under rated irradiation .....	69
4.4.4	Experimental results under low irradiation .....	71
4.4.5	Experimental results in transient operation .....	72
4.4.6	Experimental results under condition of non-unity power factor.....	73
4.4.7	Comparison of decoupling circuits.....	74
4.5	Conclusion .....	75
<b>Chapter 5</b>	<b>Proposed dual- function Impedance spectroscopy tool and pulsating power compensator .....</b>	<b>77</b>
5.1	Impedance spectroscopy tool and pulsating power compensator .....	78
5.1.1	Equivalent electric circuit of a PV module.....	78
5.1.2	System operation description .....	80
5.1.2.1	Pulsating power decoupling .....	80
5.1.2.2	Impedance Spectroscopy .....	81
5.1.3	The characteristics of the compensator .....	85
5.1.4	Control system.....	86
5.2	Simulation and system design .....	88
5.2.1	Characteristics of the system under study .....	88
5.2.2	Theoretical impedance of the PV array .....	90
5.2.3	Tuning of the Impedance Spectroscopy .....	91
5.2.4	Simulation results .....	92
5.2.4.1	Simulation results under 1000 W/m <sup>2</sup> solar irradiance.....	92
5.2.4.2	Comparison between theoretical and the IS .....	96
5.2.4.3	Simulation results under 800 W/m <sup>2</sup> solar irradiance.....	97
5.3	Conclusion .....	98
<b>Chapter 6</b>	<b>Conclusion and perspectives .....</b>	<b>99</b>
References	.....	120

## Table of Figures

<b>Figure 1.1.</b> Circuit configuration of the grid-connected PV inverter. ....	3
<b>Figure 1.2.</b> Grid-connected PV inverter with pulsating power. ....	5
<b>Figure 1.3.</b> Conceptual P–V curve under typical operational conditions [4]. ....	6
<b>Figure 2.1.</b> General structure of the single-stage grid-connected PV system [12]. ....	10
<b>Figure 2.2.</b> I-V and P-V curves of a solar module. ....	11
<b>Figure 2.3.</b> P-V curve of a PV panel. ....	12
<b>Figure 2.4.</b> Flowchart of the conventional P&O algorithm [22]. ....	13
<b>Figure 2.5.</b> Block diagram of the SOGI [31]. ....	15
<b>Figure 2.6.</b> Block diagram of the deadbeat-direct power control [27]. ....	16
<b>Figure 2.7.</b> Block diagram of the deadbeat predictive power control [28]. ....	17
<b>Figure 2.8.</b> Block diagram of the power hysteresis control [29]. ....	17
<b>Figure 2.9.</b> Block diagram of the SMC- DPC [30]. ....	18
<b>Figure 2.10.</b> Schematics of the independent pulsating power decoupling circuits. ....	21
<b>Figure 2.11.</b> Schematic of the series pulsating power decoupling circuit [55]. ....	22
<b>Figure 2.12.</b> Schematics of the dependent pulsating power decoupling circuits. ....	24
<b>Figure 2.13.</b> The temperature distribution analysis using IRT [67]. ....	27
<b>Figure 2.15.</b> Schematic of the impedance spectroscopy measurement [77]. ....	28
<b>Figure 2.16.</b> The proposed online impedance measurement method in [85]. ....	29
<b>Figure 3.1.</b> Flowchart of the MPPT algorithm with power output. ....	34
<b>Figure 3.2.</b> The general structure of the system with FTSMC. ....	35
<b>Figure 3.3.</b> The equivalent circuit of the single-phase grid-tied inverter. ....	35
<b>Figure 3.4.</b> Block diagram of the proposed FTSMC. ....	40
<b>Figure 3.5.</b> The simulated system with FTSMC in Matlab-Simulink. ....	42
<b>Figure 3.6.</b> Simulation results of the FTSMC in steady state condition. ....	44
<b>Figure 3.7.</b> Grid current harmonic spectrum in the simulated system with FTSMC. ....	44
<b>Figure 3.8.</b> Simulation results of the FTSMC with active power step changes. ....	45
<b>Figure 3.9.</b> Simulation results of the FTSMC with reactive power step changes. ....	46
<b>Figure 3.10.</b> The experimental setup for FTSMC. ....	47
<b>Figure 3.11.</b> Experimental results of the FTSMC in steady state condition; time: (10ms/div), $P_o$ (1000 W/div), $Q_o$ (500 VAR/div), $v$ (500V/div), and $i_L$ (26A/div). ....	48
<b>Figure 3.12.</b> Experimental Grid current harmonic spectrum for FTSMC. ....	48
<b>Figure 3.13.</b> Experimental results of the FTSMC with active power step changes; time: (20ms/div), $P_o$ (1000 W/div), $Q_o$ (500 VAR/div), $v$ (500V/div), and $i_L$ (26A/div). ....	49

<b>Figure 3.14.</b> Experimental results of the FTSMC with reactive power step changes; time: (20ms/div), $P_o$ (1000 W/div), $Q_o$ (500 VAR/div), $v$ (500V/div), and $i_L$ (26A/div). .....	50
<b>Figure 3.15.</b> Experimental results of FTSMC with mismatches in filter inductor; time: (20ms/div), $P_o$ (1000 W/div), $Q_o$ (500 VAR/div), $v$ (500V/div), and $i_L$ (26A/div). .....	50
<b>Figure 4.1.</b> General structure of the single-stage grid-connected PV inverter with hybrid compensator. ....	54
<b>Figure 4.2.</b> Operating modes of the proposed hybrid compensator. ....	55
<b>Figure 4.3.</b> Block diagram of the controller of hybrid compensator. ....	58
<b>Figure 4.4.</b> Power ratio. ....	60
<b>Figure 4.5.</b> Evolution of capacitors $C_{dc}$ and $C_{comp}$ . ....	63
<b>Figure 4.6.</b> The experimental setup for hybrid compensator. ....	65
<b>Figure 4.7.</b> Power loss breakdown analysis. ....	69
<b>Figure 4.8.</b> Experimental results of the proposed compensator under rated irradiation; time: (5ms/div), $v_{dc}$ (100 V/div), $V_{pv}$ (100 V/div), $v_g$ (250V/div), .....	70
<b>Figure 4.9.</b> Experimental results of the proposed compensator under rated irradiation; time: (10ms/div), $i_L$ (25 A/div), $I_{pv}$ (5 A/div), and $v_c$ (20 V/div). ....	70
<b>Figure 4.10.</b> Experimental results of the proposed compensator under conditions of low irradiation; time: (5ms/div), $v_{dc}$ (100 V/div), $V_{pv}$ (100 V/div), $v_g$ (250V/div), and $v_{comp}$ (100V/div). ...	71
<b>Figure 4.11.</b> Experimental results of the proposed compensator under conditions of low irradiation; time: (10 ms/div), $i_L$ (25 A/div), $I_{pv}$ (5 A/div), and $v_c$ (20 V/div). ....	72
<b>Figure 4.12.</b> Transient responses of the proposed compensator; time: (20ms/div), $v_{dc}$ (80 V/div), $V_{pv}$ (80V/div), and $v_{comp}$ (80V/div). ....	73
<b>Figure 4.13.</b> Experimental results of the proposed compensator with 0.9 leading power factor; time: (10ms/div), $v_{dc}$ (100 V/div), $V_{pv}$ (100 V/div), $v_g$ (250V/div), and $i_L$ (25V/div). ....	73
<b>Figure 5.2.</b> The static (DC) equivalent circuit of a PV module [95]. ....	78
<b>Figure 5.3.</b> The dynamic equivalent circuit of a PV module. ....	79
<b>Figure 5.4.</b> Circuit configuration of the PV system with proposed circuit as pulsating power compensator and IS circuit. ....	80
<b>Figure 5.5.</b> The PV panel equivalent circuit with impedance measurement. ....	82
<b>Figure 5.6.</b> The simplified PV panels equivalent circuit. ....	82
<b>Figure 5.7.</b> Nyquist diagram of the PV panel. ....	83
<b>Figure 5.8.</b> The proposed controller for pulsating power decoupling and IS. ....	87
<b>Figure 5.9.</b> The grid current controller for pulsating power decoupling and IS. ....	87

<b>Figure 5.10.</b> Simulated system of the pulsating power decoupling and IS circuit with Matlab-Simulink. .....	90
<b>Figure 5.11.</b> Bode diagram of the PV impedance. ....	91
<b>Figure 5.12.</b> The voltage excitation in the case of $\gamma = 0.03$ . ....	92
<b>Figure 5.13.</b> Simulated voltages for pulsating power decoupling and IS circuit: PV array ( $V_{pv}$ ), DC-link ( $v_{dc}$ ), compensator ( $v_{comp}$ ), grid ( $v_g$ ). ....	93
<b>Figure 5.14.</b> Simulation results for pulsating power decoupling and IS circuit: PV power ( $P_{pv}$ ), PV current ( $I_{pv}$ ), and grid current ( $i_L$ ). ....	94
<b>Figure 5.15.</b> Grid current harmonic spectrum for pulsating power decoupling and impedance measurement circuit. ....	94
<b>Figure 5.16.</b> PV array ( $V_{pv}$ ), and compensator ( $v_{comp}$ ) voltages for pulsating power decoupling and IS circuit. ....	95
<b>Figure 5.17.</b> PV current for pulsating power decoupling and IS circuit. ....	95
<b>Figure 5.18.</b> The Nyquist diagram of theoretical and IS impedances. ....	96
<b>Figure 5.19.</b> Nyquist plot of PV array impedance using curve fitting. ....	97
<b>Figure 5.20.</b> Bode diagrams of the theoretical and IS impedances. ....	97
<b>Figure 5.21.</b> The Nyquist diagram of the theoretical and IS under 800W/m2. ....	98

## Table of Tables

<b>Table 2.1.</b> Comparison of several power decoupling circuits. ....	24
<b>Table 3.1.</b> The parameters of system with FTSMC. ....	42
<b>Table 3.2.</b> Specifications of the PV module (APOS Energy AP210) .....	43
<b>Table 3.3.</b> The proposed FTSMC parameters. ....	43
<b>Table 3.4.</b> Comparison of experimental performance of the proposed FTSMC .....	51
<b>Table 4.1.</b> Parameters of the main inverter in the PV system .....	64
<b>Table 4.2.</b> Parameters of the hybrid compensator. ....	64
<b>Table 4.3.</b> Power losses and cost calculation of the system proposed in [55]. ....	67
<b>Table 4.4.</b> Power losses, efficiency and costs for the proposed circuit. ....	68
<b>Table 4.5.</b> Comparison of decoupling circuits with proposed hybrid compensator. ....	75
<b>Table 5.1.</b> Main inverter parameters in the system with IS. ....	88
<b>Table 5.2.</b> The IS circuit parameters. ....	88
<b>Table 5.3.</b> Specifications of the PV module at 1000 W/m <sup>2</sup> , 25 °C . ....	89

## **Chapter 1 General introduction**

## 1.1 Context of the study

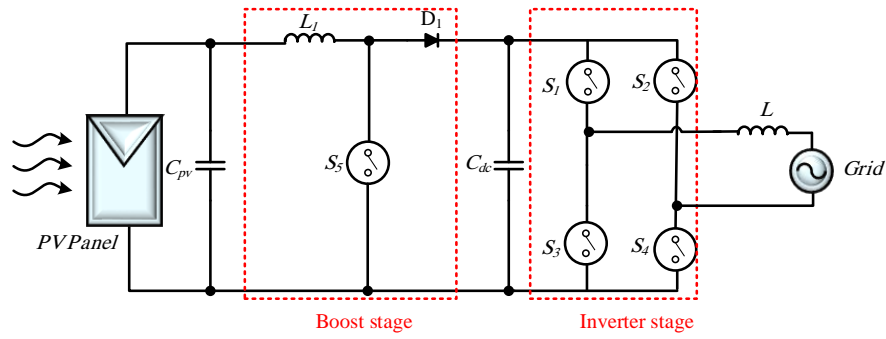
Because of environmental issues, renewables are expected to be the fastest-growing energy sources for electricity production. Their contribution is expected in 2040 to be doubled compared to 2012 [1]. Among renewable energy sources, photovoltaic (PV) plants have experienced the fastest growth thanks to the progress in semiconductor materials, packaging, and cost reduction [1]. Besides, the PV module has no moving parts, making it a long lifetime, robust and low maintenance device. By the end of this century, it is expected to have the most significant generation among renewable energy sources, up to 60% of the total energy [2].

The produced power from the PV panels has shifted from stand-alone to grid-connected as the technologies of power electronic converters and control methods are becoming more mature, so that the stand-alone market can hardly be compared with the grid-connected market [2]. Increasing reliability, efficiency and reducing system costs are the challenging targets for each electrical system, including grid-connected PV systems.

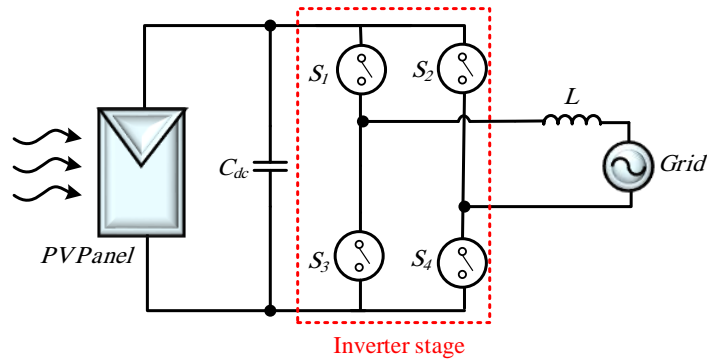
An important issue to increase the PV system efficiency is to capture the maximum power of PV panels and transfer it to the grid. Therefore, the maximum power point tracking (MPPT) algorithm and the grid side controller are crucial. For low power applications, a single-phase inverter is the best compromise for power converter interfaces. However, single-phase power systems face power oscillations (pulsating power) at twice the grid frequency on the DC bus. This disturbance reduces the efficiency and the PV panel lifetime. It also degrades the performance of the maximum power point tracking algorithm [3].

As a result, on the one hand, an efficient control system and pulsating power elimination must be addressed for single-phase grid-connected PV systems. On the other hand, active maintenance based on continuous monitoring of PV panels is essential to ensure the PV system reliability and safety.

There are two main configurations for single-phase grid-connected PV systems: single and two-stage systems shown in Figure 1.1.



a) Two-stage



b) Single-stage

**Figure 1.1.** Circuit configuration of the grid-connected PV inverter.

The PV power plant is connected to the grid through a DC/DC converter and an inverter in the two-stage configuration. Thus, the voltage required to feed the grid is obtained by a boost converter sized at the rated power. Removing this stage reduces the size and costs by switching to a single-stage system. However, the operating voltage range is limited at low irradiation, which leads to power losses [4]. As a result, structures that can overcome the limited operating voltage range gain interest in single-stage configurations.

## 1.2 Objectives

In this study, a comprehensive study is carried out on the main challenges in a single-stage single-phase grid-connected PV system.

Three topics have been developed in this work:

- control of the system,
- mitigation of pulsating power and voltage drop under low irradiance conditions,
- and the monitoring of PV panels.

- *Control system*

In a single-stage PV system, MPPT algorithm and grid current controller drive the only power converter, which is the inverter. Fast transient response is essential for active or reactive power injection into the grid. Besides, a good power quality with a low total harmonic distortion (THD) of the grid current is required in grid-connected system. Thus, the efficient coordination between grid and PV side controllers results in removing the internal loops, which increases the dynamic response.

In this work, we'll address these requirements for the control of a single-stage grid-connected PV inverter.

- *Pulsating Power and PV voltage drop*

In a single-phase grid-connected system, grid voltage and current can be expressed as:

$$v_g(t) = V_o \cos(\omega t) \quad (1.1)$$

$$i_L(t) = I_o \cos(\omega t - \phi_o)$$

With no loss of generality, a unity factor is assumed. Therefore, the instantaneous power is as follows:

$$p_{ac}(t) = P_o + P_o \cos(2\omega t) \quad (1.2)$$

where  $P_o = \frac{V_o I_o}{2}$ .

$P_o \cos(2\omega t)$  is the pulsating power, which is absorbed from the AC side. This pulsating power will be transferred to the DC side as shown in Figure1.2. Therefore, the DC-Link voltage becomes:

$$v_{dc}(t) = V_{dc} + v_{ripple}(t) \quad (1.3)$$

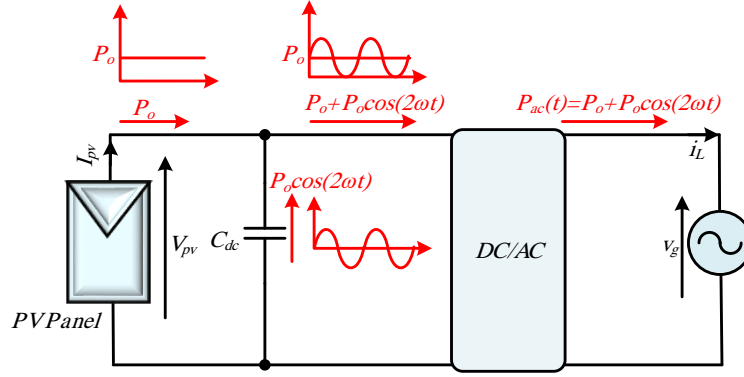


**Figure 1.2.** Grid-connected PV inverter with pulsating power.

$v_{ripple}(t)$  is the voltage ripple at twice the grid frequency:

$$v_{ripple}(t) = |\Delta v_{dc}| \cos(2\omega t) \quad (1.4)$$

It should be mentioned that for photovoltaic applications, the voltage ripple should not be transferred to the PV side as it reduces the efficiency of the solar panel.

The solutions to address this issue are mainly divided into two categories: passive and active decoupling methods. The passive decoupling methods consist of increasing the DC-Link inductance or capacitance [3]. Recently, more attention has been paid to capacitive energy storage for reducing cost and volume compared to inductive energy storage. Besides, the inductances can increase the power losses because of high equivalent series resistance. Therefore, an electrolytic capacitor calculated from (1.5) is connected to the DC bus to mitigate this disturbance.

$$C_{dc} = \frac{P_o}{2\omega V_{dc} |\Delta v_{dc}|} \quad (1.5)$$

However, these capacitors suffer from low reliability. Typically, the lifetime of electrolytic capacitors at temperatures of 40-105°C is about 1000-7000 hours. This is short compared to the lifetime of PV modules that is more than 20 years [5]. Furthermore, for an increase of 10°C, the lifetime of electrolytic capacitors will be halved, according to the Arrhenius equation [5,6].

One solution is to replace electrolytic capacitors with film capacitors, which have a longer lifetime. However, film capacitors with the same capacity are larger and more expensive than electrolytic capacitors.

Active power decoupling circuits consist of power switches and an energy storage device. As the energy storage device only compensates for pulsating power, film capacitors can be used. Therefore, active decoupling circuits have been proposed with long-life, low-volume film capacitors [5].

On the other hand, single-stage PV systems suffer from reduced operating range due to irradiation and temperature. In [4], the PV arrays are connected to a 220V grid. So, the operating voltage of the PV arrays is limited to 360-400V. Conceptual P–V curve for illustrating a limited operating voltage range under typical operational conditions is shown in Figure 1.3 [4].

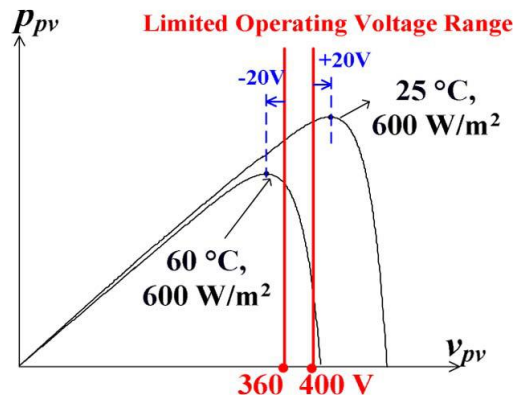


**Figure 1.3.** Conceptual P–V curve under typical operational conditions [4].

The operating voltage  $V_{mpp}$  lies out of the limited range, reducing the power conversion efficiency of 4% [4]. Thus, the absence of a boost in these systems may decrease conversion efficiency under low irradiation conditions. In single-stage configurations, voltage drop compensation and limitation of inverter operating range are not yet addressed.

As a result, the two aforementioned critical issues for single-stage PV inverters are addressed in this study.

- *PV panels monitoring and fault diagnosis*

The operating maintenance and protection have received great importance with the exponential growth of PV systems. PV modules suffer from various failures due to endogenous (ageing, short circuit, open circuit, ...), and exogenous (transport, shading, soiling, ...) reasons. These faults may result in the reduction of power conversion efficiency, module damage or even fire. Therefore, monitoring and fault diagnosis of PV modules is crucial to increase system reliability, efficiency, and safety [7,8]. Different methods have been proposed for the fault detection and diagnosis of PV modules [9,10]. The methods can be broadly classified in two families: visual inspection (human and camera-assisted, and automatic analysis).

Human visual inspection is only suitable for small PV plants and may suffer from misinterpretation. Camera-assisted inspection is based on the use of images captured by drones or UAV. Besides the high cost, the images should be corrected with heavy processing techniques to eliminate/compensate nuisances due to environmental conditions. The automatic analysis consists of processing input raw data to extract fault features. The input data are usually PV voltage and current, irradiance and temperature. One of the main problems is to monitor the PV modules without interrupting energy production, and to use only already available measurements. Our study has developed a monitoring method that takes benefit of our power conversion structure and its control. It is expected to operate online without additional equipment and interruption of energy production.

### **1.3 Contributions and outline**

In this study, the aforementioned critical issues in single-stage single-phase grid-connected PV systems are studied, and relevant solutions are proposed.

The principal contributions of this work are:

- A new control system including MPPT algorithm, and grid-side controller,
- A dual-function pulsating power decoupling circuit, which compensates for the pulsating power, and the voltage drop due to low irradiation,
- A dual-function converter, which compensates for the pulsating power and realizes an online monitoring method for the PV array.

The present document is structured in 6 chapters.

In chapter 2, the literature review is presented. Different control methods, pulsating power decoupling and fault diagnosis methods of single-phase PV systems are studied and analyzed. These topics are studied based on the crucial issues of single-stage PV systems. The main challenges are explained in the problem statement.

In chapter 3, the proposed control system is presented, and its effectiveness is proven using simulation and experimental results. The proposed control system is also compared to different previous works.

In chapter 4, a dual-function pulsating power decoupling and its control system is proposed. The proposed system compensates for the pulsating power and the voltage drop due to low irradiance conditions with an additional low power circuit. The validation is carried out through experimental results. A comparison of performance is made with other circuits.

Chapter 5 proposes a new tool for pulsating power decoupling and impedance spectroscopy (IS) as a monitoring method. Intensive simulations are done to show the effectiveness of the proposed circuit.

Chapter 6 concludes the manuscript, and proposes several perspectives.

## **Chapter 2 Literature review on single-phase grid-connected PV systems**

## 2.1 Control systems for single-phase PV systems

The control system in the grid-connected PV system is done through two control loops [11]. The inner loop generates the power switching signals to modulate the inverter output current in accordance with grid requirements. The outer loop uses maximum power point tracking algorithms to capture the maximum power from the solar panels [11]. The control system response on both grid and PV sides plays an important role since it directly affects the extraction of maximum power from solar energy, the harmonic distortion of injected grid current, and transient response. In addition, coordination of grid-side and PV-side controllers has attracted more attention to mitigate the grid and external distortions. This is even more crucial for single-stage PV systems that have only one power converter. The general structure of control system for the single-stage grid-connected PV system is shown in Figure 2.1 [12].

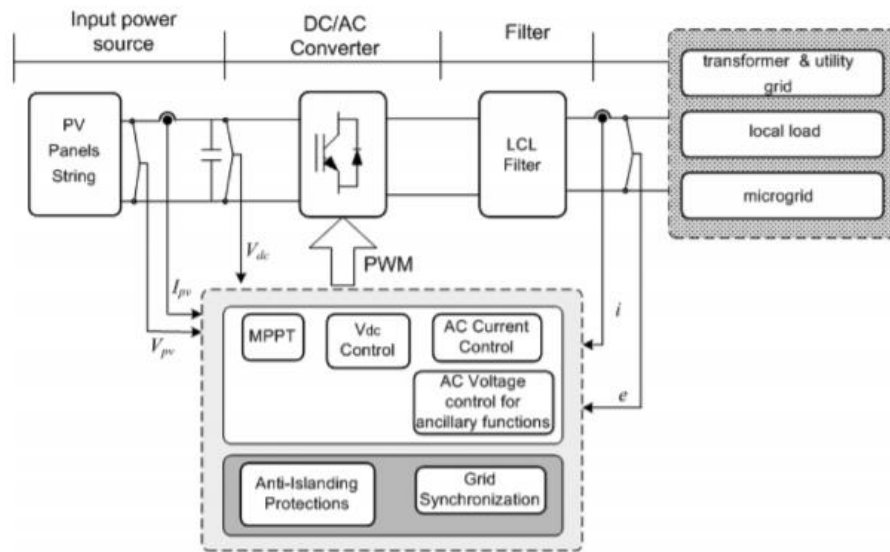


**Figure 2.1.** General structure of the single-stage grid-connected PV system [12].

### 2.1.1 Maximum power point tracking algorithms

The typical I-V and P-V curves of a solar module are displayed in Figure 2.2. As shown, for the solar module, there is a maximum power operating point for each irradiance and temperature, which should be tracked in order to ensure the efficient operation of the solar

modules. This issue is addressed by MPPT to automatically determine the PV voltage or current to produce the maximum power under a given irradiance and temperature.

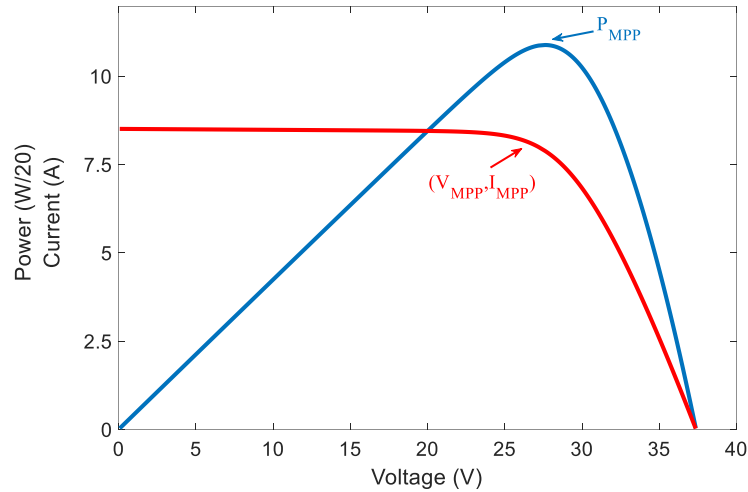


**Figure 2.2.** I-V and P-V curves of a solar module.

An important issue in the grid-connected PV system is to capture the maximum power from the solar irradiance and convert it efficiently into electrical power transferred to the grid. Many methods have been proposed to control the power interfaces on both PV and grid to deal with the power conversion and transfer.

To capture the maximum power with PV panels, different maximum power point tracking algorithms are proposed, which can be classified in two main categories: offline or indirect methods, and online or direct methods [13,14]. Indirect methods are based on estimation of maximum power point based on database of PV panels or mathematical calculations. Curve-fitting [15], fractional-short circuit current [16], fractional-open circuit voltage [17] and look-up table [18] are indirect MPPT techniques. In these methods, MPP is estimated approximately. However, in the direct methods, the PV voltage and current are used directly and MPP can be obtained without the knowledge of the environmental conditions such as irradiance or temperature. Feedback voltage or current [19], feedback of power variation with voltage [20], forced oscillation [21], Perturb and Observe (P&O) [22-24], and Incremental conductance [25] are the most common techniques in this category.

Among these methods, the P&O algorithm is the most popular one because of its high accuracy in MPP tracking, simplicity and easy implementation [13,14]. In this method, at first the PV current and voltage at the sample time  $k$  ( $I_{pv}(k), V_{pv}(k)$ ) are measured and the corresponding power ( $P_{pv}(k)$ ) is calculated. Then, a small voltage perturbation ( $\Delta V$ ) [22], current perturbation ( $\Delta I$ ) [23] or duty cycle perturbation ( $\Delta D$ ) (for systems with DC/DC converter) [24] is applied in one direction and the corresponding power is calculated. As shown in a typical P-V curve in Figure 2.3, on the left side of the MPP,  $\frac{dP_{pv}}{dV_{pv}} > 0$ , and  $V_{ref}(k)$  should be increased and selected as  $V_{ref}(k) = V_{ref}(k-1) + \Delta V$ . On the other hand, on the right side of the MPP,  $\frac{dP_{pv}}{dV_{pv}} < 0$  and  $V_{ref}(k)$  should be decreased and selected as  $V_{ref}(k) = V_{ref}(k-1) - \Delta V$ . Finally, at the MPP,  $\frac{dP_{pv}}{dV_{pv}} = 0$  and the algorithm is stopped. The flowchart of P&O algorithm with voltage perturbation is shown in Figure 2.4 [22].

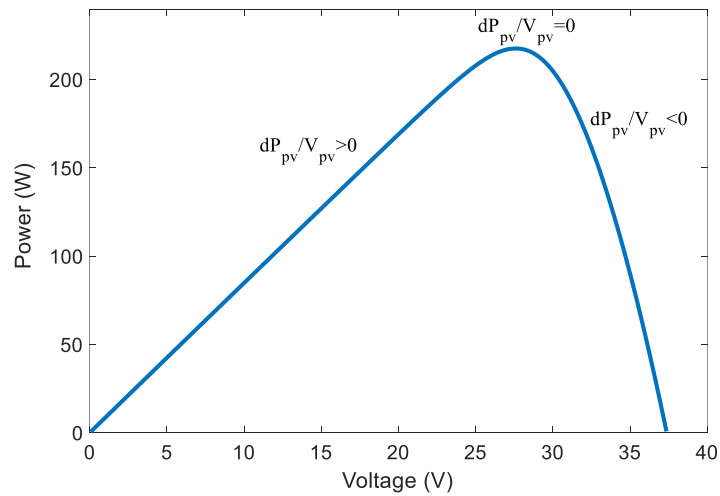


**Figure 2.3.** P-V curve of a PV panel.

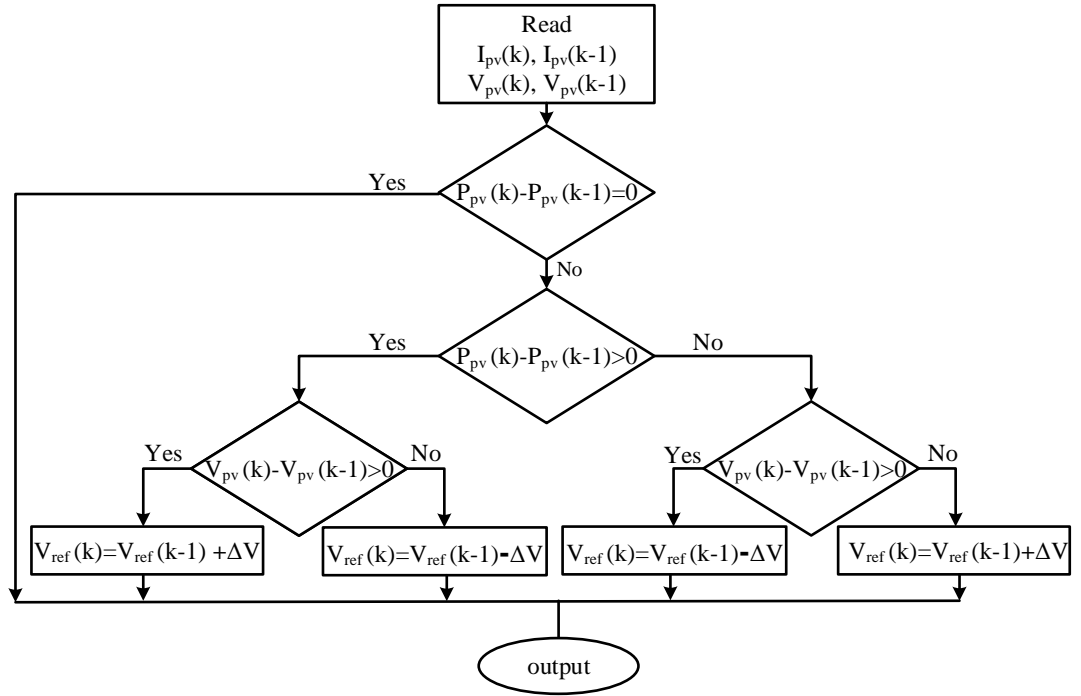


**Figure 2.4.** Flowchart of the conventional P&O algorithm [22].

### 2.1.2 Grid-connected inverter control methods

Among many control methods that have been explored for control of grid-tied converters with different characteristics, direct power control (DPC) is particularly of interest [26-30]. The conventional DPC acts based on selecting the best switching state of the power switches through a lookup table with hysteresis comparisons to achieve unity power factor and maintain constant dc-Link voltage [26]. Its popularity is due to its simplicity and ease of digital implementation. However, it needs a high sampling frequency and a variable switching frequency, which makes the design of the filter and the cooling system hard and complex. To overcome these issues, different modified DPC schemes with a constant switching frequency, such as deadbeat-direct power control [27], model predictive power control [28], power hysteresis control [29], and sliding mode control (SMC)-direct power control [30] have been proposed.

The reference frames theory used for the control of AC drives is also used to design the control of power electronics converters especially grid-connected ones. There are two main

reference frames used in the control of grid-connected power converters; 1- Rotating ( $dq$ ) reference frame, 2- Stationary ( $\alpha\beta$ ) reference frame.

In the  $dq$  reference frame, in steady-state, the AC variables are transformed into DC ones, which can be driven with usual PI controllers. Other benefits related to the  $dq$  reference frame is in accordance with the powers equations in this frame defined as follows:

$$P_o = v_{gd} i_{Ld} + v_{gq} i_{Lq} \quad (2.1)$$

$$Q_o = v_{gq} i_{Ld} - v_{gd} i_{Lq}$$

Where  $v_{gd}, v_{gq}, i_{Ld}, i_{Lq}$  are the grid voltage and current components in the  $dq$  reference frame. Usually, a synchronization unit is used to lock the reference frame to the grid voltages. Hence at the constant grid voltage frequency,  $v_{gd} \neq 0$ ,  $v_{gq} = 0$ . Accordingly, the power equations can be simplified as follows:

$$P_o = v_{gd} i_{Ld} \quad (2.2)$$

$$Q_o = -v_{gd} i_{Lq}$$

Based on (2.1) and (2.2), active and reactive powers can be controlled independently in the  $dq$  reference frame [27]. Also, the number of variables is decreased from three to two under the assumption of balanced three-phase three-wire systems. The main challenge is to maintain the coordination between the grid voltages, and the rotating reference frame.

To avoid the issues that may arise due to mis-coordination, the stationary  $\alpha\beta$  reference frame is an option. The number of variables is also reduced from three to two under the assumption of a balanced three-phase three-wire systems. In the single-phase system, virtual two-phase converter model can be used to obtain grid voltage and current components in the  $\alpha\beta$  reference frame. Thus, a phase locked loop (PLL) structure based on the second-order-generalised-integrator (SOGI) is adopted [31]. This method provides simple digital implementation, low computational complexity and good performance under distorted grid voltage. The block diagram of the SOGI is shown in Figure 2.5 [31].

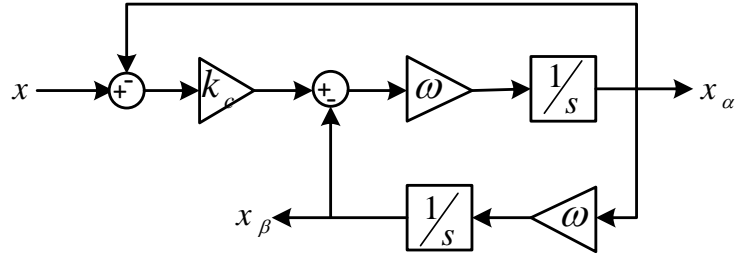


**Figure 2.5.** Block diagram of the SOGI [31].

The corresponding transfer functions are expressed as follows:

$$G_d(s) = \frac{x_\alpha}{x} = \frac{k_c \omega s}{s^2 + k_c \omega s + \omega^2} \quad (2.3)$$

$$G_q(s) = \frac{x_\beta}{x} = \frac{k_c \omega^2}{s^2 + k_c \omega s + \omega^2}$$

Where  $k_c$  allows tuning the closed-loop system bandwidth and  $\omega$  is the fundamental angular frequency. Applying (2.3) to the grid current and voltage, the orthogonal two-phase system can be obtained. It is preferable to implement the control system in the  $\alpha\beta$  reference frame to avoid the issue related to orthogonal signal generation in single-phase grid-connected converters.

The scheme of the deadbeat-direct power control is shown in Figure 2.6 [27]. The converter voltage reference is determined at each sampling period so that the power errors are driven to zero at the next sampling period. To address this, the active and reactive powers at the next sampling period are predicted using the virtual two-phase converter model. Then they are used as reference values for the current sampling period.

The advantage of this control method is its high dynamics. However, it suffers from low robustness against parameter mismatches, model uncertainties, and the need for a high sampling frequency.

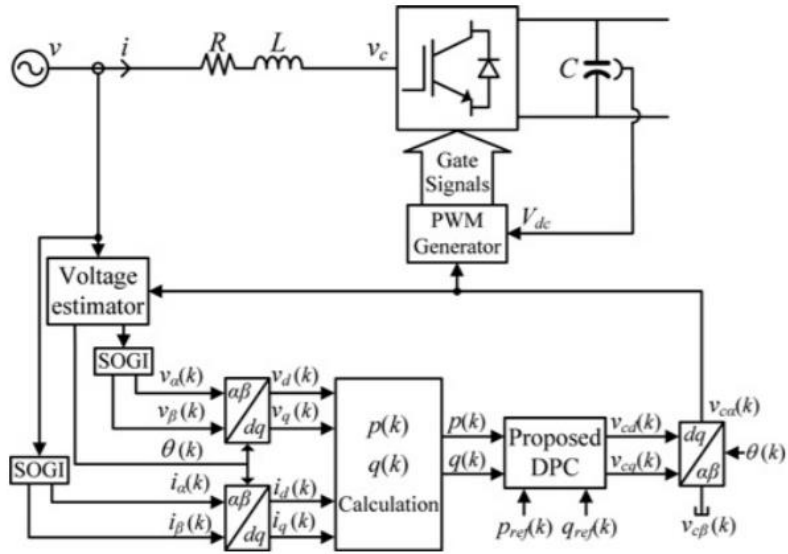


**Figure 2.6.** Block diagram of the deadbeat-direct power control [27].

The predictive power control based on deadbeat controller is shown in Figure 2.7 [28]. In predictive control, the output signals are selected to minimize a cost function over a time horizon. The method has good dynamic performance. However, it needs an accurate model of the system that makes it highly sensitive to parameter mismatches and model uncertainties. On the other hand, the proposed delay compensation is an inaccurate method.

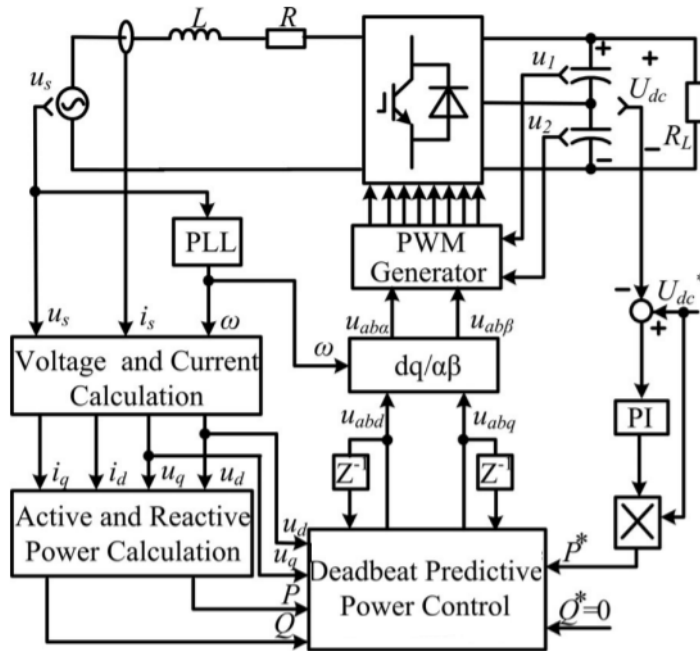


**Figure 2.7.** Block diagram of the deadbeat predictive power control [28].

In the power hysteresis control scheme shown in Figure 2.8 [29], the main idea is to combine the conventional table-based DPC and PI-based DPC. It is based on a simple DPC scheme with hysteresis comparators and a pulse width modulator (PWM) to generate the reference voltage [29]. The dynamic performance is improved but the method suffers from control complexity, high computational burden, and high sampling frequency.

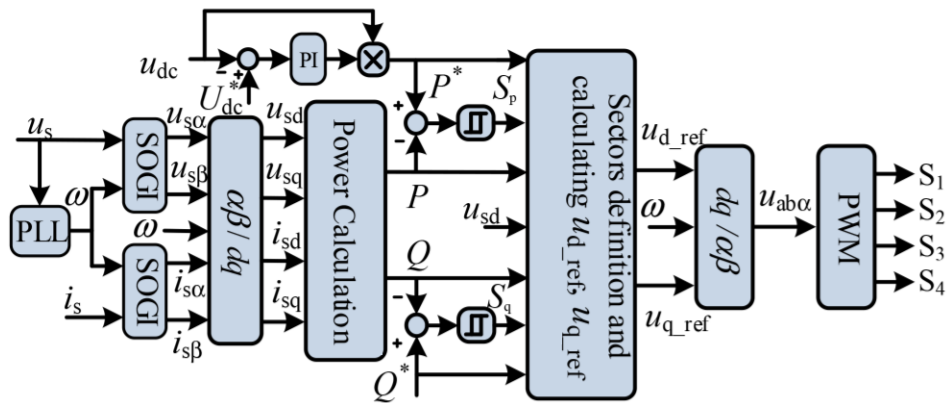


**Figure 2.8.** Block diagram of the power hysteresis control [29].

Another technique used to drive power converters is sliding mode control [32]. The design of a SMC requires selecting a sliding surface, setting the control law, and finally assessing the stability. The states of the system are at first attracted towards the sliding surface before sliding on it. Consequently, the sliding surface and its derivative that is a linear function of the error are equal to zero. The technique is easy to implement, and robust against parameter variations and model mismatches [33,34]. It exhibits also good dynamic performance due to its inherent switching nature. A SMC-DPC for a three-phase grid-connected inverter is shown in Figure 2.9 [30]. The control objectives are the slide along the predefined active and reactive power trajectories. So, the sliding surfaces are considered as:

$$S_p = e_p(t) + K_p \int e_p(\tau) d\tau \quad (2.4)$$

$$S_Q = e_Q(t) + K_Q \int e_Q(\tau) d\tau$$

Where  $e_p(t)$  and  $e_Q(t)$  are the respective errors between the references and the actual values of instantaneous active and reactive powers.

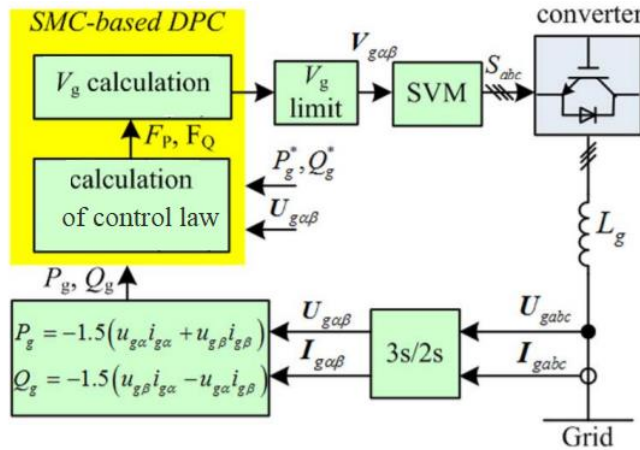


**Figure 2.9.** Block diagram of the SMC- DPC [30].

However, the conventional SMC suffers from infinite convergence time and especially for grid connected converters, poor transient response during grid voltage distortion [35]. This issue can be addressed with higher coefficients on the sliding surface but will not prevent from the steady state error. To improve the conventional SMC, terminal sliding mode control (TSMC) has been proposed. It is based on specific computations of the sliding surface [35].

In TSMC, the convergence time not only is finite but also, it can be properly tuned to be as low as possible. Thus, by using TSMC the system's dynamic is improved. However, when the states of the system are not near the equilibrium point, the convergence time increases. To solve this problem, fast terminal sliding mode control (FTSMC) has been proposed. For this control, the sliding surface consists of linear and non-linear terms, resulting in fast dynamic response whether the states are close or far from an equilibrium operating point [36-38].

To conclude, control methods that can guarantee simultaneously: high performance, fast dynamics, robustness against model parameter mismatches, high grid current quality, and ease of implementation are of high interest.

## **2.2 Pulsating power decoupling circuits and PV voltage drop in single-stage systems**

A major concern for single-phase grid-connected systems is the pulsating power on the DC bus at twice the frequency of the mains. The common solution to absorb these power oscillations is to connect large electrolytic capacitors to the DC bus. However, these capacitors suffer from low reliability [39]. One solution is to replace electrolytic capacitors with film capacitors with longer lifetime. However, film capacitors with the same capacity are larger and more expensive than electrolytic capacitors. Therefore, active pulsating power decoupling topologies, which consist of power switches and energy storage device have been proposed [3]. The idea of these methods is to divert the pulsating power to another energy storage device. As a result, active power decoupling circuits are proposed in association with long-lifetime and low-volume film capacitors [3].

Generally, the power decoupling topologies include the decoupling cell and the main converter. Some of the decoupling cells operate partially or completely with the main converter and some of them operate independently. Therefore, they can be broadly classified for single-phase systems into two main categories: independent decoupling circuits and dependent or switch-multiplexing ones [3].

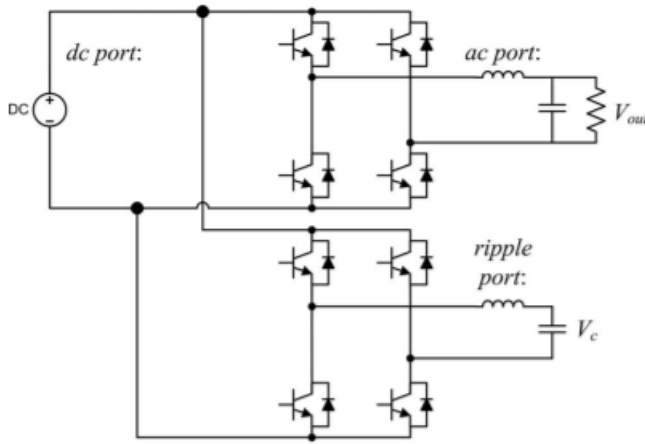
### 2.2.1 Independent pulsating power decoupling circuits

In independent pulsating power decoupling circuits, the decoupling cell and the main converter operate independently. The decoupling cell is usually connected in parallel or in series to the DC-Link. The main converter is responsible for DC-Link voltage/current regulation while decoupling cell deals with pulsating power.

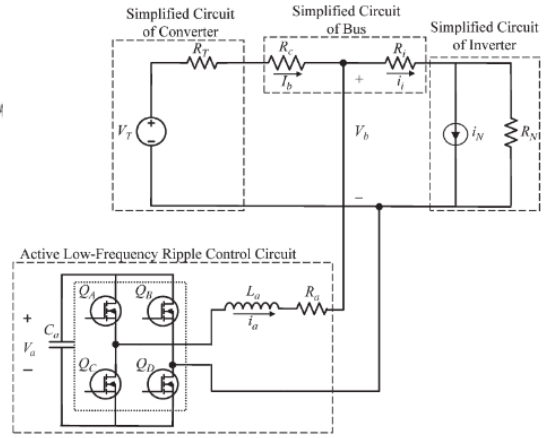
In [40,41] the decoupling circuit is based on an H-bridge. In [40] (Figure 2.10a), the voltage across the decoupling capacitor must be lower than the DC-link voltage. Thus, the decoupling cell has been reduced to a buck converter (Figure 2.10c) [42] suitable for high DC voltage applications. In this topology, the injected current is discontinuous, and the pulsating power is mostly stored in buck converter capacitor. This solution has been investigated for different operating modes, control methods, and applications [43-45].

In [41] (Figure 2.10b) the voltage across the decoupling capacitor must be higher than the DC-link voltage. So, the decoupling cell became a boost converter (Figure. 2.10d) [46]. Unlike the buck converter, it injects a continuous current, and is more suitable for low DC voltage applications.

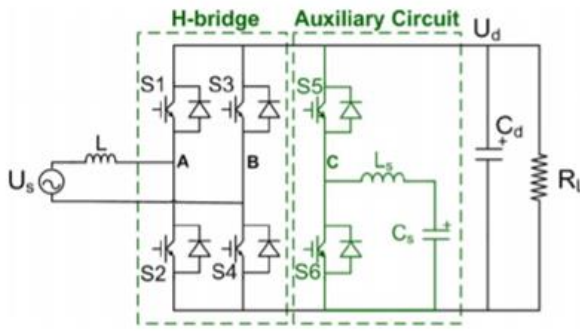
Several improved control methods and different applications have been proposed for this topology [47-50]. The problem of operating voltage range of decoupling capacitor has been solved using the decoupling cells based on buck-boost converter in Figure 2.10e [51,52] with flexible voltage range. In the capacitor-split-based decoupling cell (Half-bridge converter), the decoupling capacitors are also used as output filter [53,54]. This topology is shown in Figure 2.10f.



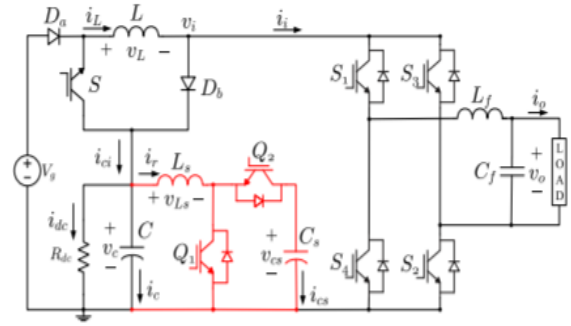
a. H-bridge converter [40]



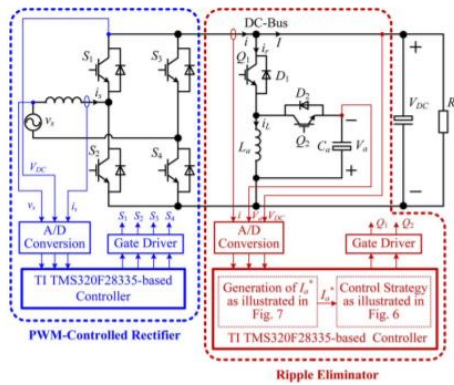
b. H-bridge converter [41]



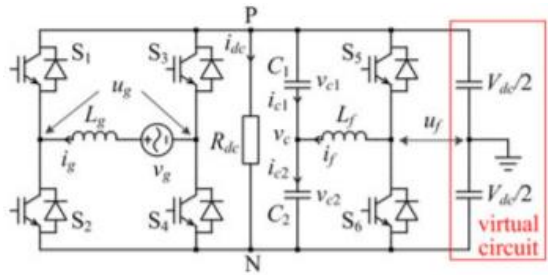
c. Buck converter [42]



d. Boost converter [46]



e. Buck- Boost converter [51]



f. Half-bridge converter [54]

**Figure 2.10.** Schematics of the independent pulsating power decoupling circuits.

These independent decoupling circuits do not affect the performance, and the operating points of the main converter. However, their common issue is that the voltage stress on the decoupling circuit is equal to or higher than the DC-Link voltage. Therefore, the cost is

increased, and the efficiency is reduced. This challenge can be addressed with series-decoupling cell that adds a compensation voltage to the DC-Link [55,56]. The series-decoupling cell shown in Figure 2.11 [55,56] is based on the H-bridge converter for two-stage grid-connected PV systems. Although the number of switches has increased, the compensator power rating is much less than the main converter [55].

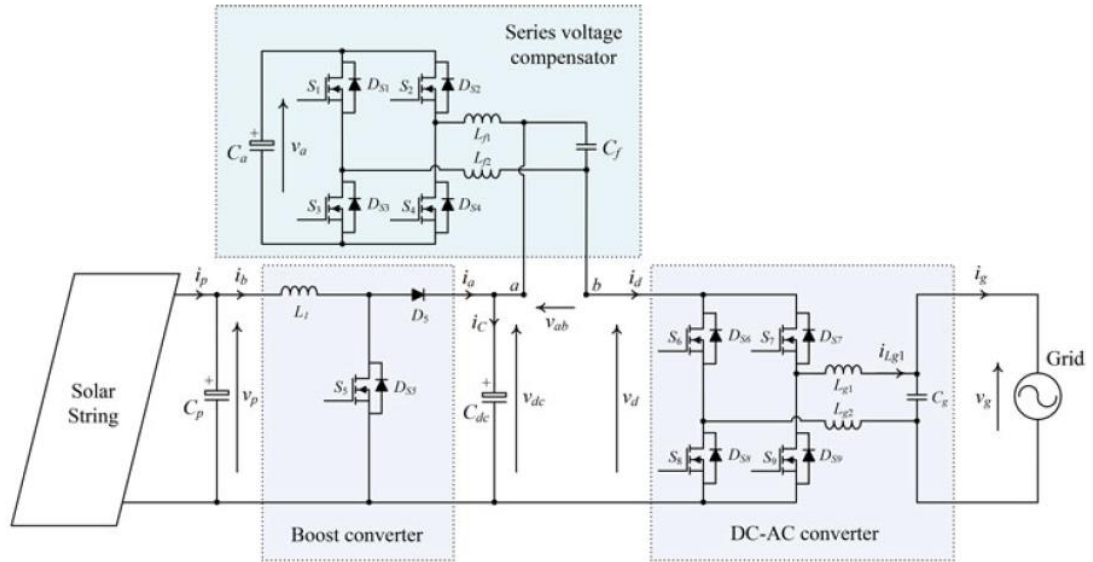


**Figure 2.11.** Schematic of the series pulsating power decoupling circuit [55].

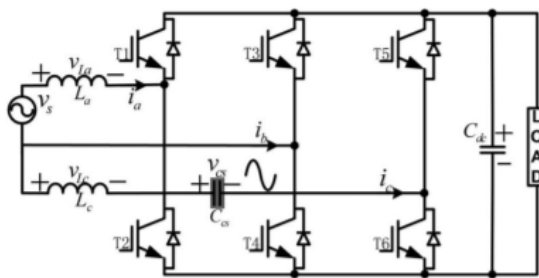
### 2.2.2 Dependent pulsating power decoupling circuits

In dependent pulsating power decoupling circuits, the main inverter shares partially or completely power switches with the decoupling cell.

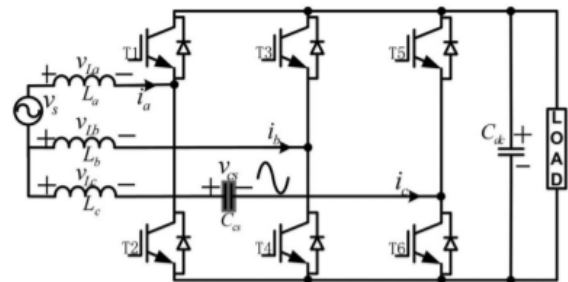
A switch-multiplexing circuit [57,58] derived from an independent decoupling circuit based on the H-bridge is shown in Figure 2.12a. The middle bridge-arm shared by the decoupling cell and the main converter has two functions: inversion/rectification, and pulsating power compensation. Thanks to this topology, two power switches have been saved. However, the voltage stresses may become higher, and the range of operating of DC-Link voltage is reduced. In Figure 2.12a, the dynamics of input and decoupling currents are independent. However, in the method proposed in Figure 2.12b [59,60], the dynamics of the

decoupling current and the voltage across the energy storage capacitor are coupled, which increases the complexity in the controller design.

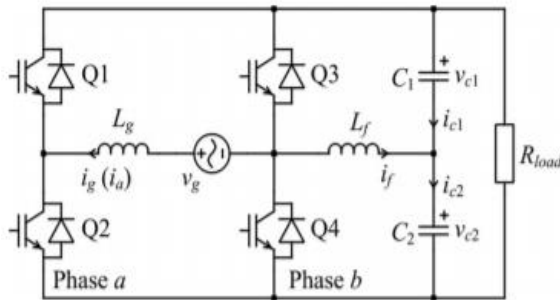
Other dependent decoupling circuits derived from independent circuit based on the Half-bridge converter are shown in Figure 2.12c [59], and in Figure 2.12d [60]. Their control methods are different because one of the capacitors is replaced by a DC source. In these topologies, no additional switches are used for decoupling cell. However, the voltage stress on power switches is higher. Care must therefore be taken with their thermal sizing.



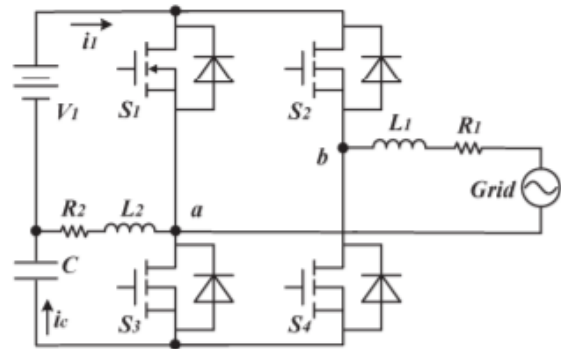
a. H-bridge converter [57]



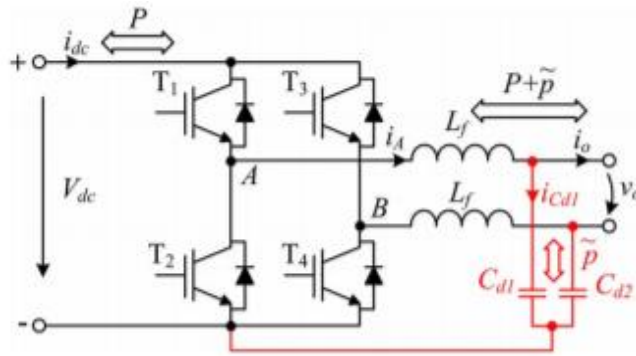
b. H-bridge converter [58]



c. Half-bridge converter [59]



d. Half-bridge converter [60]



e. Differential connection [61]

**Figure 2.12.** Schematics of the dependent pulsating power decoupling circuits.

Another switch-multiplexing topology has been proposed based on differential connection of AC/DC converters, which have the inherent capability of pulsating power decoupling. It will be obtained using control of the common mode voltages of the output filter capacitors (Figure 2.12e) [61,62]. Although in dependent topologies the number of switches is reduced, the complexity of modulation and control is increased. Moreover, the voltage stress may be increased in some topologies. Table 2.1 summarizes the main characteristics of these circuits.

**Table 2.1.** Comparison of several power decoupling circuits.

Ref.	Power rating	Additional switches, diodes	Efficiency	Connection	Feature and classification	
[41]	500W	4, 4	-	In parallel	Independent decoupling circuits (Flexible control and modulation)	A large number of switches, High voltage stress on decoupling circuit
[45]	20W	1, 2	84%	In parallel		Step-down voltage characteristic, High voltage stress on decoupling circuit
[49]	250W	2, 2	88%	In parallel		Step-up voltage characteristic, High voltage stress on decoupling circuit
[51]	1kW	2,2	-	In parallel		Flexible voltage range, High switches voltage stress
[55]	2kW	4,4	-	In series		A large number of switches and diodes, Low voltage stress on switches

[58]	4kW	2, 2	-	In parallel	Dependent decoupling techniques (Increasing control and modulation complexity)	Additional switches and diodes, Limited operating range, Increasing voltage stress
[59]	1kW	-	93.8%	-		No additional switches and diodes, Increasing switches voltage stress
[60]	500W	-	93.2%	-		No additional switches and diodes, Increasing switches voltage stress
[61]	1kW	-	90%	Differential connection		No additional switches and diodes, Introducing distortion to grid current

As a consequence, although in the dependent techniques the number of switches has been reduced, the decoupling cell cooperates with the compensator and the main converter. This leads to complexity in the modulation and control and also increasing voltage stress on switches. Flexibility in control and modulation can be achieved with independent techniques to the detriment of increased number of switches.

Among independent techniques, the series decoupling cell has the following advantages: low power rating of the compensator, low voltage stress on switches, flexibility in control and modulation. Nonetheless, the series decoupling cell for the PV system [55] has so far only been used for a two-stage single-phase inverter.

### 2.2.3 PV voltage drop

The required DC-Link voltage for power injection to the grid can be obtained using the modulation index given in (2.5).

$$m_a = \frac{V_o}{V_{dc}} \quad (2.5)$$

where  $V_o$  is the grid voltage amplitude and  $V_{dc}$  the DC-Link voltage. Although the required  $V_{dc}$  can be decreased by increasing  $m_a$ , it is limited by the dead-time of the power

switches. In the single-stage PV inverter, the DC voltage is equal to the PV voltage that is influenced by solar irradiation, shading effect and panel temperature. Hence, if PV voltage drops beyond the lower limit, the inverter is stopped, and all the remaining power is lost. Thus, the PV voltage is limited and the maximum power may not be achieved by changes in irradiance and temperature that results in high power losses. It is one of the main drawbacks of single-stage PV inverters that should be addressed to increase the efficiency. However, to the best of our knowledge, the voltage drop compensation and the limited operating range of the single-stage inverters are not yet addressed.

### **2.3 Fault diagnosis methods in PV systems**

Regarding the importance of PV panels monitoring for safety and economic reasons, different methods have been proposed for diagnosis of PV faults. These methods can be classified in two categories based on information collection: passive methods and active methods. Passive methods use electrical and environmental measurements on the DC side. This information is already available, and they include DC current and voltage, power at MPP, irradiance and measurement.

On the other hand, the idea of active methods is analyzing of system response to an applied signal. Temperature is one of the most important environmental parameters influencing the performance of photovoltaic panels. Thus, temperature monitoring of PV modules plays an important role in efficiency analysis and power prediction. Electroluminescence (EL) [63,64] and Infrared thermography (IRT) [65-67] work based on analyzing the thermal energy emitted by an object. Since this energy is converted to temperature, it is used to show a thermographic image of temperature distribution [68]. However, EL needs specific test conditions and equipment such as thermal camera and silicon charged couple device camera, which makes it highly expensive [69]. It also requires a dark environment and the interruption of power production. The drawback of power production interruption can be solved using IRT, which can be operated in real time. An example of temperature distribution using IRT is shown in Figure 2.13 [67]. These methods have the advantage of locating the fault with a high accuracy.

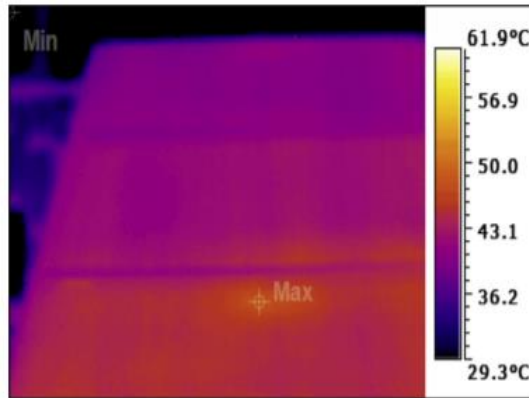


**Figure 2.13.** The temperature distribution analysis using IRT [67].

The I-V curve is a significant characteristic of PV modules that embeds valuable information on its health status. Several I-V tracers are commercially available, and therefore, several fault detection and diagnosis techniques have been developed based on the analysis of the I-V curve. However, because the I-V curve is very sensitive to environmental condition, an important preprocessing step is required before extracting fault signatures [70]. Among preprocessing techniques, principal component analysis is one of the most common multivariate statistical tools used for data representation. Thanks to its capability of retaining the most relevant information within a dataset, it has been applied for partial shading detection and classification based on the analysis of I-V curve [69].

There are other techniques that they require external excitation signals. Among them, time-domain reflectometry (TDR) is used to detect open-circuit faults [71] and spread spectrum time-domain reflectometry (SSTDR) is used for ground faults and PV arc faults [72].

They are based on reflectometry: a high frequency signal is injected into the circuit and the analysis of the reflected signal is used to evaluate the health status. Indeed, any impedance mismatch along the traveling line is responsible for the distortion of the reflected signal. Any variation in the reflected signal will be used to detect the fault type, and position. The difference between the two techniques is that TDR injects an analogue signal, while SSTDR injects a pseudorandom binary signal [73]. These techniques do not need an explicit model of the plant and they can be used even without solar irradiation. However, they cannot detect

partial shading. Besides, they require a specific external function generator, which makes them costly techniques.

Electrochemical impedance spectroscopy (EIS) is a fault diagnosis method that has already been used in different applications [74]. In the previous studies, impedance spectroscopy has been used for extracting the parameters of PV dynamic model [75,76] and more recently it has been used as a fault diagnosis tool in PV systems [77-83]. IS is based on the analysis of the PV panels impedance in the frequency domain. The conventional EIS has been presented based on frequency response analyzer, which is an offline method [84]. The idea is to inject of a small voltage/current at different frequencies into the PV system and estimate its impedance using the system response as shown in Figure 2.14 [77]. Thus, the PV dynamic model can be extracted, and its parameters used to analyze the solar panels operation under a wide range of conditions.

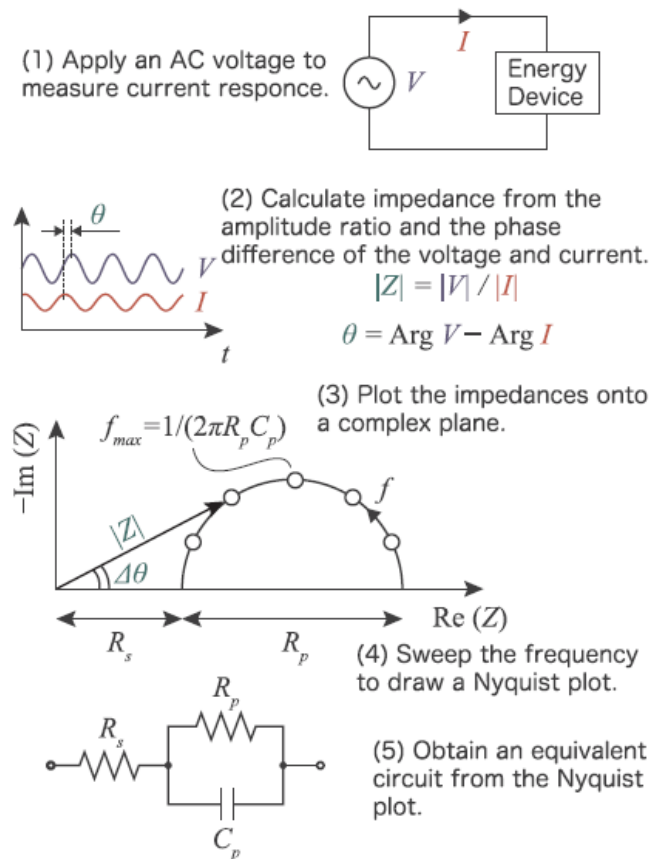


**Figure 2.14.** Schematic of the impedance spectroscopy measurement [77].

Hence, since it enables the estimation of the equivalent capacitor of PV panels, it may provide an additional information compared to DC current-voltage methods. IS method has been used to evaluate the fault conditions such as mechanical stress, potential induced degradation [78,79], and partial shading [80]. Also, different conditions have been considered such as bias voltages [81,82], series versus parallel connections [83], and different temperatures [84].

However, in all these methods an IS equipment is required, which represents an additional cost. Moreover, it requires to interrupt the power production to connect the equipment. Thus, an online method has been proposed by using the DC/DC converter in the PV system with the elimination of the additional impedance measurement tool [85]. The idea is to inject an additional low-frequency signal into the circuit and scan a sufficiently wide frequency range to extract the Nyquist diagram. To validate the proposed method, the impedance of the solar panel has been measured with an IS analyzer and used in the simulation model [85]. The proposed method depicted in Figure 2.15 [85] shows similar results to those obtained with IS equipment without the need for a separate excitation circuit. However, because of the high bandwidth in PV panels, the converter switching frequency must be high, which is a serious challenge for implementation especially in high power applications [80].

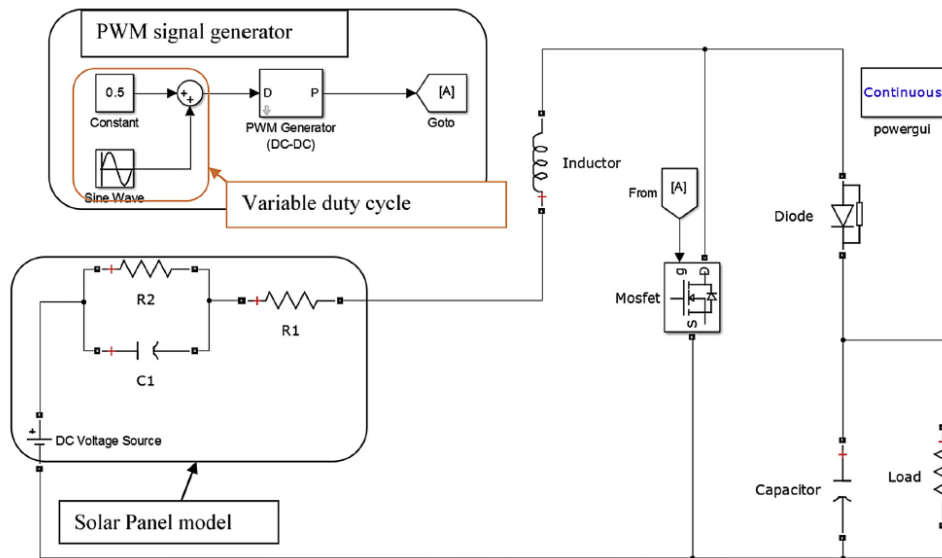


**Figure 2.15.** The proposed online impedance measurement method in [85].

## 2.4 Problem statement

The main issues in single-phase grid-connected PV systems particularly in single-stage ones and the current proposed solutions in various works have been investigated. These issues have been analyzed from three parts: control, pulsating power decoupling and voltage drop, and fault diagnosis. At first the features of various MPPT algorithms and grid current controllers have been discussed. Also, the general structure of control system for single-stage grid-connected PV systems has been studied. Consequently, important issues in control of single-stage grid-connected PV systems can be considered as easy implementation, fast dynamic response, robustness against parameter mismatches and model uncertainties, high grid current quality and coordination of grid and PV sides controllers. As a result, a new direct power control with constant switching frequency is proposed. The proposed method can overcome the drawbacks of the previously mentioned control methods such as being model-based and low robustness, control complexity and the infinite transient response. Also, based on the advantages of the P&O algorithm such as easy implementation and good performance, a new P&O method has been proposed to be adopted with the proposed DPC method.

Another important issue is pulsating power and limited operating voltage range in the single-stage PV systems. Although a single-stage grid-connected system offers higher efficiency and lower cost and size, it suffers from lower operating range due to low irradiance conditions. This problem leads to PV voltage drop, and consequently to inverter shutdown and loss of the total injected power. Hence, structures and procedures that can overcome this problem gain interest in single-stage configurations. Besides, especially for low power single-phase systems, pulsating power is an additional handicap. The pulsating power is a major problem in both single and two-stage systems and many techniques have been proposed to overcome this issue. To address these issues in a single-stage grid-connected PV system, a dual-function decoupling circuit is proposed. It compensates the pulsating power and increases the system's lifetime by replacing electrolytic capacitors with film capacitors. In addition, the proposed system offers a low power voltage compensator to overcome the voltage drop due to the shading and therefore, prevents the inverter from shutting down, and increases the operating range. As a result, the proposed compensator is called "hybrid

compensator”. The circuit operation is based on a controlled series voltage source between the PV module and the DC-Link. Therefore, both the aforementioned critical issues about single-stage PV inverters are fully addressed with the equivalent low power circuit, a simple structure and control unit. To sum up, the proposed hybrid compensator is the only one among the decoupling circuits that can achieve the following contributions, simultaneously:

- Pulsating power elimination,
- Voltage recovery capability to compensate PV voltage drop

The last important issue that has been addressed is monitoring and fault diagnosis of the PV systems. In the recent years and regarding the importance of system monitoring and fault detection, different techniques have been proposed for PV panel fault diagnosis. These methods have their pros and cons. However, most of them require additional equipment such as thermal camera, a specific external function generator or I-V curve tracer, and impedance spectroscopy analyzer. To overcome this issue, a new fault diagnosis method has been proposed for the single-phase PV systems. The method is based on the use as an impedance measurement tool of the active power decoupling circuit that eliminates pulsating power on the DC side. In other words, we have taken the benefit of pulsating power decoupling circuit as impedance spectroscopy tool without using any additional equipment. The proposed method includes a low power high frequency circuit that operates as an online impedance spectroscopy with no need to interrupt PV power production.

## **Chapter 3 Proposed control system for single-phase PV systems**

### 3.1 Modified P&O algorithm

Regarding the advantages of P&O algorithm such as high accuracy in MPP tracking, simplicity and easy implementation, a power-based P&O algorithm is proposed. The modified algorithm directly provides the reference of active power instead of voltage or current. Therefore, the proposed MPPT algorithm can be adopted with power control methods and so, internal control loops are removed to speed up the dynamic response.

In the modified P&O algorithm, firstly, the PV voltage and current are measured and the output power is calculated. Secondly, an initial power reference is selected and a power perturbation ( $\Delta P$ ) is introduced. Then, based on P-V curve in Figure 2.3, we have:

$$\text{At the left of the MPP, } \frac{dP_{pv}}{dV_{pv}} > 0 \rightarrow P_{oref}(k) = P_{oref}(k-1) - \Delta P \quad (3.1)$$

$$\text{At the right of the MPP, } \frac{dP_{pv}}{dV_{pv}} < 0 \rightarrow P_{oref}(k) = P_{oref}(k-1) + \Delta P \quad (3.2)$$

Finally, at the MPP,  $\frac{dP_{pv}}{dV_{pv}} = 0$  and the algorithm is stopped. The flowchart of the modified P&O algorithm with output power reference is shown in Figure 3.1.

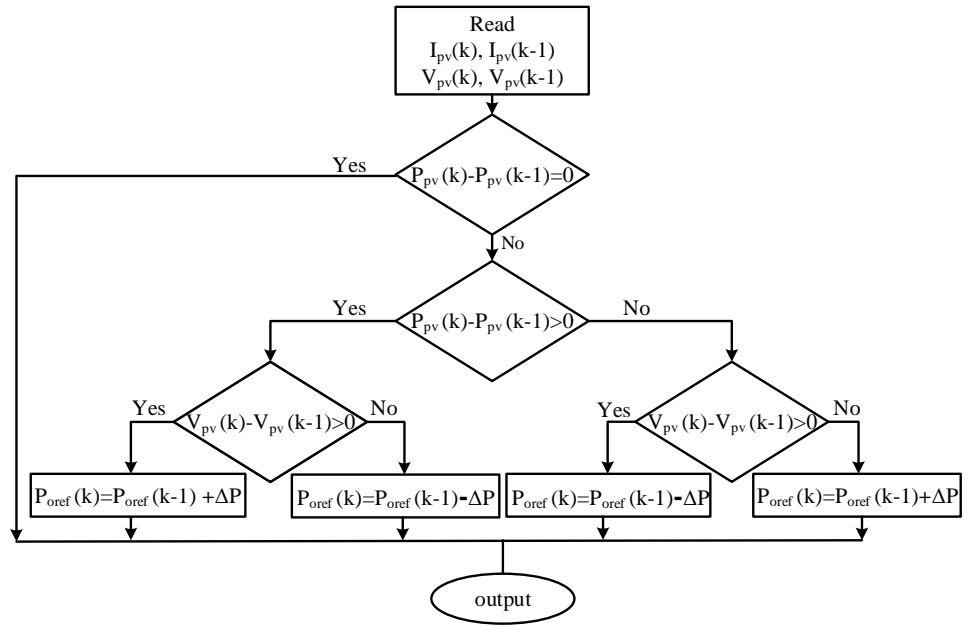


**Figure 3.1.** Flowchart of the MPPT algorithm with power output.

## 3.2 Power Control Strategy

### 3.2.1 System description

The schematic of the single-stage single-phase PV system is depicted in Figure 3.2. The outer control loop sampled at a low frequency implements the MPPT using the proposed P&O algorithm. Its output is the active power reference  $P_{oref}$  and in order to operate at a unit power factor, the reactive power reference  $Q_{oref}$  is set at 0.

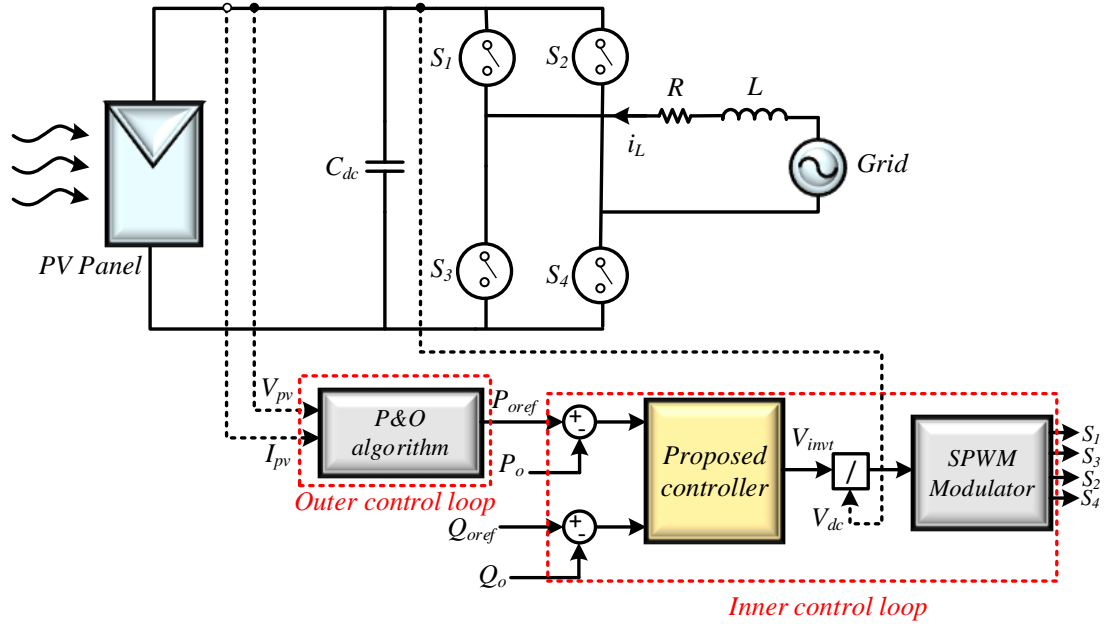


**Figure 3.2.** The general structure of the system with FTSMC.

The inner control loop is based on a sinusoidal pulse width modulator (SPWM) to generate the converter switching signals. Its sampling frequency is set higher enough ( $>20$  compared to the grid fundamental frequency) [86]. Therefore, the output voltage of the inverter can be assumed equal to its fundamental component. Consequently, the equivalent circuit in the stationary reference frame ( $\alpha\beta$ ) is displayed in Figure 3.3.

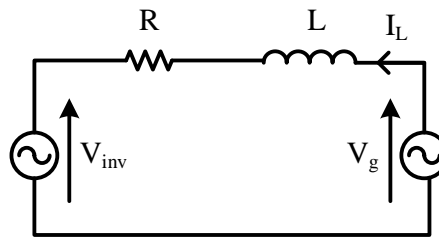


**Figure 3.3.** The equivalent circuit of the single-phase grid-tied inverter.

Based on Figure 3.3, the voltage equation can be written as:

$$V_{g\alpha\beta} = RI_{L\alpha\beta} + L \frac{dI_{L\alpha\beta}}{dt} + V_{inv\alpha\beta} \quad (3.3)$$

where  $V_{g\alpha\beta}$  is the grid voltage and  $V_{inv\alpha\beta}$  is the average output voltage of the inverter,  $R$  and  $L$  are the grid line parameters, respectively.

The instantaneous apparent, active and reactive powers can be computed as:

$$\begin{aligned}
 S_o &= -\frac{1}{2}V_{g\alpha\beta}I_{L\alpha\beta}^* \\
 P_o &= -\frac{1}{2}(v_{g\alpha}i_{L\alpha} + v_{g\beta}i_{L\beta}) \\
 Q_o &= -\frac{1}{2}(v_{g\beta}i_{L\alpha} - v_{g\alpha}i_{L\beta})
 \end{aligned} \tag{3.4}$$

where  $v_{g\alpha}, v_{g\beta}, i_{L\alpha}, i_{L\beta}$  are the grid voltage and current components in the  $\alpha\beta$  reference frame, respectively. In order to obtain these components from the measurements, a PLL is required. Thus, a PLL structure based on the SOGI is adopted to retrieve the stationary components [31]. This method is an advanced and popular method, which can simply transfer the current and voltage to the stationary reference frame.

### 3.2.2 Fast terminal sliding mode control

#### 3.2.2.1 General description

Sliding mode control is a well-known and popular method for the robust control of non-linear systems [87]. The first step in designing the SMC is the selection of a sliding surface. Once the states reach the surface, they slide along it. Therefore, the sliding surface and its derivative, which is a linear function of the error, are equal to zero. In closed-loop systems, the error must converge to the surface and remain there. Thus, in such systems, the slip surface is usually defined as the error, the derivative or the integral of the error. The next step is to define the control law. For this purpose, the derivative of the slip surface is set to zero and the uncertainties must be considered in its design. Finally, the stability analysis of the controller must be performed.

In direct power control, the objective is to minimize the error between the power references (active and reactive) and their actual values despite the disturbances, the unavoidable parameter mismatch, and the modelling errors.

The addition of the error integral to design the surface reduces the steady state error and mitigates the chattering phenomenon. For the conventional SMC, the sliding surface is expressed as:

$$S_{SMC} = \left(\frac{d}{dt} + \lambda\right)X_1 \quad (3.5)$$

where  $X_1 = \int e(\tau)d\tau$ ,  $e(t)$  is the output power error and  $\lambda$  is a time-invariant coefficient.

The solution of (3.5) in steady state is expressed as:  $X_1(t) = X_1(t_0)e^{-\lambda t}$ . Therefore as  $X_1$  represents the error, the convergence time is infinite. Increasing the coefficient  $\lambda$  may improve the transient but to the detriment of more chattering and will not prevent from the steady state error. To address this issue, terminal sliding mode control has been proposed as an alternative [35].

The sliding surface is defined as:

$$S_{TSMC} = \dot{X}_1 + \delta X_1^{\frac{r}{l}} \quad (3.6)$$

where  $r, l$  are positive odd integers and  $\delta$  is a positive integer. In this case  $X_1$  will reach its equilibrium point in an adjustable finite time expressed as:

$$t_s^{TSMC} = \frac{l}{\delta(l-r)} |X_1(t_0)|^{(1-\frac{r}{l})} \text{ under the condition that } l > r. \text{ However, it is noticeable that the}$$

convergence time also depends on the value of the initial point. In order to mitigate this effect, fast terminal SMC is introduced. In this case, the sliding surface consisting of a linear term and a non-linear term, is now defined as:

$$S_{FTSMC} = \dot{X}_1 + \delta X_1^{\frac{r}{l}} + \gamma X_1 \quad (3.7)$$

where  $\gamma$  is a positive integer bringing in an additional linear term. With such a sliding surface when the states of the system are not near the equilibrium point ( $|X_1| > 1$ ) the dynamic of system is obtained as  $\dot{X}_1 = -\gamma X_1$ , and when they are close to the equilibrium point ( $|X_1| < 1$ ), the dynamic of system is  $\dot{X}_1 = -\delta X_1^{\frac{r}{l}}$ . Then, whatever the distance to the operating point, it results in a faster dynamic response [37]. The expression of the convergence time is  $t_s^{FTSMC} = \frac{l}{\delta(l-r)} (\ln(\gamma X_1(t_0)^{(1-\frac{r}{l})} + \delta) - \ln \delta)$  under the condition that  $l > r$ .

### 3.2.1. Application of FTSMC to power control

#### 3.2.1.1. Definition of the sliding surfaces

If we define  $e_p = P_{oref} - P_o$ ,  $e_Q = Q_{oref} - Q_o$ , the sliding surfaces for the active and reactive powers can be written as:

$$S_t = [S_{tP} \quad S_{tQ}]^T$$

$$S_{tP} = e_p(t) + \gamma_p \int e_p(\tau) d\tau + \delta_p \left( \int e_p(\tau) d\tau \right)^{\frac{r}{l}}$$

$$S_{tQ} = e_Q(t) + \gamma_Q \int e_Q(\tau) d\tau + \delta_Q \left( \int e_Q(\tau) d\tau \right)^{\frac{r}{l}} \quad (3.8)$$

where  $(.)^T$  is the transpose operator.

#### 3.2.1.2. Derivation of the control law

The control law is composed of two terms: the equivalent control law  $V_{invt(eq)}$  obtained by setting  $S_t = 0$  and  $\dot{S}_t = 0$ , the discontinuous or switching control law  $V_{invt(sw)}$  designed to compensating the disturbances that deviate the states from the sliding surface. Finally  $V_{invt} = V_{invt(eq)} + V_{invt(sw)}$ .

The derivatives of the active and reactive surfaces are expressed as follows:

$$\begin{aligned}\dot{S}_{iP} &= \dot{e}_P + \gamma_p e_P + \frac{r}{l} \delta_p \left( \int e_P(\tau) d\tau \right)^{\frac{r}{l}-1} e_P \\ \dot{S}_{iQ} &= \dot{e}_Q + \gamma_q e_Q + \frac{r}{l} \delta_q \left( \int e_Q(\tau) d\tau \right)^{\frac{r}{l}-1} e_Q\end{aligned}\quad (3.9)$$

After some simplifications, they are expressed as (3.10).

$$\begin{aligned}\dot{S}_{iP} &= -\dot{P}_o + \gamma_p (P_{oref} - P_o) + \frac{r}{l} \delta_p \left( \int (P_{oref} - P_o) d\tau \right)^{\frac{r}{l}-1} (P_{oref} - P_o) \\ \dot{S}_{iQ} &= -\dot{Q}_o + \gamma_q (Q_{oref} - Q_o) + \frac{r}{l} \delta_q \left( \int (Q_{oref} - Q_o) d\tau \right)^{\frac{r}{l}-1} (Q_{oref} - Q_o)\end{aligned}\quad (3.10)$$

The derivatives of the active and reactive powers are required to obtain the control law through the derivative of the sliding surfaces. They are computed using (3.3) and (3.4):

$$\begin{aligned}\frac{dP_o}{dt} &= -\frac{1}{2L} [(v_{g\alpha}^2 + v_{g\beta}^2) - (v_{g\alpha} v_{inv\alpha} + v_{g\beta} v_{inv\beta})] - \frac{R}{L} P_o - \omega Q_o \\ \frac{dQ_o}{dt} &= -\frac{1}{2L} [-v_{g\beta} v_{inv\alpha} - v_{g\alpha} v_{inv\beta}] - \frac{R}{L} Q_o + \omega P_o\end{aligned}\quad (3.11)$$

The derivative  $\dot{S}_t$  is retrieved from (3.10) and (3.11). It can be written as:

$$\begin{aligned}\dot{S}_t &= A_t + B_t V_{invt}, \\ A_t &= [A_{iP} \quad A_{iQ}]^T, B_t = \frac{-1}{2L} \begin{bmatrix} v_{g\alpha} & v_{g\beta} \\ v_{g\beta} & -v_{g\alpha} \end{bmatrix} \\ A_{iP} &= \frac{R}{L} P_o + \omega Q_o + \frac{1}{2L} (v_{g\alpha}^2 + v_{g\beta}^2) + \gamma_p (P_{oref} - P_o) + \frac{r}{l} \delta_p \left( \int (P_{oref} - P_o) d\tau \right)^{\frac{r}{l}-1} (P_{oref} - P_o) \\ A_{iQ} &= \frac{R}{L} Q_o - \omega P_o + \gamma_q (Q_{oref} - Q_o) + \frac{r}{l} \delta_q \left( \int (Q_{oref} - Q_o) d\tau \right)^{\frac{r}{l}-1} (Q_{oref} - Q_o)\end{aligned}\quad (3.12)$$

Setting  $\dot{S}_t = 0$  allows determining the equivalent control law  $V_{invt(eq)} = -B_t^{-1} A_t$ . In order to cope with the disturbances, the additional term that is the switching control law is

set as  $V_{invt(sw)} = -B_t^{-1}k_t sign(S_t) = -B_t^{-1} \begin{bmatrix} k_1 & 0 \\ 0 & k_2 \end{bmatrix} \begin{bmatrix} sign(S_{tP}) \\ sign(S_{tQ}) \end{bmatrix}$  where  $k_1, k_2$  are positive coefficients.

The final control law  $V_{invt} = V_{invt(eq)} + V_{invt(sw)}$  is applied to the sinusoidal pulse width modulator to determine the gate signals of the inverter. As a result, in the proposed FTSMC method, the control law is composed of two terms;  $V_{invt(eq)}$  and  $V_{invt(sw)}$ . So, not only the output of *Sign* function is very low but also, the output inductor filter can be used to minimize as low as possible the chattering effect of this term. In addition, the final control law is calculated and fed to the pulse width modulator with constant switching frequency that can effectively cope with the chattering issue and high frequency components.

One can notice from (3.12) that we have at our disposal the adjustable coefficients to minimize the steady state error and improve the dynamic performance.

Let us remind that the proposed MPPT algorithm calculates the active power reference, which removes internal control loops and the reactive power reference can be set to zero. The block diagram of the proposed controller is shown in Figure 3.4.

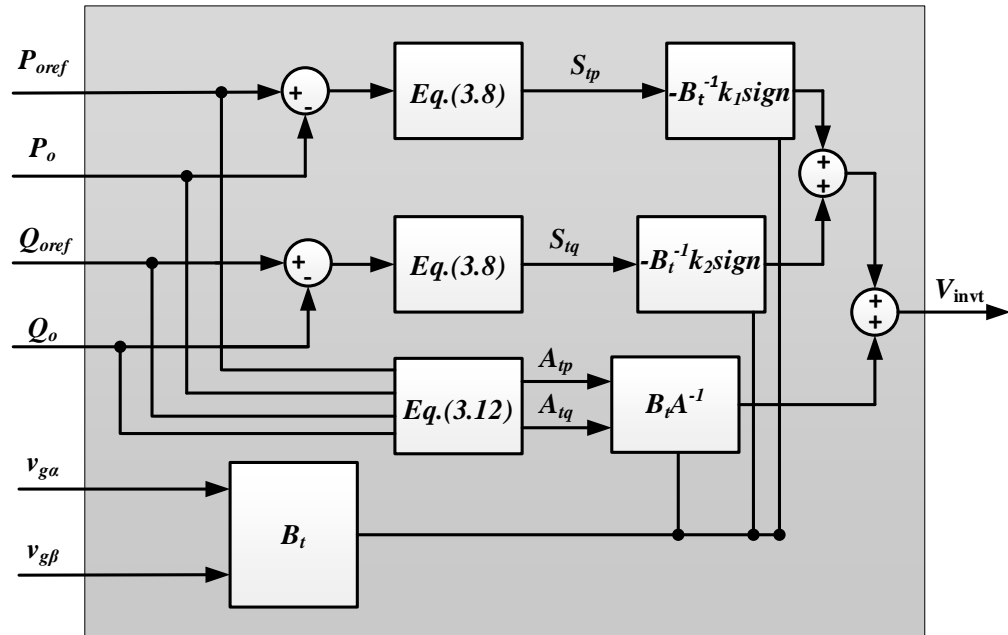


**Figure 3.4.** Block diagram of the proposed FTSMC.

### 3.2.2.2 Stability analysis

Once the states are attracted on the sliding surface, it is important to evaluate the stability of the control law. This is done with the help of Lyapunov theorem on stability. The Lyapunov function in our case is defined as  $V_t = \frac{1}{2} S_t^T S_t$ . The stability is guaranteed if the condition  $\dot{V}_t = S_t^T \dot{S}_t < 0$  is satisfied.

From (3.12), the following stability condition is derived:

$$\dot{V}_t = S_t^T \dot{S}_t = -k_t S_t^T \text{sign}(S_t) < 0 \quad (3.13)$$

As  $k_t > 0$ , the system is stable if  $S_t^T \text{sign}(S_t) > 0$ .

#### 3.2.1.3. Parameters selection

The parameters used in the definition of the sliding surface (3.8) must be set to obtain good dynamic performance such as minimum settling time and steady state error. The parameters  $r, l$  are odd integers and must be set to avoid singularity, meaning that  $S_t \rightarrow 0$  while the control variable must be bounded. Based on a recursive procedure [37], the minimum values of  $r, l$  are set as:

$r = 3$ , and  $l = 5$ . The parameters  $\gamma_{P,Q}, \delta_{P,Q}$  must be set at highest values to reduce the settling time. In the following, they are set at  $\gamma_{P,Q} = 10000$  and  $\delta_{P,Q} = 10000$ . The last parameters to be set are the coefficients in  $k_t$ . They must be set to reject efficiently the disturbances within the system without increasing the inherent chattering phenomenon [88].

Let us define the disturbances as  $D = [D_P \quad D_Q]^T$ . If we include the disturbance in the derivative of the sliding surface defined in (3.12),  $\dot{S}_t = A_t + B_t U + D$  and the stability condition becomes:

$$\dot{V}_t = S_t^T \dot{S}_t = S_t^T D - k_t S_t^T \text{sign}(S_t) < 0 \quad (3.14)$$

To guarantee the stability of the system on the sliding surface, the following condition must be satisfied:

$k_t > D$ . Once the designer has estimated the disturbances affecting the active and reactive powers, he can tune appropriately his switching control coefficients.

### 3.3 Simulation results of the control system

At first, to evaluate our proposal, we have simulated with Matlab-Simulink® a single-stage single-phase grid-connected PV system that is shown in Figure 3.5. The system parameters are listed in Table 3.1. It is composed of a PV array model with parameters listed in Table 3.2, a single-phase inverter, a 110V-220V transformer (for grid connection) and an inductance. The latter has been selected as recommended in [89]. Because of the transformer, 110V is considered as the grid voltage ( $v_g$ ). The parameters of the controller are listed in Table 3.3. They have been set as explained in the previous section.

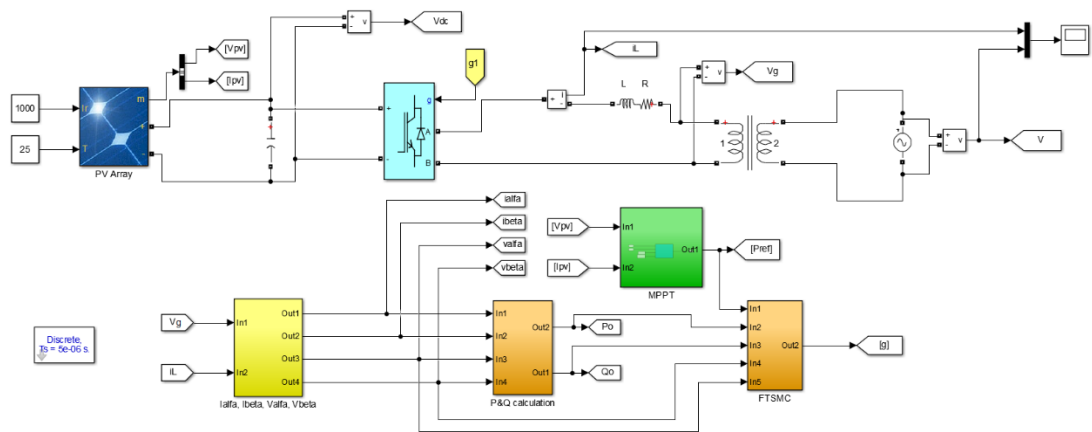


**Figure 3.5.** The simulated system with FTSMC in Matlab-Simulink.

**Table 3.1.** The parameters of system with FTSMC.

Parameter	Description	Value
$V_g$	Grid voltage	110 (rms)
$f$	Grid frequency	50 Hz
$f_{sw}$	Switching frequency	6 kHz
$f_{sampling}$	Sampling frequency	12 kHz
$L$	Filter inductance	3.25 mH
$R$	Filter resistance	10 m $\Omega$

**Table 3.2.** Specifications of the PV module (APOS Energy AP210)

Parameter	Description	Value
$P_{mpp}$	Maximum PV power	209.85 W
$V_{mpp}$	Voltage at maximum power	28.63 V
$I_{mpp}$	Current at maximum power	7.33 A
$V_{oc}$	Open circuit voltage	36.55 V
$I_{sc}$	Short circuit current	7.79 A
$n_s$	Series-connected modules per string	7
$n_p$	Parallel strings	1

**Table 3.3.** The proposed FTSMC parameters.

Parameter	Value
$k_1, k_2$	5000
$\frac{r}{l}$	0.6
Control coefficients of $\gamma_p, \gamma_q, \delta_p, \delta_q$	10000

### 3.3.1 Simulation results in steady state condition

The FTSMC-DPC strategy is first evaluated in steady state. The reference of the active power is obtained from MPPT under  $1000W/m^2$  solar radiation and temperature of  $25^{\circ}C$ . The reactive power reference is set to 0Var. The simulation results are shown in Figures 3.6 and 3.7. In Figure 3.6 from top to bottom one can see that the active and reactive powers are perfectly controlled. Besides, the maximum power of PV panels is properly tracked using the proposed MPPT. The last two waveforms represent the voltage (220V side) and the grid

current. In Figure 3.7, the grid current spectrum is plotted. The THD is equal to 2.97%, which copes with the international standard IEC62040-3 that recommends a THD < 5%.

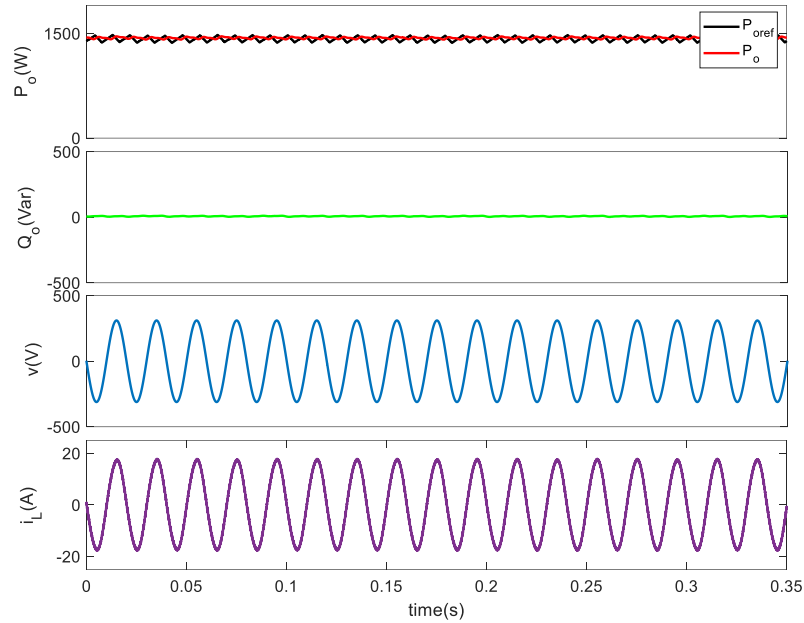


**Figure 3.6.** Simulation results of the FTSMC in steady state condition.

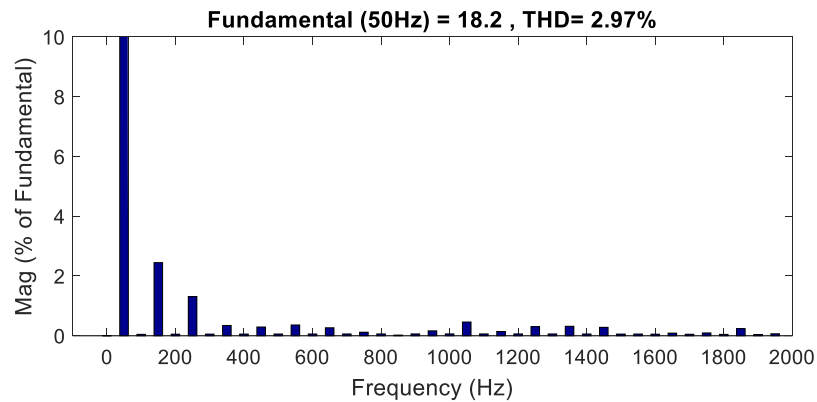


**Figure 3.7.** Grid current harmonic spectrum in the simulated system with FTSMC.

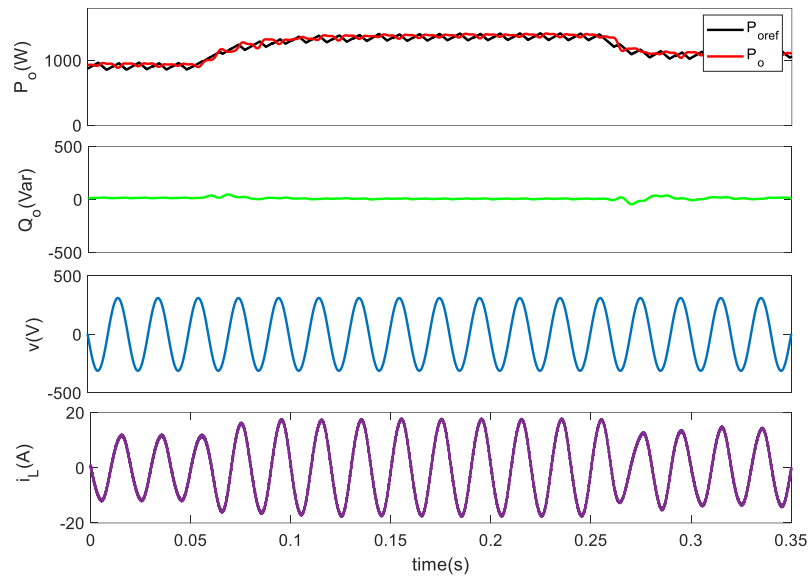
### 3.3.2 Simulation results in transient conditions

The FTSMC-DPC strategy is also evaluated in transient conditions. The results are plotted in Figure 3.8 and Figure 3.9 with from top to bottom, the active power, the reactive power, the voltage, and the grid current.

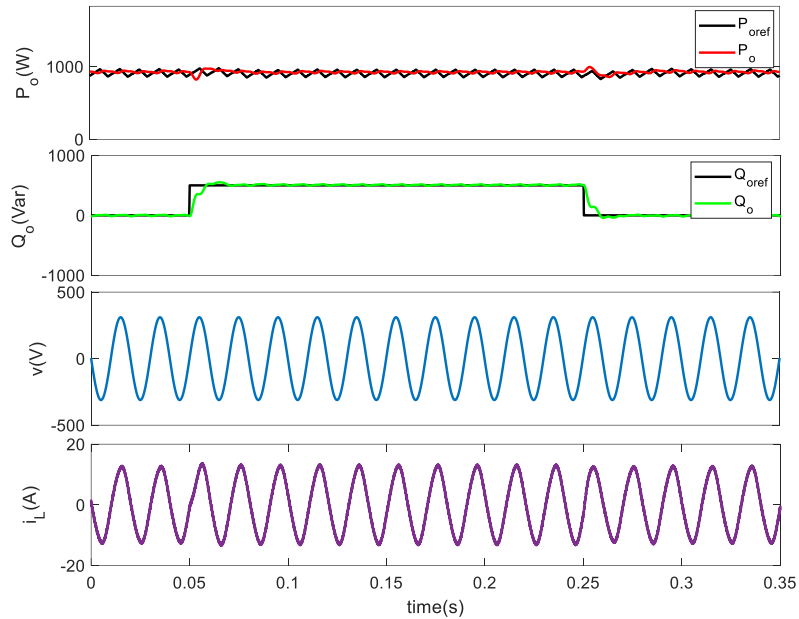
Figure 3.8 corresponds to solar radiation step changes ( $600-1000-750W/m^2$ ). The results show the fast response of the controller for maximum power tracking with almost no overshoot and a null steady state error.

Figure 3.9 corresponds to reactive power step changes. The results show a time response  $t_r = 8ms$  for reactive power tracking with almost no overshoot and a null steady state error.

In both cases, one can notice the good decoupling between the two power loops and the fast transient response for the grid current.



**Figure 3.8.** Simulation results of the FTSMC with active power step changes.



**Figure 3.9.** Simulation results of the FTSMC with reactive power step changes.

### 3.4 Experimental results of the control system

The experimental test bench is shown in Figure 3.10. An adjustable DC source fed from a three-phase rectifier is used to emulate the PV source. The single-stage inverter is composed of IGBT power switches IKW40N120H3 (40A/1200V) driven with HCPL3120 optocoupler gate drivers. The control algorithm is implemented in the TMS320F28335, a DSP from Texas Instruments. This DSP-based board provides several high-resolution enhanced Pulse Width Modulators with output buffers and multi-channel high-speed 12-bit analog to digital converters, which make it highly applicable for power electronics applications. A prototype driver board via HCPL3120 optocoupler and maximum 2.5A peak current has been designed to control the power switches.

Hall effect sensors, LTS25NP and LV25P are used to measure the current and the voltage, respectively.

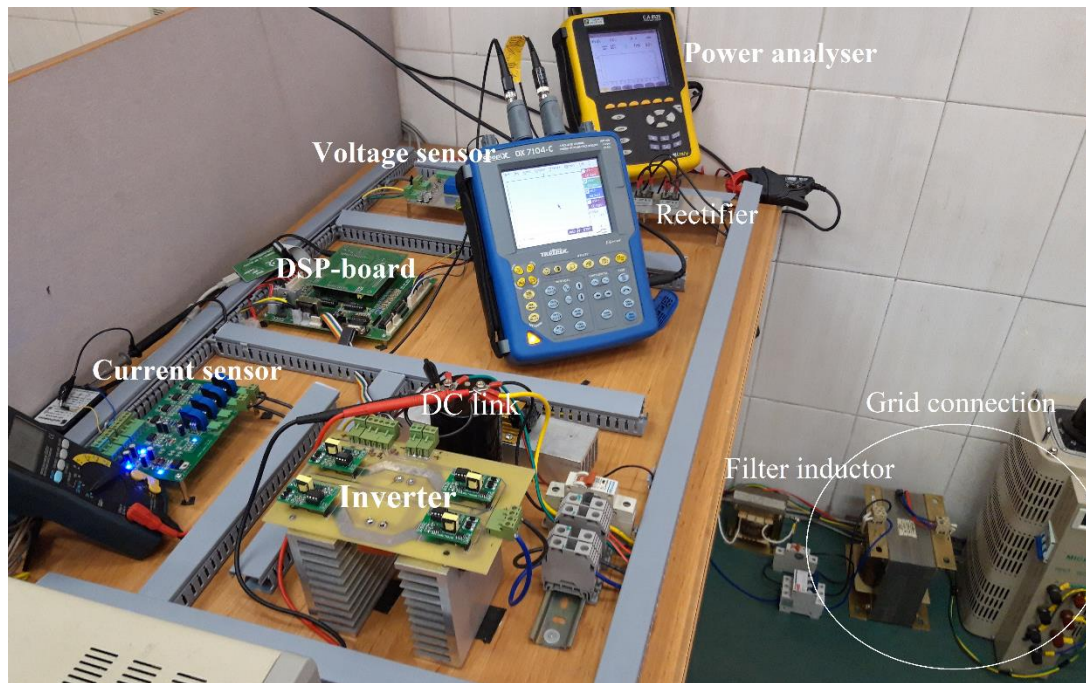


**Figure 3.10.** The experimental setup for FTSMC.

### 3.4.1 Experimental results in steady state

The experimental results in steady state are displayed in Figure 3.11. The active power is equal to 1kW while the reactive power is almost null (given the actual value that is not zero as it can be observed from the power factor). One can also notice the sinusoidal waveforms of the grid voltage and current. Figure 3.12 represents the grid current spectrum. It shows a THD equal to 3.5% still compliant with the international standard.

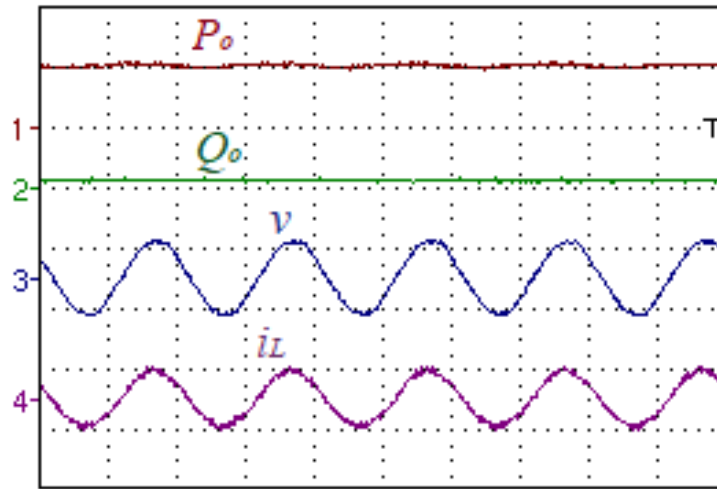


**Figure 3.11.** Experimental results of the FTSMC in steady state condition; time: (10ms/div),  $P_o$  (1000 W/div),  $Q_o$  (500 VAR/div),  $v$  (500V/div), and  $i_L$  (26A/div).

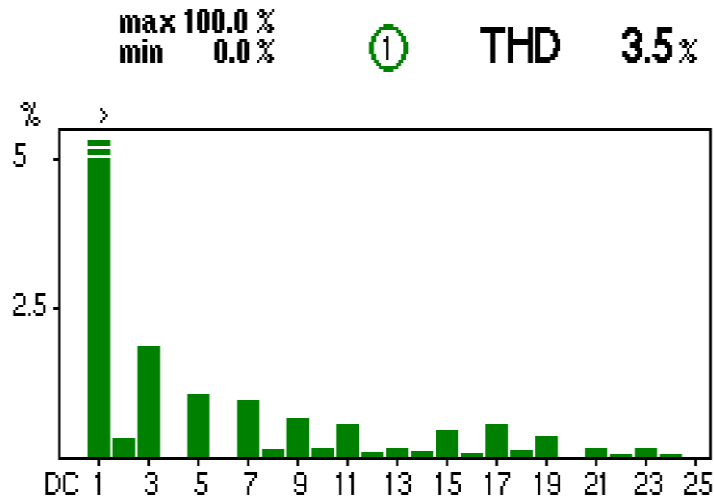


**Figure 3.12.** Experimental Grid current harmonic spectrum for FTSMC.

### 3.4.2 Experimental results in transient operation

To evaluate the performance of the controller in case of solar radiation changes due for example to clouds, stepwise variations from 50% to 100% and back to 50% of the nominal value of the active power reference are introduced. The results are plotted in Figure 3.13. The

power tracking performance is very good with almost no overshoot and a time response of 10 ms. The transient on the grid current is negligible and there is no perturbation in the grid voltage.

The controller is also evaluated in case of reactive power changes due to grid requirements. The results are plotted in Figure 3.14. The same conclusions can be drawn as before.

Moreover, the performance during the transients is better than with other methods [27-29]. From the previous results, one can also notice the good decoupling capability of the proposed controller. The two power loops (active and reactive) are almost independently controlled.

A change of  $\pm 25\%$  in the inductance value is introduced in the model to verify the robustness of the proposed controller. The results plotted in Figure 3.15 show a good robustness with a THD of the grid current equal to 3.7% compared to 3.5% when there is no parameter mismatch. The dynamics of the power tracking are unchanged.

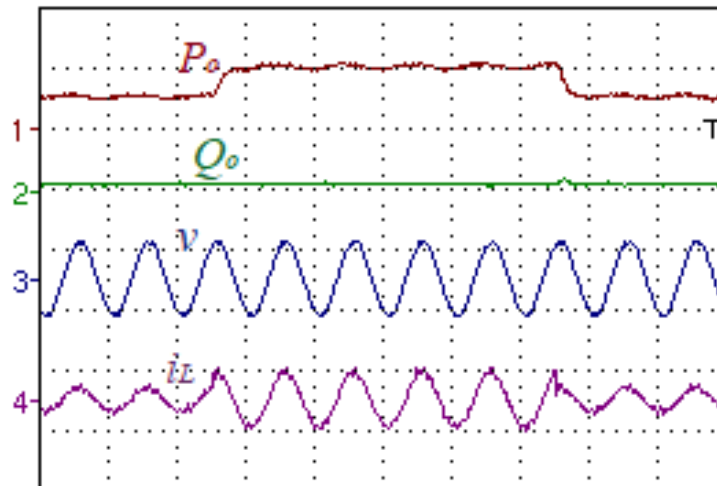


**Figure 3.13.** Experimental results of the FTSMC with active power step changes; time: (20ms/div),  $P_o$  (1000 W/div),  $Q_o$  (500 VAR/div),  $v$  (500V/div), and  $i_L$  (26A/div).

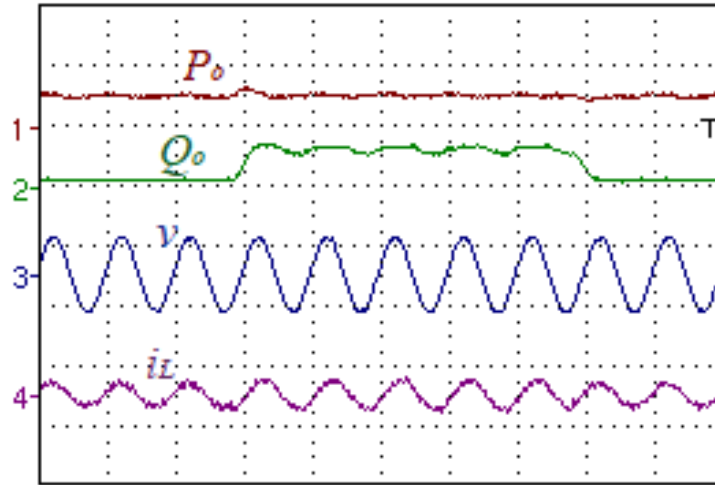


**Figure 3.14.** Experimental results of the FTSMC with reactive power step changes; time: (20ms/div),  $P_o$  (1000 W/div),  $Q_o$  (500 VAR/div),  $v$  (500V/div), and  $i_L$  (26A/div).

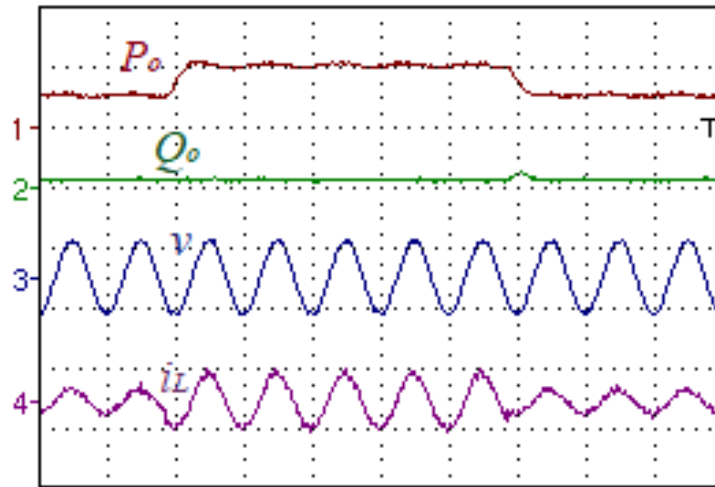


**Figure 3.15.** Experimental results of the FTSMC with mismatches in filter inductor; time: (20ms/div),  $P_o$  (1000 W/div),  $Q_o$  (500 VAR/div),  $v$  (500V/div), and  $i_L$  (26A/div).

### 3.4.3 Comparison of experimental performance

Finally, a comparison of experimental results is done with deadbeat-DPC method [27], deadbeat predictive controller [28] and a power hysteresis control scheme with dynamic performance improvement [29]. The results are summarized in Table 3.4. We can particularly

notice a lower THD of the grid current for our method. In order to compare the dynamic performance while the rate of active power variation is different, we have computed the relative time response defined as  $\frac{t_r}{\Delta P_o \%}$ . The results show that our proposal exhibits the best performance.

**Table 3.4.** Comparison of experimental performance of the proposed FTSMC with other control methods.

Reference	Proposed method	[27]	[29]	[28]
Grid voltage ( $V_g$ )	110	70	110	60
S (kVA)	1	1	1	0.5
$f_{sw}$ (kHz)	6	5	5	2.5
$f_{sampling}$ (kHz)	12	5	-	5
Filter inductor (mH)	3.25	3.7	5.6	5
$\frac{t_r}{\Delta P_o \%}$ (ms)	0.1	2	0.4	0.4
Grid current THD (%)	3.5	3.9	6.81	4.63

### 3.5 Conclusion

In this chapter a fast terminal sliding mode –direct power controller has been designed for the control of a single-stage single-phase PV grid-connected system. Besides, a MPPT algorithm has been proposed to be included in the power controller. Simulation and experimental results have shown that the proposed controller provides:

- a fast transient response (less than half a cycle of the grid period), which is essential for active or reactive power injection into the grid,
- a good power quality with a low THD of the grid current (3.5%), compliant with the international standard,
- a good decoupling capability of the two power control loops,
- a good coordination between the grid and PV controllers.

The results have also shown that the controller can cope with irradiation change and is robust to the inductor parameter mismatch.

A comparison with other conventional methods has shown the superiority of our proposal with higher dynamics and better power quality.

## **Chapter 4 Proposed dual- function pulsating power and voltage drop compensator for single-stage PV systems**

## 4.1 Dual-Function Power Decoupling Circuit

The proposed hybrid compensator is shown in Figure 4.1. The compensator consists of a two-port isolated DC/DC converter and a DC/AC converter. The main idea is based on equation (1.5); by compensating the voltage ripple, a larger voltage ripple can be allowed on the DC bus and thus the capacitor value  $C_{dc}$  can be reduced.

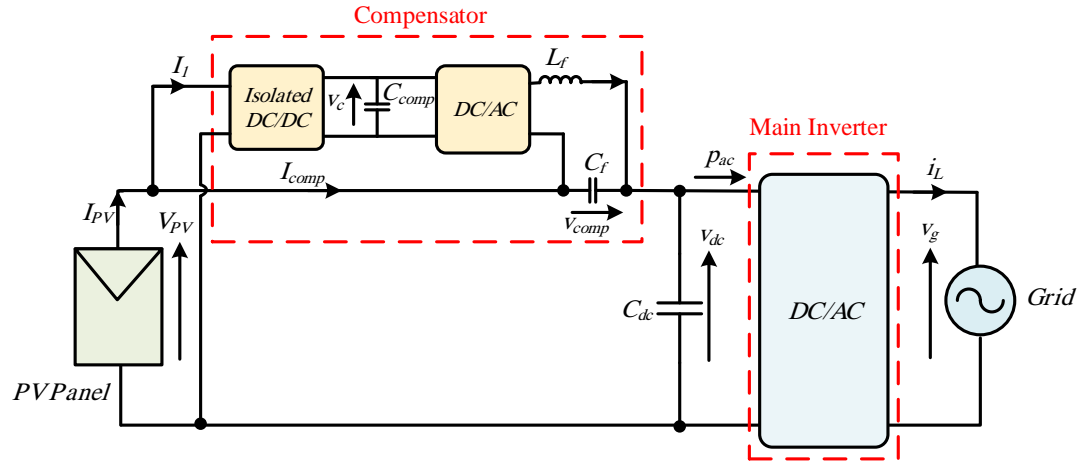


**Figure 4.1.** General structure of the single-stage grid-connected PV inverter with hybrid compensator.

### 4.1.1 Operating Modes of the system

According to Figure 4.1, the PV voltage can be written as follows:

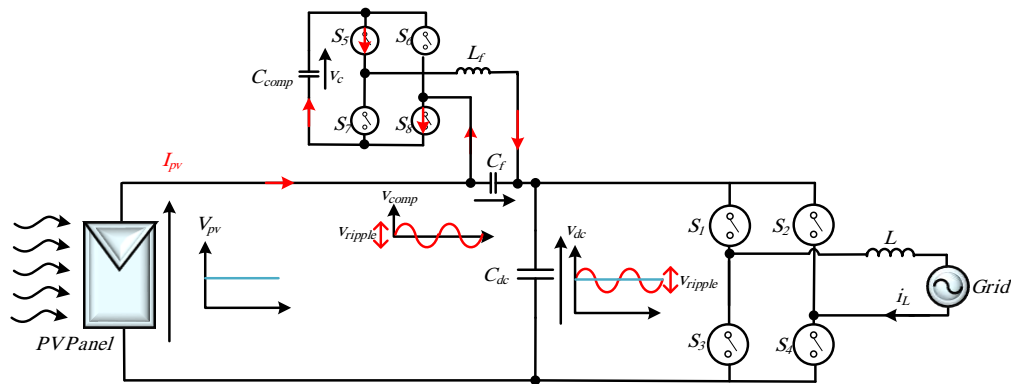
$$V_{pv} = v_{dc}(t) - v_{comp}(t) \quad (4.1)$$

where  $v_{comp}(t)$  is the voltage injected by the compensator. Since PV voltage should be constant and replacing (1.3) ( $v_{dc}(t) = V_{dc} + v_{ripple}(t)$ ) in (4.1), the compensator voltage will be derived as:

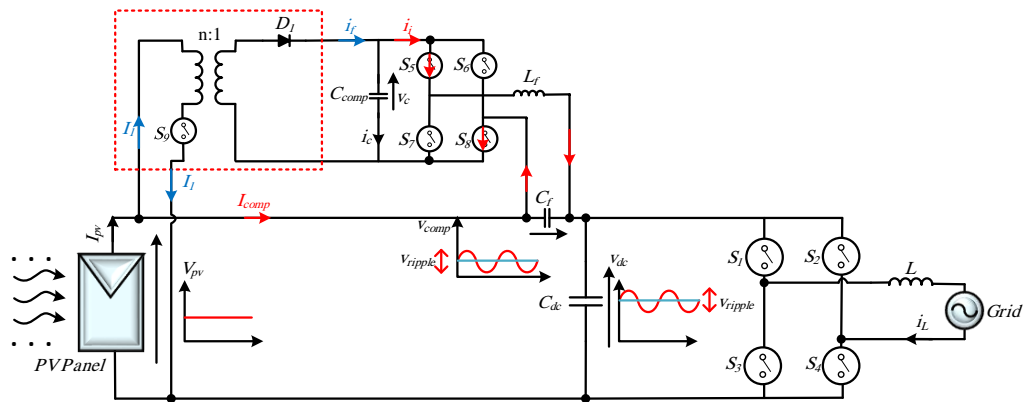
$$v_{comp}(t) = V_{dc} - V_{pv} + v_{ripple}(t) \quad (4.2)$$

The required  $v_{comp}(t)$  will be provided according to the system requirements.

The isolated DC/DC converter is a flyback converter because of the simplicity of design, control and limited number of components. The DC/AC converter is an H-bridge that can inject a voltage with both DC and AC components. The compensator has two operating modes illustrated in Figure 4.2; pulsating power compensation, and hybrid compensation under mismatch conditions.



a) Pulsating power decoupling mode



b) Hybrid compensator mode

**Figure 4.2.** Operating modes of the proposed hybrid compensator.

#### 4.1.1.1 Pulsating power compensation mode: $V_{dc} > \frac{V_o}{m_a}$

In this mode, the circuit only compensates the voltage ripple. Thus, the compensator voltage is calculated as follows:

$$v_{comp}(t) = v_{ripple}(t) \quad (4.3)$$

The total average power produced by the compensator is zero under the ideal conditions. The system configuration is shown in Figure 4.2a. Therefore, the voltage ripple will be eliminated on the PV panel side, and the PV voltage will become constant:

$$V_{PV} = V_{dc} \quad (4.4)$$

Thus, the maximum voltage ripple allowed on the DC bus can be increased and based on  $C_{dc} = \frac{P_o}{2\omega V_{dc} |\Delta v_{dc}|}$ , the DC-link capacitance will be reduced.

#### 4.1.1.2 Hybrid compensator (pulsating power and voltage drop compensator) under mismatching conditions: $V_{dc} < \frac{V_o}{m_a}$

In this mode, the compensator operates in hybrid mode as shown in Figure 4.2b because it compensates the voltage drop and attenuates the pulsating power, simultaneously. In this mode, the injected voltage consists of two terms:

DC component for drop voltage compensation ( $V_{comp} = V_{dc} - V_{pv}$ ), and AC component for pulsating power compensation ( $v_{ripple}(t)$ ):

$$v_{comp}(t) = V_{comp} + v_{ripple}(t) \quad (4.5)$$

In contrast to the previous mode, the hybrid compensator should inject active power fed from the PV panel, the only energy source. This is done with a low power flyback converter connected to the PV panel and the input of the compensator.

Thus, the required voltage to inject power to the grid is satisfied while eliminating the PV side's pulsating power. These two targets are achieved simultaneously without any additional power sources. The inverter is saved from shutting down without the need to limit the PV voltage. In addition, the flyback inverter has a low power rating.

## 4.2 Control System

The control of the hybrid compensator, which consists of three parts is shown in Figure 4.3: control of the main inverter, control of the H-bridge and control of the flyback converter.

For the main inverter, the MPPT defines the reference grid current, so that the reference current is the product of PLL output and the MPPT output. A simple Proportional-Resonant (PR) controller is adopted to regulate the grid current with fast dynamic response and zero steady state error (Figure 4.3a).

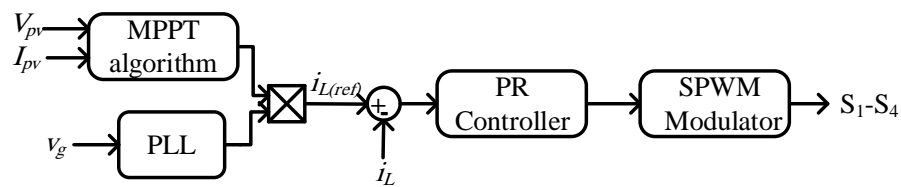
The transfer function of non-ideal (non-infinite gain) PR controller can be expressed as (4.6) [89],

$$G_{PR} = K_p + \frac{K_r s}{s^2 + 2\zeta\omega_0 s + \omega_0^2} \quad (4.6)$$

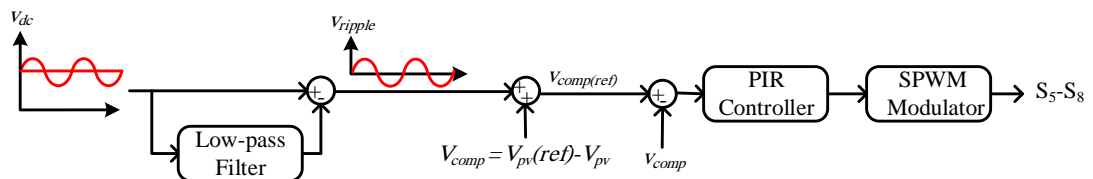
where  $K_p$  and  $K_r$  are the gains.  $\omega_0$  and  $\zeta\omega_0$  are the central angular frequency, and the bandwidth, respectively.

Because of slight changes in the frequency, a narrow bandwidth around the central frequency is usually adopted. However, the limited bandwidth leads to a high Q-factor, which is challenging to implement digitally. Therefore, a trade-off between bandwidth and digital implementation must be considered [89]. A Proportional-Integral-Resonant (PIR) controller is used to drive the H-bridge. It compensates the voltage ripple and the PV voltage drop (Figure 4.3b). The DC component is calculated from the difference between PV measured voltage ( $V_{pv}$ ) and PV voltage under normal condition ( $V_{pv(ref)}$ ). The integral part controls the steady state response, the voltage ripple is regulated by the resonant term (R) and finally the proportional term (P) is responsible for the dynamics.

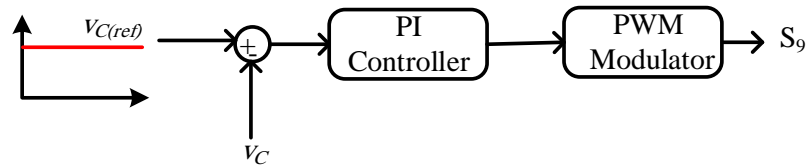
Due to the power flow balancing, the average voltage across the output capacitor of the flyback converter must be constant. Therefore, the switching signals of the flyback converter are provided by a PI controller (Figure 4.3c). By controlling the PV voltage with the MPPT and compensator, the DC bus voltage will be controlled for power injection over a wider operating range. In summary, the control of the proposed hybrid compensator is performed with usual PI, PIR and PR controllers.



a) Main inverter controller



b) Compensator H-bridge controller



c) Flyback controller

**Figure 4.3.** Block diagram of the controller of hybrid compensator.

### 4.3 The characteristics of the compensator

The power rating of the hybrid compensator depends on the voltage drop and voltage ripple. In other words, there is a tradeoff between the compensator power rating and the compensated voltage and ripples. Thus, under low irradiance condition with reduced DC-Link voltage, the apparent power ratio between the compensator and the whole system can be expressed as:

$$M = \frac{S_{comp}}{S_s} = \frac{|v_{comp}(t)I_{comp}|}{|v_{dc}(t)I_{comp}|} = \frac{|v_{comp}|}{|v_{dc}|} \quad (4.7)$$

Where  $S_{comp}$  is the compensator apparent power and  $S_s$  is the apparent power of system operating point. The compensator and DC-Link voltages can be expressed as:

$$v_{comp}(t) = V_{comp} + |\Delta v_{dc}| \cos 2\omega t \quad (4.8)$$

$$v_{dc}(t) = V_{dc} + |\Delta v_{dc}| \cos 2\omega t \quad (4.9)$$

Replacing (4.8) and (4.9) in (4.7), the power ratio becomes:

$$M = \frac{S_{comp}}{S_s} = \frac{|V_{comp} + |\Delta v_{dc}| \cos 2\omega t|}{|V_{dc} + |\Delta v_{dc}| \cos 2\omega t|} \quad (4.10)$$

Besides, considering  $k_v$  as a percentage of PV voltage drop, we have:

$$V_{comp} = k_v V_{PV(ref)} \quad (4.11)$$

Hence, substituting (4.11) in (4.10), the power ratio is:

$$M = \frac{|k_v V_{PV(ref)} + |\Delta v_{dc}| \cos 2\omega t|}{|V_{dc} + |\Delta v_{dc}| \cos 2\omega t|} \quad (4.12)$$

After compensation, the DC-Link voltage ( $V_{dc}$ ) will be equal to PV panel's voltage under normal condition ( $V_{PV(ref)}$ ). Therefore, (4.12) can be expressed as:

$$M = \frac{\left| k_v + \frac{|\Delta v_{dc}|}{V_{dc}} \cos 2\omega t \right|}{\left| 1 + \frac{|\Delta v_{dc}|}{V_{dc}} \cos 2\omega t \right|} \quad (4.13)$$

Since the RMS value of  $a_0 + a_1 \cos 2\omega t$  equals  $\sqrt{a_0^2 + \frac{a_1^2}{2}}$ , (4.13) can be simplified as:

$$M = \frac{\sqrt{k_v^2 + \frac{(|\Delta v_{dc}|/V_{dc})^2}{2}}}{\sqrt{1 + \frac{(|\Delta v_{dc}|/V_{dc})^2}{2}}} \quad (4.14)$$

The evolution of the power ratio versus  $|\Delta v_{dc}|/V_{dc}$  parameterized by  $k_v$  is shown in Figure 4.4.

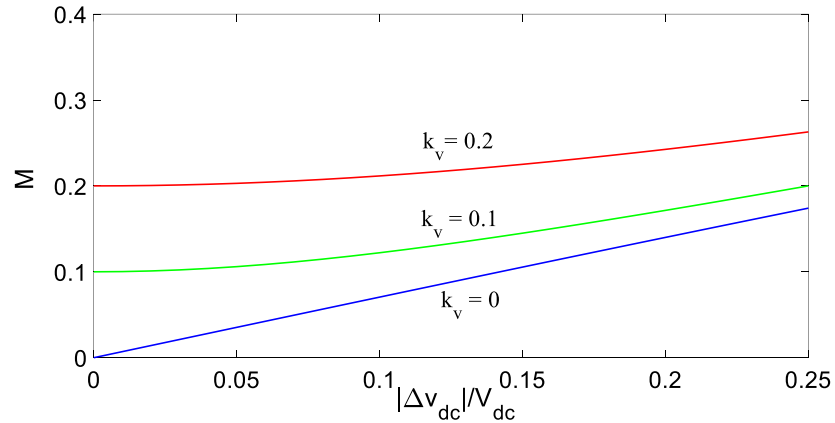


**Figure 4.4.** Power ratio.

It can be deduced from Figure 4.4 that in the worst-case corresponding to a voltage drop of 20% and a ripple of 20% of the DC bus voltage, the hybrid compensator should be sized at about 24% of the power of system operating point. But of course, the circuit will not be able to handle a large voltage reduction. However, the hybrid compensator can operate at a higher frequency than the main inverter, resulting in a higher power density. This is another advantage of the proposed hybrid compensator.

The sizing of the capacitor  $C_{comp}$  related to its current rating is another issue.

$$i_C(t) = i_f(t) - i_i(t) \quad (4.15)$$

where  $i_C(t)$ ,  $i_f(t)$  and  $i_i(t)$  are the input currents of the compensator DC-Link, the flyback output and the full-bridge, respectively. From Figure 4.2b, the following relationships can be deduced.

$$i_C(t) = C_{comp} \frac{dv_C(t)}{dt} \quad (4.16)$$

$$i_f(t) = \frac{P_{comp}}{v_C(t)} \quad (4.17)$$

$$i_i(t) = \frac{P_{comp}(t)}{v_C(t)} \quad (4.18)$$

Where  $v_C(t)$  and  $P_{comp}(t)$  are the voltage across  $C_{comp}$  and the instantaneous power of the compensator, respectively. They can be computed as:

$$v_C(t) = V_C + \Delta v_C(t) = V_C + |\Delta v_C| \cos(2\omega t) \quad (4.19)$$

$$P_{comp}(t) = v_{comp}(t) I_{comp} \quad (4.20)$$

By replacing (4.8) in (4.20),  $P_{comp}(t)$  can be derived as:

$$P_{comp}(t) = V_{comp} I_{comp} + |\Delta v_{dc}| I_{comp} \cos 2\omega t \quad (4.21)$$

Finally, the expressions of the currents can be obtained:

$$i_C(t) = -2\omega C_{comp} |\Delta v_c| \sin(2\omega t) \quad (4.22)$$

$$i_f(t) = \frac{V_{comp} I_{comp}}{V_C + |\Delta v_c| \cos(2\omega t)} \quad (4.23)$$

$$i_i(t) = \frac{V_{comp} I_{comp} + |\Delta v_{dc}| I_{comp} \cos 2\omega t}{V_C + |\Delta v_c| \cos(2\omega t)} \quad (4.24)$$

By substituting (4.22)- (4.24) in (4.15), and after some simplifications:

$$\begin{aligned} & \omega C_{comp} |\Delta v_c|^2 \sin(4\omega t) + 2\omega C_{comp} V_C |\Delta v_c| \sin(2\omega t) \\ & = |\Delta v_{dc}| I_{comp} \cos 2\omega t \end{aligned} \quad (4.25)$$

If the second-order term  $|\Delta v_c|^2$  is neglected, we can deduce:

$$C_{comp} = \frac{|\Delta v_{dc}| I_{comp}}{4\pi f |\Delta v_c| V_C} \quad (4.26)$$

In the worst case  $I_{comp} = I_{pv}$ , the expression of  $C_{comp}$  becomes:

$$C_{comp} = \frac{|\Delta v_{dc}| I_{PV}}{4\pi f |\Delta v_c| V_C} \quad (4.27)$$

## 4.4 Experimental bench and results of the dual-function power decoupling circuit

### 4.4.1 Design of the test bench components

The performance of the proposed system is evaluated on a test bench to show the validity of the hybrid compensator concept. A variable DC power source replaces the photovoltaic module and its MPPT algorithm with a series resistor. The experimental bench comprises a DC-Link capacitor, the compensator circuit (flyback and H-bridge converters), and the main inverter connected to the grid through an inductive filter. The power and voltage ratings are 1kW and 200V, respectively. The system is designed under the assumption of 20% voltage drop ( $k_v = 0.2$ ) and 20% permissible ripple on the DC-Link voltage ( $|\Delta v_{dc}| = 40$  V). So, from (4.14), the nominal power of the compensator is  $S_{comp} = MS_s = 0.24S_s$ . The study results in [4] have shown that for the most usual environmental conditions, the worst voltage reduction would be 15%. This voltage drop typically results in a 35 to 40% reduction in PV current based on PV panels characteristics. However, to have a compensator robust to unpredictable conditions, we have designed the compensator based on 20% reduction in PV current that

results in a higher power rating of the compensator:  $S_{comp} = 0.24 \times 160 \times 4 = 153VA$  , which is equal to 15% of system nominal power (1kW). Furthermore, to inject the ripple component, the flyback converter absorbs almost zero power and to inject DC power, it absorbs  $S_{comp} = 0.2 \times 160 \times 4 = 128VA$  .

According to (1.5) and (4.27), the evolutions of  $C_{dc}$  and  $C_{comp}$  versus  $\frac{|\Delta v_{dc}|}{V_{dc}}$  are depicted in Figure 4.5.

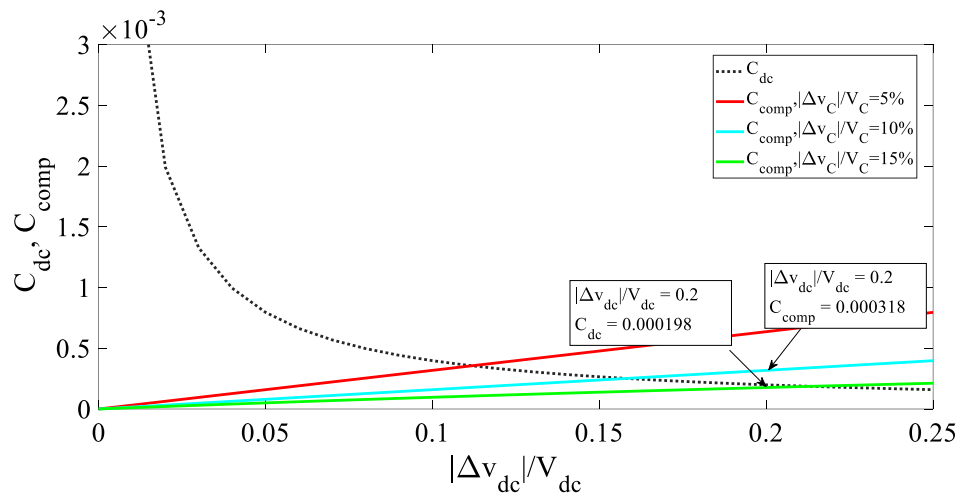


**Figure 4.5.** Evolution of the capacitors  $C_{dc}$  and  $C_{comp}$  .

With a voltage ripple of 20% on the DC bus, the values of the capacitors can be deduced :  $C_{dc} = 198 \mu F$ ,  $C_{comp} = 318 \mu F$  with  $V_C = 100 V$ . Finally, we have retained for  $C_{dc}$  a film capacitor of  $200\mu F$ ,  $400V$  with a lifetime of  $100000h$  at  $85^\circ C$ , and for  $C_{comp}$  two electrolytic capacitors in series, ( $680 \mu F$ ,  $63 V$ ) with a lifetime of  $8000h$  at  $125^\circ C$  .

The main inverter and the parameters of the proposed compensator are given in Table 4.1 and Table 4.2, respectively.

**Table 4.1.** Parameters of the main inverter in the PV system with hybrid compensator

Parameter	Description	Value
$V_g$	Grid voltage	110V (rms)
$f$	Grid frequency	50 Hz
$f_{sw}$	Switching frequency	6 kHz
$f_{sampling}$	Sampling frequency	12 kHz
$L$	Filter inductance	3.25 mH

**Table 4.2.** Parameters of the hybrid compensator.

Parameter	Description	Value
$f_{sw1}$	Switching frequency	40 kHz
$f_{sampling1}$	Sampling frequency	40 kHz
$L_f$	Filter inductance	0.5 mH
$C_f$	Filter capacitance	4 $\mu$ F

The digital control is implemented in a DSP-based board TMS320F28335. The LV25P and LTS25NP hall-effect transducers are used for voltage and current sensing. The experimental platform is shown in Figure 4.6.

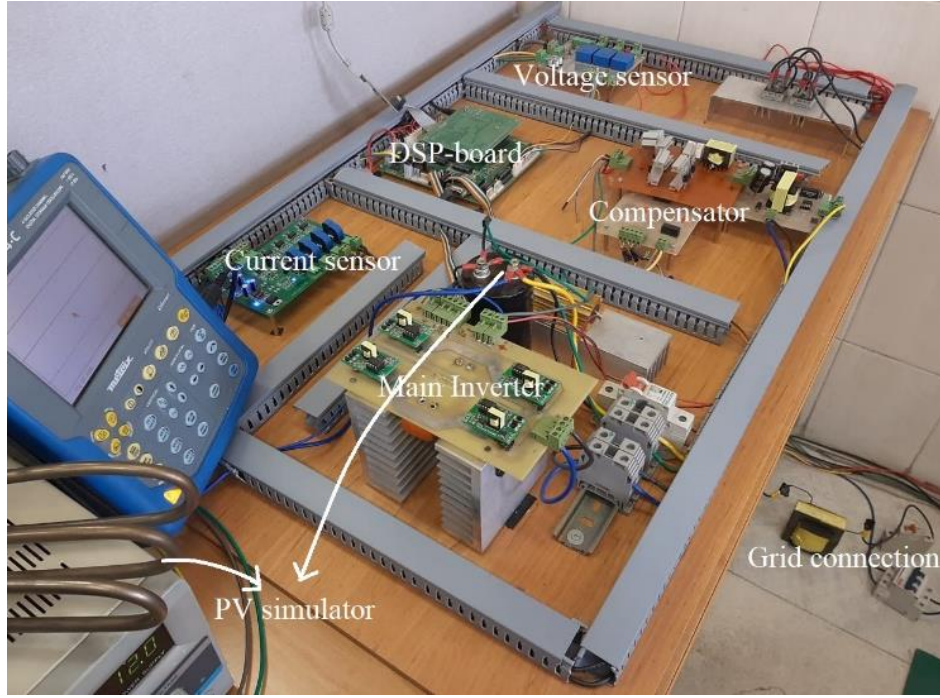


**Figure 4.6.** The experimental setup for hybrid compensator.

#### 4.4.2 Power losses and cost calculation

For better evaluation and fair comparison, the proposed system has been compared with the two-stage system proposed in [55] (Fig 2.11) using the same parameters in terms of efficiency and cost. The performance is based on series voltage compensation. The equations for the power losses are given as follows:

Conduction losses are calculated with the switch RMS current ( $I_{sw(mrs)}$ ), which flows through the equivalent  $R_{ds(on)}$  of the power switch. They are calculated as (4.28) for the main inverter and H-bridge compensator, and as (4.29) for the boost and flyback converters:

$$P_{cond} = 2I_{sw(mrs)}^2 R_{ds(on)} \quad (4.28)$$

$$P_{cond} = I_{sw(mrs)}^2 R_{ds(on)} + \underbrace{V_{fd} I_d}_{Diode} (avg) \quad (4.29)$$

The switching losses of the PWM switch are expressed as (4.30) for the main inverter and H-bridge compensator, and as (4.31) for the boost and flyback converters [90]:

$$P_{sw} = \frac{2V_{sw} (t_{on} + t_{off})}{2T_{sw}} I_{sw (rms)} \quad (4.30)$$

$$P_{sw} = \frac{V_{sw} (t_{on} + t_{off})}{2T_{sw}} I_{sw (rms)} \quad (4.31)$$

Where  $T_{sw}$  is the PWM switching period,  $t_{on}$  and  $t_{off}$  are the turn-on and turn-off times of the power switch.

Another significant factor is inductance losses that consist of the copper and core losses.

The copper losses can be calculated as:

$$P_{cu} = I_{L(rms)}^2 R_L \quad (4.32)$$

where  $R_L$  is the equivalent resistance of the inductor winding. The core losses are approximated by [90]:

$$P_{core} = k_f \Delta B^{2.33} f_{sw}^{1.32} V_{core} \quad (4.33)$$

Where  $V_{core}$  is the core volume and  $k_f$  is derived from the datasheet.

The costs are calculated from data found on the international market. The power losses and costs are displayed in Tables 4.3 and 4.4. The results show that the proposed hybrid compensator has a lower cost and a higher efficiency. In addition, compared to usual single-stage inverter, it has the advantage of voltage boosting capability.

To have a better evaluation of the proposed circuit, the efficiency is displayed for two operating conditions:

- Under normal irradiance conditions (1kW), the flyback power is almost zero, and the H-bridge only compensates the pulsating power leading to an efficiency of 96.8%.
- Under low irradiance conditions (0.64 kW) for which we have considered a severe voltage reduction of 40V, both converters consume energy and the efficiency drops to 96.6%.

The efficiency drops of 0.2%, which is much less than the power loss of conventional boost converter that is about 2- 3%. Therefore, the impact on the efficiency is minor.

**Table 4.3.** Power losses and cost calculation of the system proposed in [55]

		Main Inverter	Boost converter	Compensator H-bridge
Power		1kW	1kW	140W
Switches, diodes		S1-S4 (200v, 12.85A), FCH25N60N	S9(200V,12A), FCH25N60N D1(200V,12A), D4020L	S5- S8(50V,5A) FDPF3860T
Passive elements		L(3.25mH,12.85A), EE85, C <sub>dc</sub> (200μF,200V), Film capacitor	C <sub>p</sub> (100uF,100V) , L <sub>1</sub> (2mH,12A), EE85	C <sub>comp</sub> (1273μF,50V), Electrolytic capacitor C <sub>f</sub> (4.7μF,40V), film capacitor L <sub>f</sub> (0.5mH,5A), pq32/20
Power losses, efficiency at 1kW	$P_{cond} + P_{sw}$	8.93+0.21 =9.14W	5.44+6+0.12 =11.56W	1.52+0.21 =1.73W
	$P_{cu} + P_{core}$	13.34+0.19 =13.53W	11+0.64 =11.64W	2.35+0.14 =2.49W
	losses	22.67W	23.2W	4.22W
	Drive, additional auxiliary	5W		
	Total losses Efficiency	55.09W 94.5%		
Cost		75\$	40\$	26\$
		141\$		

**Table 4.4.** Power losses, efficiency and costs for the proposed circuit.

		Main Inverter	Flyback converter	Compensator H-bridge
Power		1kW	128W	153W
Switches and diodes		S1-S4(200v,12.85A), FCH25N60N	S9(300V,4.93A), FCH25N60N D1(300V,4.93A), D4020L	S5-S8(100V,5A) FDP2670
Passive elements		L(3.25mH,12.85A), EE85, C <sub>dc</sub> (200μF,200V), Film	T1(1:1) (L <sub>T1</sub> (0.3mH,4.93)), EE30	C <sub>comp</sub> (318μF,100V), Electrolytic C <sub>f</sub> (4.7μF,80V), film L <sub>f</sub> (0.5mH,5A), pq32/20
Power losses, efficiency at 1kW	$P_{cond} + P_{sw}$	8.93+0.21=9.14W	-	1.96+0.35 =2.31W
	$P_{cu} + P_{core}$	13.34+0.19 =13.53W	-	2.35+0.14 =2.49W
	Total	22.67W	-	4.8W
	Drive,...	5W		
	Losses Efficiency	32.47W 96.8%		
Power losses, efficiency at 0.64kW	$P_{cond} + P_{sw}$	3.67+0.13=3.8W	0.32+0.28+1.05 =1.65W	1.6+0.32 =1.92W
	$P_{cu} + P_{core}$	5.36+0.19=5.55W	2.66+0.34=3W	0.96+0.05 =1.01W
	Total	9.35W	4.65W	2.93W
	Drive,...	5W		
	Losses Efficiency	21.93W 96.6%		
Cost		75\$	11\$	28\$
		114\$		

To better illustrate the comparison, the loss breakdown is displayed in Figure 4.7.

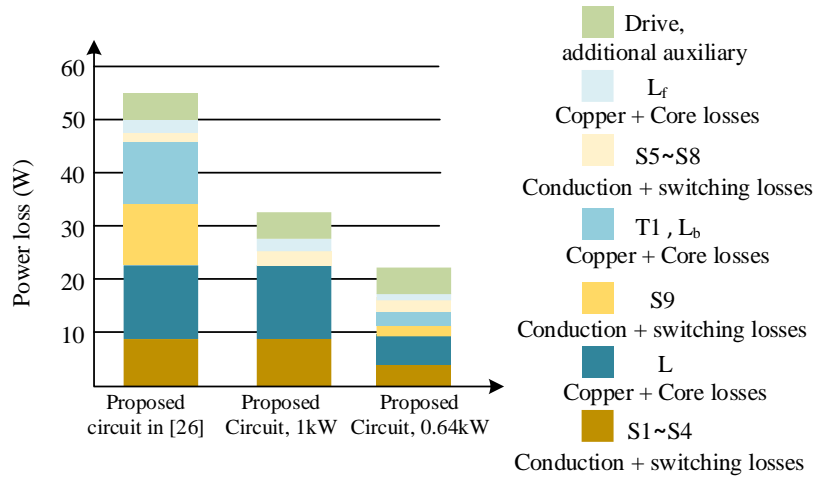


**Figure 4.7.** Power loss breakdown analysis.

#### 4.4.3 Experimental results under rated irradiation

The first experiment evaluates the performance of the system under normal irradiation conditions. The grid voltage, PV voltage, DC-Link and compensator voltages are shown in Figure 4.8. The average inverter DC voltage is equal to 200V, and the voltage ripple at twice the mains frequency have a peak-to-peak value of 82V. As it can be observed, the compensator perfectly tracks the ripples in the voltage. Consequently, the peak-to-peak voltage oscillations on the PV side reach 12.5V, which corresponds to a significant reduction of 85% compared

to the ripples on the DC bus voltage. Thus, as expected, the PV voltage is smoother, and the pulsating power is effectively attenuated on the PV panel side. The PV and grid currents, and the DC voltage of the compensator are shown in Figure 4.9. To ensure unity power factor, a high precision fast response phase-locked-loop (PLL) has been used [91]. The PV current is 5A and the maximum value of the grid current is 12.41A. Then  $P_o = 965 \text{ W}$  with an efficiency of 96.5% at nominal power. The compensator DC bus voltage illustrates the absorption and compensation of the pulsating power.

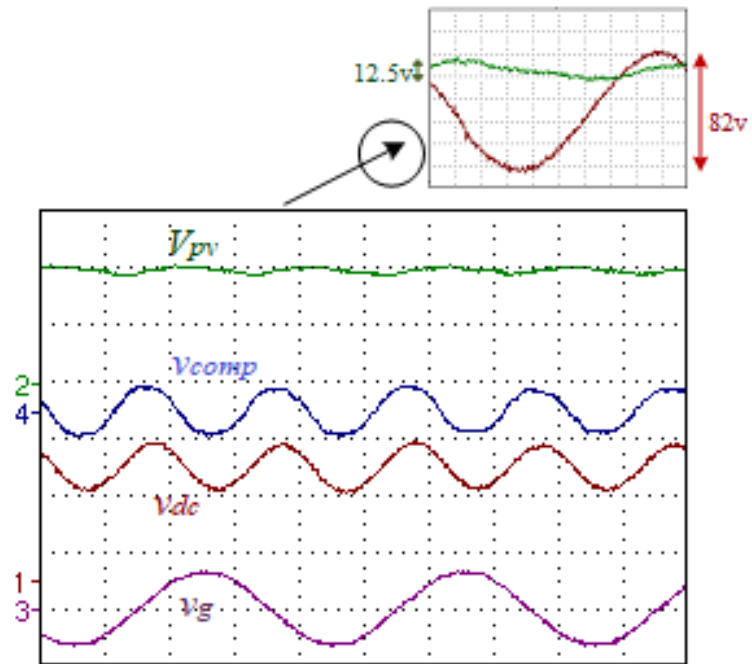


**Figure 4.8.** Experimental results of the proposed compensator under rated irradiation; time: (5ms/div),  $v_{dc}$  (100 V/div),  $V_{pv}$  (100 V/div),  $v_g$  (250V/div), and  $v_{comp}$  (100V/div).

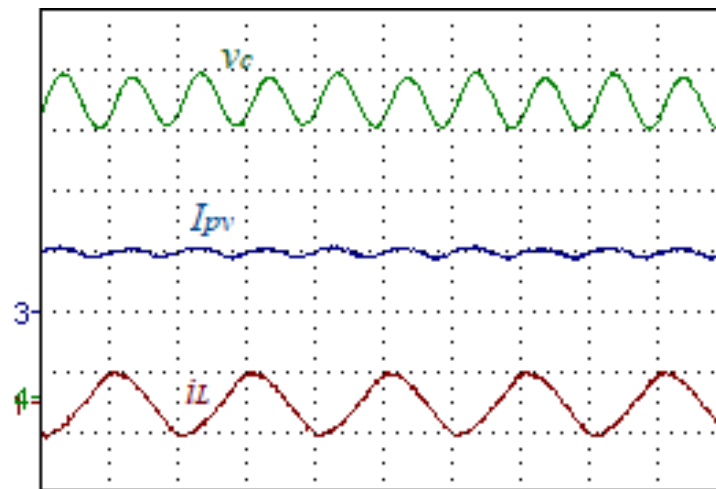


**Figure 4.9.** Experimental results of the proposed compensator under rated irradiation; time: (10ms/div),  $i_L$  (25 A/div),  $I_{pv}$  (5 A/div), and  $v_c$  (20 V/div).

#### 4.4.4 Experimental results under low irradiation

The second experiment evaluates the compensator's performance under low irradiance conditions due, for example, to clouds. The PV emulator voltage is reduced by 20% to 160 V to emulate the corresponding voltage drop. Therefore, the proposed system should compensate for a voltage drop of 40V DC and a peak-to-peak voltage ripple of 50V. The grid voltage, PV voltage, DC-Link and compensator voltages are shown in Figure 4.10. According to these results, the hybrid compensator increases the DC voltage to 200V on the inverter side to maintain power injection and effectively compensates for voltage ripple. Thus, the two aims of the proposed hybrid compensator are performed flawlessly, which validate the dual-function decoupling circuit.

The PV and grid currents and the compensator DC-Link voltage displayed in Figure 4.11 show the system injects power into the grid despite the PV voltage drop. The proposed hybrid compensator is the only one among the decoupling circuits to perform this function.

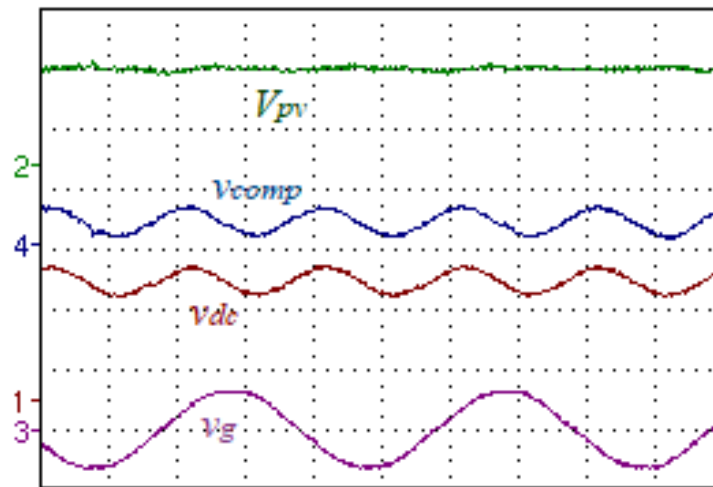


**Figure 4.10.** Experimental results of the proposed compensator under conditions of low irradiation; time: (5ms/div),  $v_{dc}$  (100 V/div),  $V_{pv}$  (100 V/div),  $v_g$  (250V/div), and  $v_{comp}$  (100V/div).

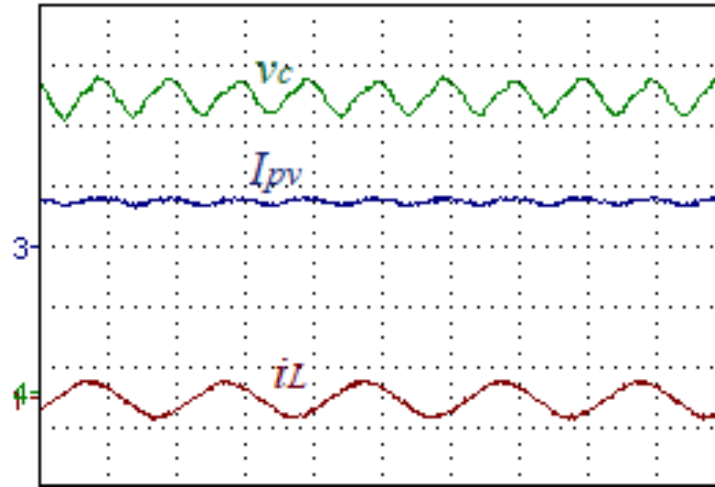


**Figure 4.11.** Experimental results of the proposed compensator under conditions of low irradiation; time: (10 ms/div),  $i_L$  (25 A/div),  $I_{pv}$  (5 A/div), and  $v_c$  (20 V/div).

#### 4.4.5 Experimental results in transient operation

The PV voltage steps down from 200V to 160V to evaluate the dynamics of the proposed hybrid compensator. The output power decreases from 1000 to 640W, and the voltage ripple decreases from 82V to 50V. The results are shown in Figure 4.12. The compensator tracks the voltage variations with a time response lower than 20ms, which is acceptable regarding the dynamics of the PV panels. It is worth to be mentioned that the PV dynamics are absolutely lower than step change as tested in Figure 4.12. Hence, this experiment is conducted under the worst case. The results confirmed that the real system can track the changes with higher dynamic response.

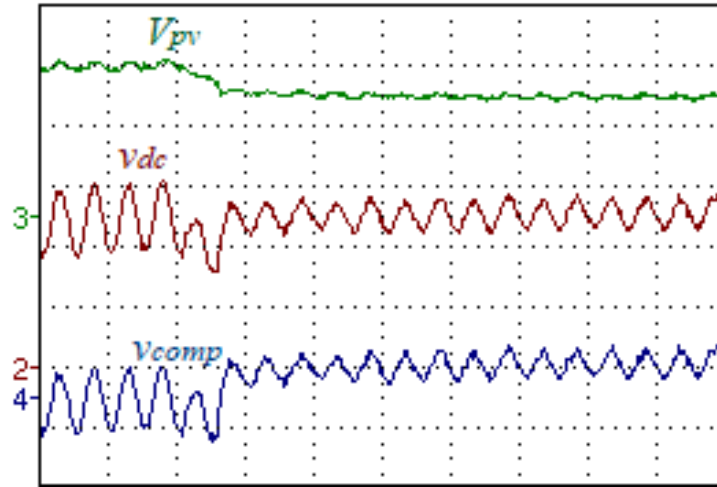


**Figure 4.12.** Transient responses of the proposed compensator; time: (20ms/div),  $v_{dc}$  (80 V/div),  $V_{pv}$  (80V/div), and  $v_{comp}$  (80V/div).

#### 4.4.6 Experimental results under condition of non-unity power factor

The last experiment is conducted with a leading power factor of 0.9. The DC-Link voltage, PV voltage, grid current and voltage are plotted in Figure 4.13. The results show the ability to exchange reactive power.

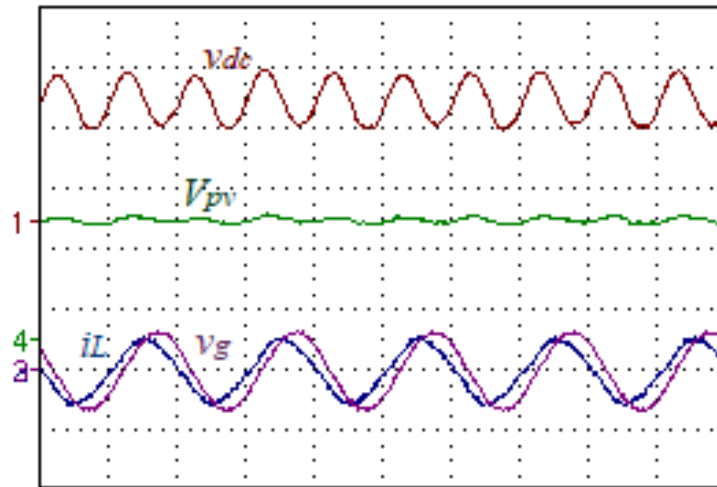


**Figure 4.13.** Experimental results of the proposed compensator with 0.9 leading power factor; time: (10ms/div),  $v_{dc}$  (100 V/div),  $V_{pv}$  (100 V/div),  $v_g$  (250V/div), and  $i_L$  (25A/div).

#### **4.4.7 Comparison of decoupling circuits**

Different active power decoupling circuits have been compared in Table 4.5 based on various criteria. As it can be observed, the proposed system achieves a significant reduction of voltage ripple using a straightforward control method. The most significant reduction of voltage ripple is achieved in [41] at the expense of using a complex controller. The reduction is only 80% with a PI controller. Another parameter is the number of components. As expected, in single-stage systems, the number of components is lower. However, they do not have voltage boosting capability.

Consequently, the voltage operating range in PV applications must be limited, reducing efficiency by up to 4% [4]. On the other hand, two-stage systems require an additional stage at nominal power, which results in higher cost and reduced efficiency. The proposed system has the minimum number of components at nominal power and the components of the compensator are rated at 15% of the nominal power. It operates as a conventional single-stage system under normal irradiance conditions. Besides, under conditions of low irradiance, the limited operating voltage range is mitigated thanks to the additional low power DC/DC converter. In other words, the proposed system combines the advantages of single and two-stage systems.

**Table 4.5.** Comparison of decoupling circuits with proposed hybrid compensator.

Ref	Proposed system	[51]	[47]	[92]	[93]	[94]	[49]	[55]	[41]	[52]	
Single/Two stage inverter	single	single					two				
Inverter nominal Power	1kW	1kW	110W	2.1kW	600W	2kW	250W	2kW	500W	400W	
Grid voltage	110V	230V	220V	220V	110V	220V	100V	220V	120	156V	
DC-link voltage	200V	400V	34V	422V	250V	400V	265V	400V	N.A	200V	
DC-link capacitor	200 $\mu$ F	110 $\mu$ F	N.A	-	330 $\mu$ F	135 $\mu$ F	100 $\mu$ F	220 $\mu$ F	N.A	-	
(Compensator power/nominal power)	15%	100%	N.A	100%	100%	100%	100%	14%	100%	100%	
Voltage boosting capability	Yes	No	No	No	No	No	Yes	Yes	Yes	Yes	
Switches, Diodes	4 5,1 (15% nominal power)	6	6	6,4	6	6	7,1	5,1 4 (14% nominal power)	9,1	6	
Capacitors, inductors	1,1 2,2 (15% nominal power)	2,2	4,2	2,4	2,2	2,2	3,3	2,3 1,2(14% nominal power)	2,3	2,2	
Compensator capacitor	318 $\mu$ F, 100V	165 $\mu$ F, 252-706V	500 $\mu$ F, 45V	2 $\times$ 150 $\mu$ F, 422V	-	130 $\mu$ F, 220V	220 $\mu$ F, 300V	1273 $\mu$ F, 63V	N.A	160 $\mu$ F, 120V	
Voltage Ripple Reduction %	85%	76%-88%	82%	83%	84%	N.A	80%	84%	90%	75%	
Efficiency	96.5%	N.A	N.A	96.3%	78%	97%	88%	N.A	N.A	91%	
Control and modulation System Complexity	low	low	high	low	high	high	high	low	high	high	

## 4.5 Conclusion

In this chapter, a dual-objective compensation circuit is proposed for single-stage grid-connected PV inverters. This circuit can simultaneously compensate for pulsating power and mitigate limited operation range due to voltage drop under low irradiance conditions. These objectives are fulfilled thanks to additional power converters; a low power flyback and an H-

bridge. The voltage drop compensation increases the operating range of the inverter, prevents its shutdown, and increases the system reliability. The control structure is based on the conventional PI and PR controllers. A 1kW test bench has been designed to evaluate the proposal for several operating points. The steady-state results show that the hybrid compensator can simultaneously achieve 85% compensation of the pulsating power and 20% compensation of the voltage drop. The circuit also shows good transient responses. The experimental results also prove the ability of the circuit to handle the reactive power flow. A comparison with a double-stage inverter has shown the superiority of the proposal in terms of efficiency and cost.

**Chapter 5 Proposed dual- function Impedance spectroscopy  
tool and pulsating power compensator**

## 5.1 Impedance spectroscopy tool and pulsating power compensator

The general structure of the PV system is depicted in Figure 5.1. It consists of PV panels, DC-link, grid connection, the main inverter, and a low power inverter used for pulsating power decoupling, and impedance spectroscopy. The low power inverter is a full bridge placed between PV panels and the main inverter with series connection.

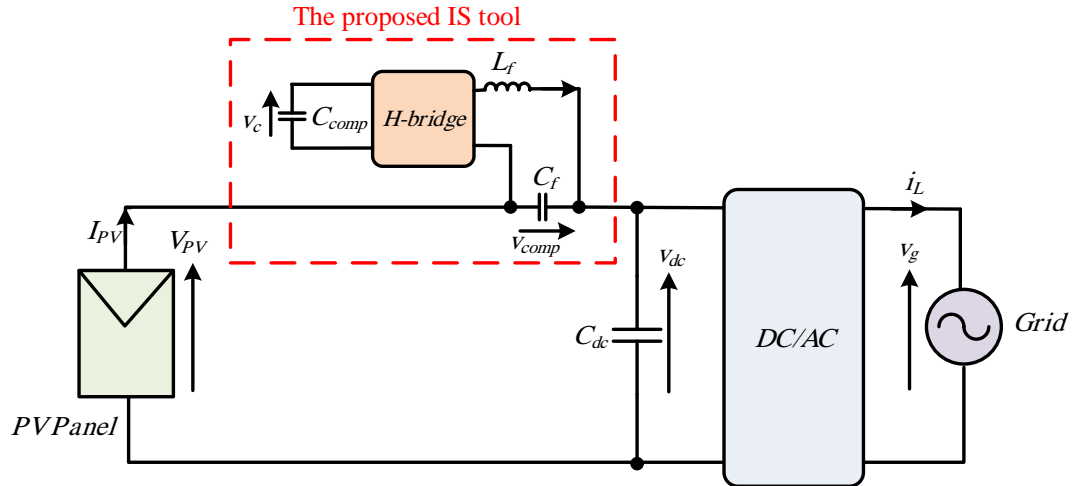


**Figure 5.1.** General structure of the PV system with proposed circuit as pulsating power decoupling and IS circuit.

### 5.1.1 Equivalent electric circuit of a PV module

The static equivalent circuit of the PV module is depicted in Figure 5.2 [95]. In this non-linear model, the diode is assumed as an ideal component and so, there is no frequency dependence.

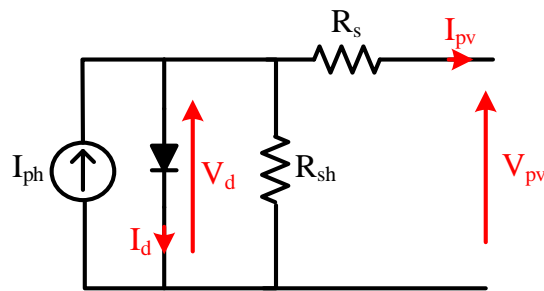


**Figure 5.1.** The static (DC) equivalent circuit of a PV module [95].

The PV current can be calculated as [96]:

$$I_{pv} = I_{ph} - \underbrace{I_s(T) \left( e^{\frac{V_d}{\eta V_T}} - 1 \right)}_{I_d(T, V_d)} - \frac{V_{pv} + R_s I_{pv}}{R_{sh}} \quad (5.1)$$

Where  $V_{pv}$ ,  $I_{pv}$  are PV voltage and current, respectively.  $I_{ph}$  and  $I_s$  are the photovoltaic and saturation currents, respectively.  $R_{sh}$  and  $R_s$  are shunt and series equivalent resistances, respectively. Furthermore,  $\eta$  is the diode ideality factor and  $V_T(T_{pn}) = \frac{k_b T_{pn}}{q} N_s$  is the thermal voltage.  $T_{pn}$  is the temperature of the p-n junction.  $N_s$  is the number of cells in series,  $q$  is the charge of the electron, and  $k_b$  is Boltzmann constant.

However, when the PV panels are connected to switch mode power converters, a dynamic model must be considered. In the dynamic model shown in Figure 5.3, the diode is replaced by two capacitors  $C_t$  and  $C_d$ , and one resistance  $R_d$  [97].

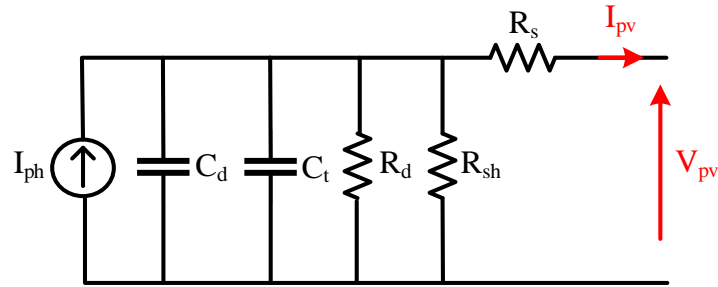


**Figure 5.2.** The dynamic equivalent circuit of a PV module.

$C_t$  is the transient or junction capacitor due to the charge stored in the region of depletion at the p-n junction of semiconductor.  $C_d$  represents the diffusion capacitance, which is due to the charge stored outside the region of depletion in the semiconductor neutral region. These capacitors have non-linear behaviors. Their values depend on the operating point and temperature [97]. They can be calculated using (5.2) and (5.3) [97]:

$$C_t(V_d) = \frac{C_{t0}}{\sqrt{1 - \frac{V_d}{N_s \phi_0}}} \quad (5.2)$$

$$C_d(T_{pn}, V_d) = \frac{\tau I_d(T_{pn}, V_d)}{\eta \mathcal{N}_T(T_{pn})} \quad (5.3)$$

Where  $C_{t0}$  is zero-voltage capacitance,  $\phi_0$  is the zero-voltage junction potential and  $\tau$  is mean carrier lifetime [104].

The shunt dynamic resistance of the diode is expressed as:

$$R_d = \frac{dV_d}{dI_d} = \frac{\eta \mathcal{N}_T(T_{pn})}{I_s(T_{pn})} e^{-\frac{V_d}{\eta \mathcal{N}_T(T_{pn})}} \quad (5.4)$$

## 5.1.2 System operation description

### 5.1.2.1 Pulsating power decoupling

The proposed converter is a full-bridge inverter with series connection, which injects an AC voltage for mitigation of the voltage ripples on the DC side, and estimation of PV panel impedance. The total average power produced by the compensator is zero. Therefore, by using a floating capacitor at the input of the proposed converter, the required voltage can be generated. The system configuration is shown in Figure 5.4.

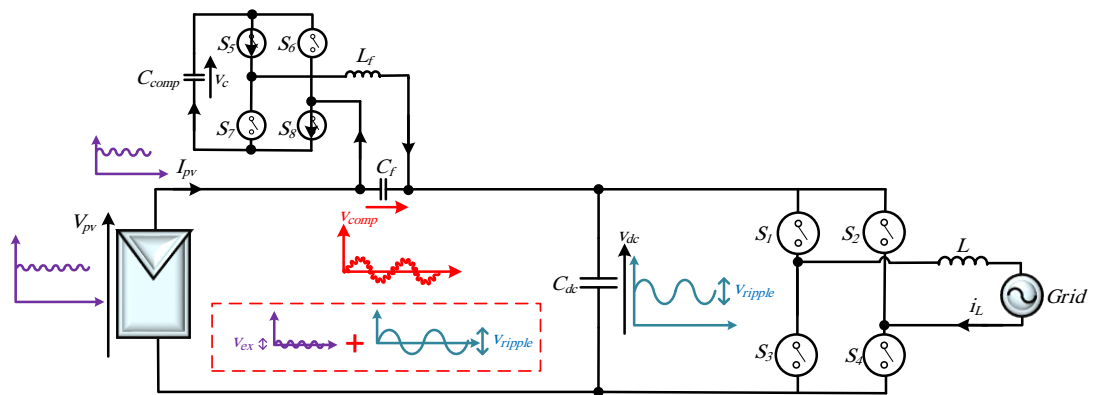


**Figure 5.3.** Circuit configuration of the PV system with proposed circuit as pulsating power compensator and IS circuit.

The principle for the pulsating power decoupling is the same as in chapter 4: the compensator generates a voltage ripple to offset the DC-link voltage ( $v_{ripple}(t) = |\Delta v_{dc}| \cos 2\omega t$ ). The impedance spectroscopy consists of injecting an additional excitation sinusoidal voltage with a variable frequency into the compensator. Once the corresponding current is extracted from the PV current measurements, using the excitation voltage, the PV panel impedance can be calculated.

As shown in Figure 5.4, the injected voltage using the converter is assumed as follows:

$$v_{comp}(t) = v_{ripple}(t) - v_{ex}(t) \quad (5.5)$$

Where  $v_{ripple}(t)$  is used for active power decoupling, and  $v_{ex}(t)$  is used as excitation voltage for PV impedance measurement. By applying KVL on the PV side, the PV voltage can be expressed as:

$$V_{pv} = v_{dc}(t) - v_{comp}(t) \quad (5.6)$$

By replacing  $v_{dc}(t) = V_{dc} + v_{ripple}(t)$  in (5.6), PV voltage is derived as:

$$V_{pv} = V_{dc} + v_{ripple}(t) - v_{comp}(t) \quad (5.7)$$

Finally, replacing (5.5) in (5.7), we have:

$$V_{pv} = V_{dc} + v_{ex}(t) \quad (5.8)$$

As a result, the voltage ripple ( $v_{ripple}(t)$ ) is eliminated on the PV panel side.

### 5.1.2.2 Impedance Spectroscopy

According to (5.8), there is an additional component in the PV voltage. This component ( $v_{ex}(t)$ ) is a low amplitude excitation voltage expressed as:

$$v_{ex}(t) = V_{ex} \cos(\omega_{ex} t) \quad (5.9)$$

Where  $V_{ex}$  is the amplitude of excitation voltage, and  $\omega_{ex}$  is the signal frequency. This excitation voltage will generate a sinusoidal component in the PV current as:

$$i_{ex}(t) = I_{ex} \cos(\omega_{ex} t + \varphi) \quad (5.10)$$

Where  $I_{ex}$  and  $\varphi$  depend on the impedance of the PV panel that can be expressed as:

$$Z(\omega_{ex}) = \frac{V_{ex}}{I_{ex}} \angle \varphi \quad (5.11)$$

Therefore, by extracting the amplitude and the phase of voltage and current excitation signals using Fast Fourier Transform (FFT), the impedance of the PV panel at frequency  $\omega_{ex}$  can be calculated.

The equivalent circuit of PV panels with impedance measurement is depicted in Figure 5.5.

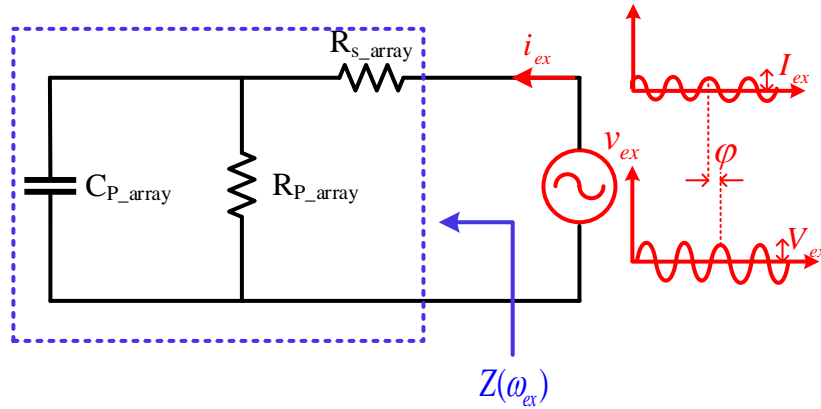


**Figure 5.4.** The PV panel equivalent circuit with impedance measurement.

The circuit can be simplified as displayed in Figure 5.6.

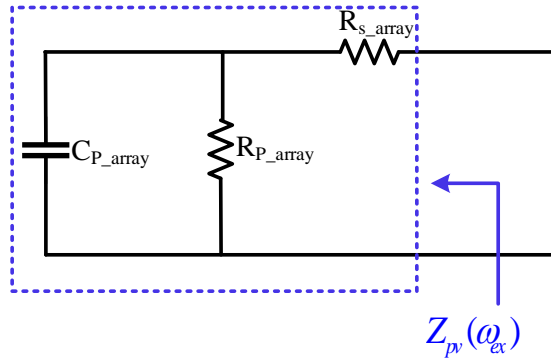


**Figure 5.5.** The simplified PV panels equivalent circuit.

Hence, the impedance can be expressed as:

$$Z(\omega_{ex}) = R_{s\_array} + \frac{R_{p\_array}}{1 + (R_{p\_array} C_{p\_array} \omega_{ex})^2} - j \frac{R_{p\_array}^2 C_{p\_array} \omega_{ex}}{1 + (R_{p\_array} C_{p\_array} \omega_{ex})^2} \quad (5.12)$$

The Nyquist diagram is shown in Figure 5.7. It is a semi-circle located at  $R_{s\_array}$  from the imaginary axis with a diameter  $R_{p\_array}$ . At the cutoff frequency  $f_c = \frac{1}{2\pi R_{p\_array} C_{p\_array}}$ ,

the real part of the impedance is equal to  $R_{s\_array} + \frac{R_{p\_array}}{2}$ . At the minimum frequency ( $\omega_{ex} = 0$ ), the impedance is equal to  $R_{s\_array} + R_{p\_array}$ , while at the maximum frequency it is equal to  $R_{s\_array}$ .

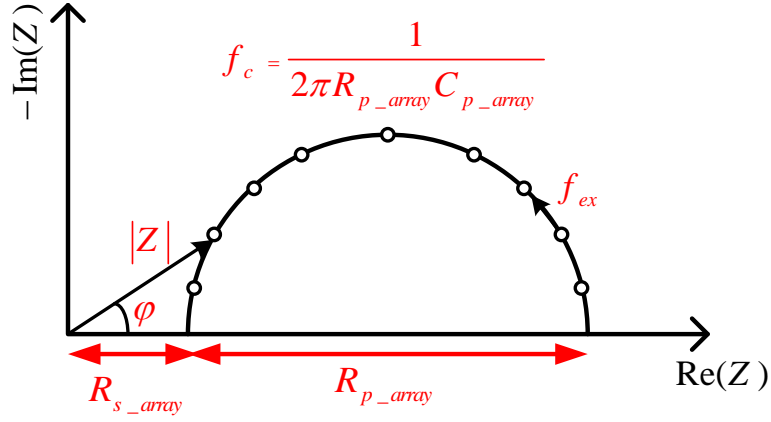


**Figure 5.6.** Nyquist diagram of the PV panel.

There are two parameters to set to operate the impedance spectroscopy; the frequency and the amplitude of the excitation voltage. The frequency range will be selected based on the frequency analysis of the theoretical impedance. To set the voltage amplitude, let us analyze the effect of the excitation on the PV power. If we consider slight variations around the MPPT, the power of the PV panels can be expressed as:

$$P(t) = (V_{mpp} + V_{ac} \cos(2\omega t) + V_{ex} \cos(\omega_{ex} t)) \times (I_{mpp} + I_{ac} \cos(2\omega t - \theta) + I_{ex} \cos(\omega_{ex} t + \varphi)) \quad (5.13)$$

Where  $V_{ac} \cos(2\omega t)$ ,  $I_{ac} \cos(2\omega t - \theta)$  are arising from pulsating power. The magnitude of these terms depends on the DC-Link capacitor, and the efficiency of the decoupling method. After simplification, and if the second-order terms are neglected, we can evaluate the variation of the power as:

$$\underbrace{P(t) - V_{ac} I_{mpp} \cos(2\omega t) - I_{ac} V_{mpp} \cos(2\omega t - \theta) - V_{mpp} I_{mpp}}_{P_{pv}(t)} = V_{ex} I_{mpp} \cos(\omega_{ex} t) + I_{ex} V_{mpp} \cos(\omega_{ex} t + \varphi) \quad (5.14)$$

Equation (5.14) can be expressed as:

$$\frac{P_{pv}(t) - V_{mpp} I_{mpp}}{V_{mpp} I_{mpp}} = \frac{V_{ex}}{V_{mpp}} \cos(\omega_{ex} t) + \frac{I_{ex}}{I_{mpp}} \cos(\omega_{ex} t + \varphi) \quad (5.15)$$

Assuming  $\varepsilon = P_{pv}(t) - V_{mpp} I_{mpp}$ , which is the power oscillation arising from the excitation voltage, we have:

$$\left| \frac{\varepsilon}{V_{mpp} I_{mpp}} \right| < \frac{V_{ex}}{V_{mpp}} + \frac{I_{ex}}{I_{mpp}} = \gamma \quad (5.16)$$

$\gamma$  is defined as the relative power oscillation amplitude due to the excitation voltage.

Replacing  $|Z| = \frac{V_{ex}}{I_{ex}}$  and after some simplifications,  $V_{ex}$  is derived as:

$$V_{ex} = \frac{\gamma}{\frac{1}{V_{mpp}} + \frac{1}{|Z| I_{mpp}}} \quad (5.17)$$

Considering  $Z_{mpp} = \frac{V_{mpp}}{I_{mpp}}$ , (5.17) is computed as:

$$V_{ex} = \gamma \mathcal{W}_{mpp} \frac{1}{1 + \frac{Z_{mpp}}{|Z|}} \quad (5.18)$$

From this equation, we can observe that:

- if the permissible amplitude of pulsation power is fixed, the amplitude of the excitation signal can be chosen for each frequency,
- if the excitation voltage is chosen to be constant, the relative amplitude will be variable during impedance spectroscopy.

To sum up, with the injection of an excitation signal, we can realize impedance spectroscopy without using any additional circuit. The proposed circuit realizes active pulsating power compensation, and impedance spectroscopy, simultaneously. This method can be used as an online IS method as it does not require interrupting PV panels operation. Besides, it works independently from the main inverter, which makes the control and system design flexible.

### 5.1.3 The characteristics of the compensator

Since the amplitude of the excitation voltage is much less than the voltage ripple, it was neglected in the power rating of the compensator. Thus, same as in chapter 4, the DC-link capacitor ( $C_{dc}$ ) is calculated as  $C_{dc} = \frac{P_o}{2\omega V_{dc} |\Delta v_{dc}|}$ .

The apparent power ratio between the compensator, and the whole system can be expressed as:

$$M_1 = \frac{S_{comp}}{S} = \left| \frac{v_{ripple}(t) I_{pv}}{v_{dc}(t) I_{pv}} \right| = \left| \frac{v_{ripple}}{v_{dc}} \right| \quad (5.19)$$

Where  $S_{comp}$ , and  $S$  are the compensator and system apparent powers, respectively.

Therefore, replacing  $v_{ripple}(t) = |\Delta V_{dc}| \cos 2\omega t$  in (5.19), it can be expressed as:

$$M_1 = \frac{S_{comp}}{S} = \frac{|\Delta v_{dc}|}{\sqrt{2} V_{dc}} \quad (5.20)$$

Since  $|\Delta v_{dc}| \ll \sqrt{2} V_{dc}$ , it confirms that the compensator power is much less than the system power.

A design issue is the sizing of the compensator input capacitor. The energy released from  $C_{comp}$  with its voltage changes from  $V_c + |\Delta v_c|$  to  $V_c - |\Delta v_c|$  can be expressed as follows:

$$\Delta E = \frac{1}{2} C_{comp} (V_c + |\Delta v_c|)^2 - (V_c - |\Delta v_c|)^2 = 2C_{comp} V_c |\Delta v_c| \quad (5.21)$$

Where  $|\Delta v_c|$  and  $V_c$  are the amplitudes of voltage ripple and average voltage across the compensator input capacitor ( $C_{comp}$ ), respectively. On the other hand, the delivered energy to the system through the proposed circuit can be calculated as follows:

$$W = \int_{-\frac{T}{8}}^{\frac{T}{8}} I_{PV} v_{ripple}(t) dt \quad (5.22)$$

By replacing  $v_{ripple}(t) = |\Delta V_{dc}| \cos 2\omega t$ , (5.22) can be expressed as follows:

$$W = I_{pv} \int_{-\frac{T}{8}}^{\frac{T}{8}} |\Delta v_{dc}| \cos(2\omega t) dt = \frac{I_{pv} |\Delta v_{dc}|}{\omega} \quad (5.23)$$

Based on the rule of energy balance, the delivered energy to the system through the proposed circuit is equal to the energy released from the capacitor  $C_{comp}$  during the same period. As a result, we have:

$$\Delta E = W \quad (5.24)$$

Replacing (5.21) and (5.23) in (5.24) and after some simplifications,  $C_{comp}$  can be calculated as:

$$C_{comp} = \frac{I_{pv} |\Delta v_{dc}|}{2\omega V_c |\Delta v_c|} \quad (5.25)$$

#### 5.1.4 Control system

To operate the system, the controller must realize three functions: 1) mitigate the voltage ripple, 2) manage excitation voltage, 3) regulate the voltage across the capacitance  $C_{comp}$ .

The voltage ripple is regulated using a proportional-resonant controller to track the sinusoidal reference. The proportional term sets the dynamic response while the resonant one regulates the voltage ripple. The transfer function of non-ideal PR controller can be expressed as (4.6).

On the other hand, a PI controller is used to charge the input capacitance of the compensator and regulate its voltage at the reference value ( $V_{C(ref)}$ ).

The excitation voltage at different frequencies is added to the PR controller output to determine the reference signal of the PWM modulator. The larger is the amplitude of the injected voltage, and the better will be the impedance resolution. However, it may affect the PV panel performance, and thus, there is a tradeoff for setting the magnitude. The block diagram of the proposed controller is shown in Figure 5.8.

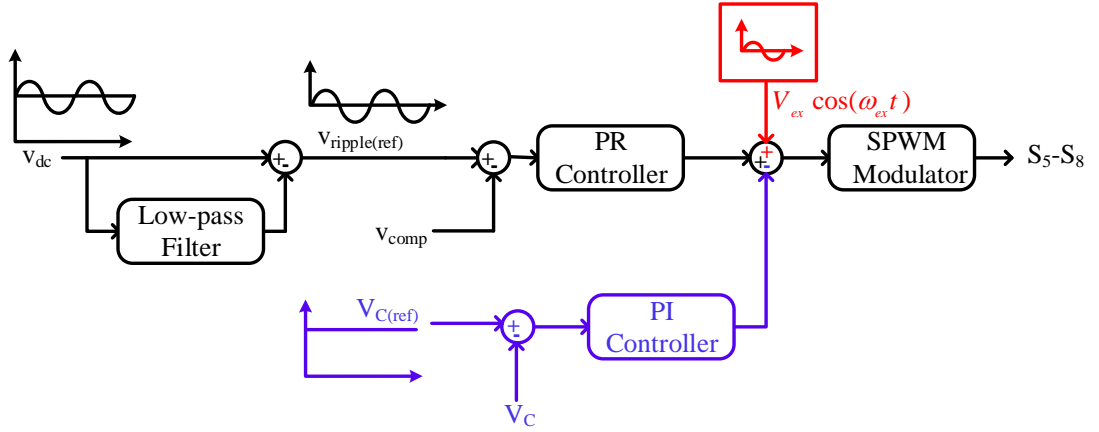


**Figure 5.7.** The proposed controller for pulsating power decoupling and IS.

To extract the maximum power of PV panels, the P&O algorithm is used as MPPT algorithm. This maximum power is used to determine the grid current reference [23]. The equations based on P-V curve are expressed as:

$$\frac{dP_{PV}}{dV_{PV}} = 0 \rightarrow \text{At MPP} \quad (5.26)$$

$$\frac{dP_{PV}}{dV_{PV}} > 0 \rightarrow \text{At the left of MPP} \rightarrow I_{oref}(k) = I_{oref}(k-1) - \Delta I \quad (5.27)$$

$$\frac{dP_{PV}}{dV_{PV}} < 0 \rightarrow \text{At the right of MPP} \rightarrow I_{oref}(k) = I_{oref}(k-1) + \Delta I \quad (5.28)$$

Where  $I_{oref}$  and  $\Delta I$  are the reference of grid peak current and current perturbation, respectively. The grid current is regulated with a PR controller as shown in Figure 5.9.

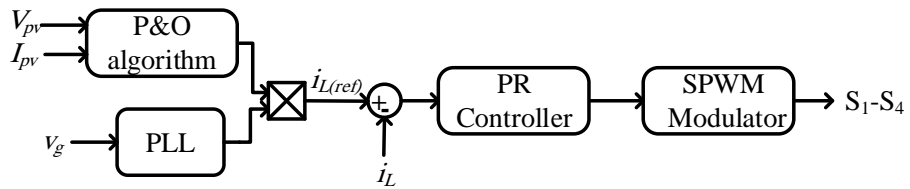


**Figure 5.8.** The grid current controller for pulsating power decoupling and IS.

## 5.2 Simulation and system design

### 5.2.1 Characteristics of the system under study

The system is composed of a full-bridge inverter as the main inverter connected to the grid through an inductive filter whose parameters are listed in Table 5.1, a full-bridge inverter used as a compensator and impedance spectroscopy tool whose parameters are listed in Table 5.2, and a PV array model whose parameters are listed in Table 5.3 [97].

**Table 5.1.** Main inverter parameters in the system with IS.

Parameter	Description	Value
$V_g$	Grid voltage	110V (rms)
$f$	Grid frequency	50 Hz
$f_{sw}$	Switching frequency	12 kHz
$f_{sampling}$	Sampling frequency	24 kHz
$L$	Filter inductance	4 mH

**Table 5.2.** The IS circuit parameters.

Parameter	Description	Value
$f_{sw1}$	Switching frequency	100 kHz
$f_{sampling1}$	Sampling frequency	100 kHz
$L_f$	Filter inductance	0.2 mH
$C_f$	Filter capacitance	0.01 $\mu$ F

**Table 5.3.** Specifications of the PV module at 1000 W/m<sup>2</sup>, 25 °C .

Parameter	Description	Value
P <sub>mpp</sub>	Maximum power	217.764 W
V <sub>mpp</sub>	Voltage at maximum power	27.6 V
I <sub>mpp</sub>	Current at maximum power	7.89 A
V <sub>oc</sub>	Open circuit voltage	37.38 V
I <sub>sc</sub>	Short circuit current	8.49 A
R <sub>s</sub>	Series resistance	0.7 Ω
R <sub>sh</sub>	Shunt resistance	377.95 Ω
C <sub>t0</sub>	Zero-voltage capacitance	7.95×10 <sup>-6</sup> F
Φ <sub>0</sub>	Zero-voltage junction potential	0.956 V
τ	Mean carrier lifetime	6.5×10 <sup>-7</sup> s
η	Diode ideality factor	1.006
n <sub>s</sub>	Series-connected modules per string	7
n <sub>p</sub>	Parallel strings	1

The PV power and voltage ratings are set at 1.5 kW and 193.2 V, respectively. The system is designed under the assumption of 20% permissible ripple on the DC-Link voltage ( $|\Delta v_{dc}| = 40$  V). So, from (5.20), the power of the compensator is  $S_{comp} = \frac{|\Delta v_{dc}|}{\sqrt{2}V_{dc}} S = 0.14S$ , which results in  $S_{comp} = 215$  W . With 20% voltage ripple on DC-Link and 10% on the compensator input capacitor, the values of the capacitors can be deduced from (1.5) and (5.25):  $C_{dc} = 310\mu F$  ,  $C_{comp} = 2000\mu F$  with  $V_c = 50V$  . As a result, a 300 μF, 400V film capacitor can be used for DC-Link and two parallel 1000 μF, 63V long lifetime electrolytic capacitors can be used for C<sub>comp</sub>. The performance evaluation of the PV system with the proposed circuit, is carried out using Matlab-Simulink. The simulated system is shown in Figure 5.10 with a dynamic model of the PV panel using (5.2) and (5.3).

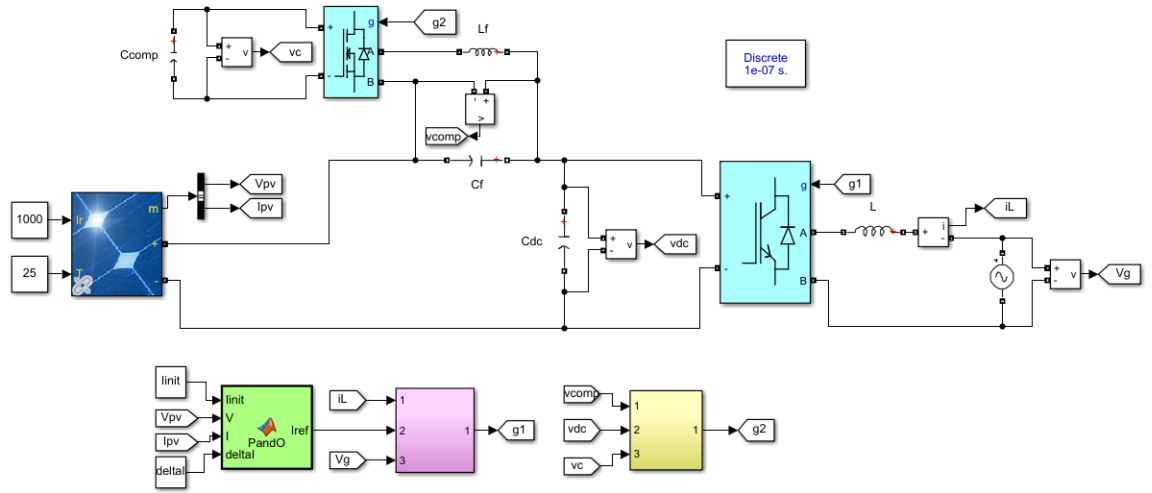


**Figure 5.9.** Simulated system of the pulsating power decoupling and IS circuit with Matlab-Simulink.

### 5.2.2 Theoretical impedance of the PV array

To evaluate the performance of the proposed system, the theoretical model of the PV array impedance is derived from the PV panel characteristics and equations (5.2) - (5.4) as follows:

$$R_{s\_array} = R_s \times \frac{n_s}{n_p} = 4.9\Omega \quad (5.29)$$

$$R_{p\_array} = (R_{sh} \times \frac{n_s}{n_p}) \parallel (R_d \times \frac{n_s}{n_p}) = 17.81\Omega \quad (5.30)$$

$$C_{p\_array} = (C_t \times \frac{n_p}{n_s}) + (C_d \times \frac{n_p}{n_s}) = 1.78\mu F \quad (5.31)$$

Where  $R_{s\_array}$ ,  $R_{p\_array}$ ,  $C_{p\_array}$  are series resistance, shunt resistance and shunt capacitor for the PV array, respectively. Thus, using (5.12), the theoretical impedance of the PV array can be expressed as:

$$Z(\omega_{ex}) = (4.9 + \frac{17.81}{1 + (31.7 \times 10^{-6} \times \omega_{ex})^2} - j \frac{564.6 \times 10^{-6} \times \omega_{ex}}{1 + (31.7 \times 10^{-6} \times \omega_{ex})^2}) \quad (5.32)$$

### 5.2.3 Tuning of the Impedance Spectroscopy

The Bode diagram of the impedance is plotted in Figure 5.11. As shown, the main variations in amplitude and phase are between 500 Hz and 80 kHz, which will be used as frequency range for IS. According to PV characteristics in Table 5.3,  $Z_{mpp} = \frac{193.2}{7.89} = 24.5\Omega$  and based on the Bode diagram, we can deduce that  $|Z|$  varies from  $|Z|_{\min} = 4.9\Omega$  to  $|Z|_{\max} = 22.73\Omega$ . In order to set the amplitude of the excitation signal, a compromise must be done between  $V_{ex}$  and  $\gamma$ . The larger  $V_{ex}$  is, the better will be the measurement resolution. However, the efficiency will be degraded as the maximum power point will be shifted. Assuming  $\gamma = 0.03$ ,  $V_{ex}$  is plotted in Figure 5.12 for different solar irradiances using (5.18). As a result, by considering  $V_{ex} = 1V$  under  $1000 \text{ W/m}^2$  solar irradiance, the maximum value of  $\gamma$  is limited to 0.03.

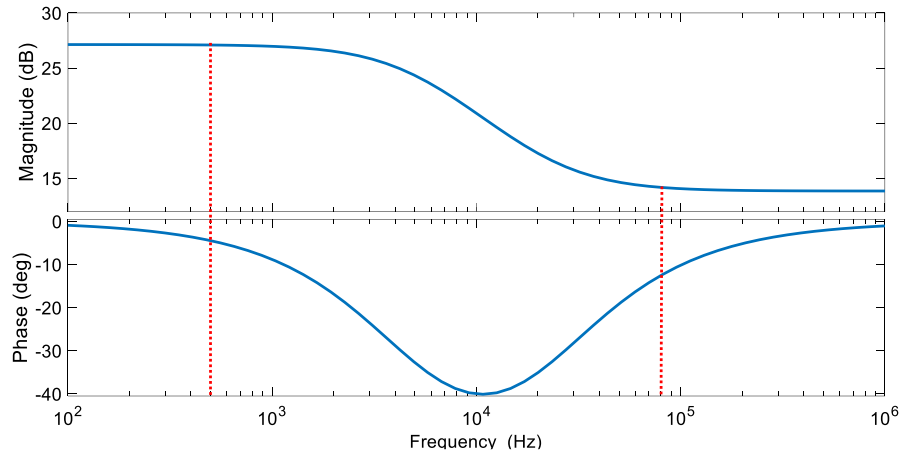


**Figure 5.10.** Bode diagram of the PV impedance.

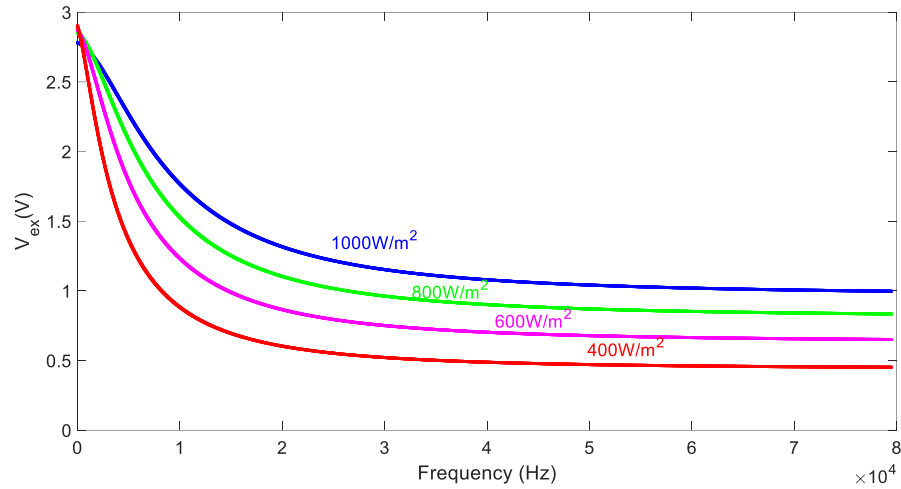


**Figure 5.11.** The voltage excitation in the case of  $\gamma = 0.03$ .

## 5.2.4 Simulation results

### 5.2.4.1 Simulation results under 1000 W/m<sup>2</sup> solar irradiance

The simulations are done under 1000 W/m<sup>2</sup> solar irradiance, and a temperature of 25<sup>0</sup>C .  $V_{ex}$  is set as 1V. As a consequence, based on (5.18),  $\gamma$  varies between 0.01 and 0.03. To evaluate the performance of pulsating power decoupling circuit, the waveforms of PV voltage, compensator voltage, DC-link voltage and grid voltage, in presence of 10kHz excitation signal, are shown in Figure 5.13. There is a peak-to-peak voltage ripple of 80V at twice the mains frequency on the DC-link voltage. However, on the PV side, the compensator reduces the voltage ripple to 15.3V, which corresponds to a significant reduction of 81% compared to the voltage across the DC bus. Hence, the PV voltage is smoother, and the pulsating power is effectively attenuated on the PV side.

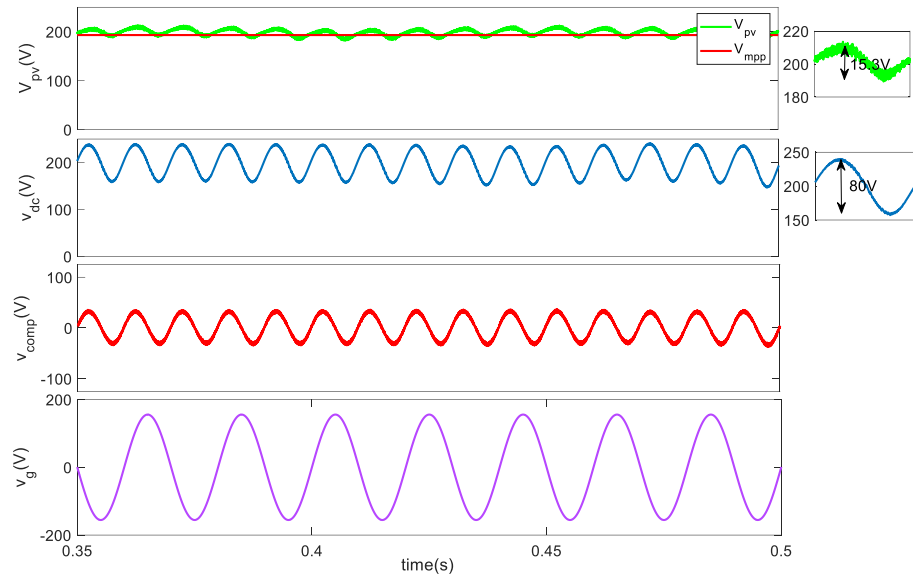


**Figure 5.12.** Simulated voltages for pulsating power decoupling and IS circuit: PV array ( $V_{pv}$ ), DC-link ( $v_{dc}$ ), compensator ( $v_{comp}$ ), grid ( $v_g$ ).

The PV power, PV and grid currents are plotted in Figure 5.14. A fast-response, high-precision phase-locked loop (A new simple structure PLL for both single and three-phase applications) is used to ensure a unity power factor [91]. The average PV power is 1505W, giving the MPPT efficiency of 98.7%. From the harmonic spectrum of the grid current shown in Figure 5.15, the amplitude of the grid current is 18.92A, and the THD is equal to 3.78%, which is compliant with the international standard IEC62040-3 that recommends THD < 5%. As it was expected, the excitation signal with an amplitude of 1V has no significant effect on system operation.

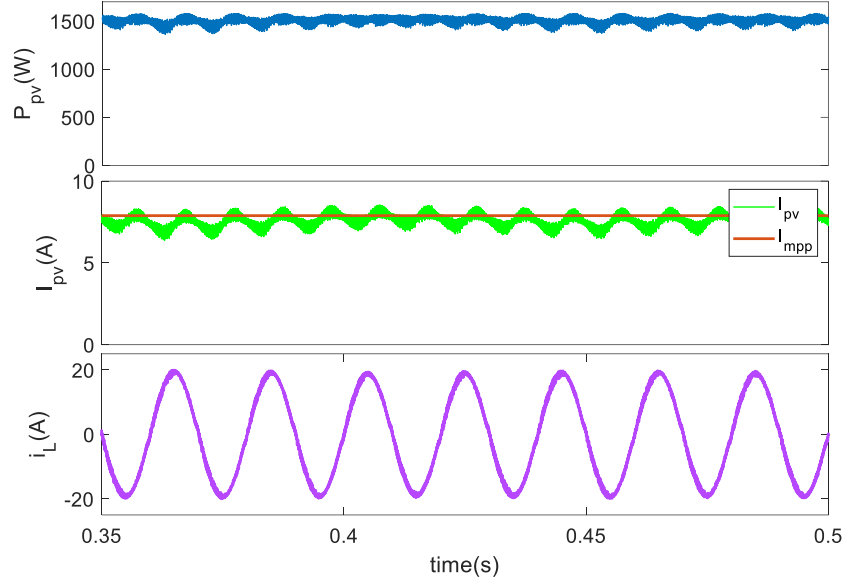


**Figure 5.13.** Simulation results for pulsating power decoupling and IS circuit: PV power ( $P_{pv}$ ), PV current ( $I_{pv}$ ), and grid current ( $i_L$ ).

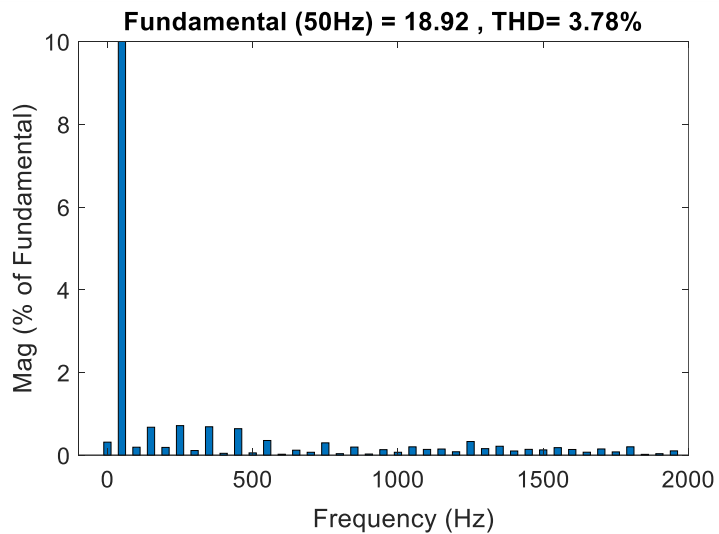


**Figure 5.14.** Grid current harmonic spectrum for pulsating power decoupling and impedance measurement circuit.

The PV and compensator voltages, and PV current are plotted in Figure 5.16 and Figure 5.17. The results show distortions at 10kHz and 200kHz induced by the IS excitation voltage and switching frequency, respectively. For the compensator, a unipolar sinusoidal pulse width modulator is used, which results in harmonics at twice the switching frequency and so,

the size of the filter is reduced. The amplitudes of PV excitation voltage and excitation current at 10kHz are equal to 1.02V and 0.096A, respectively. Besides, DC components of PV voltage and current are equal to 197.5V and 7.62A, respectively. As a result, using (5.16)  $\gamma$  is equal to 0.018.

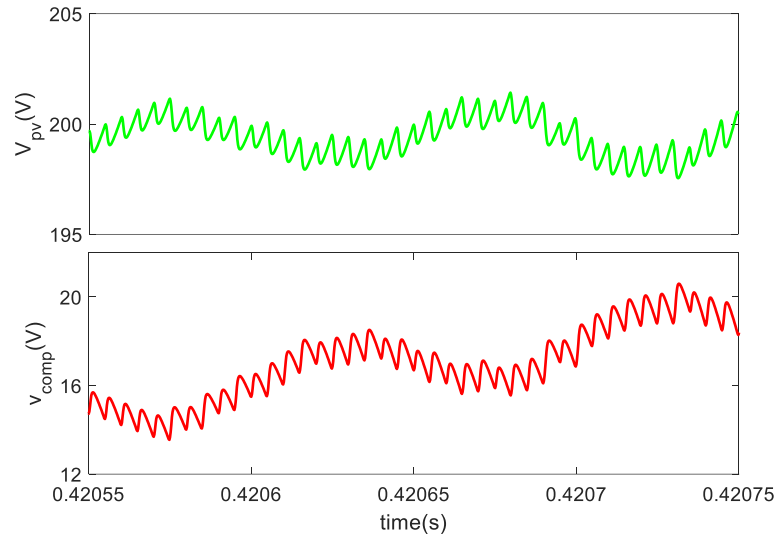


**Figure 5.15.** PV array ( $V_{pv}$ ), and compensator ( $v_{comp}$ ) voltages for pulsating power decoupling and IS circuit.

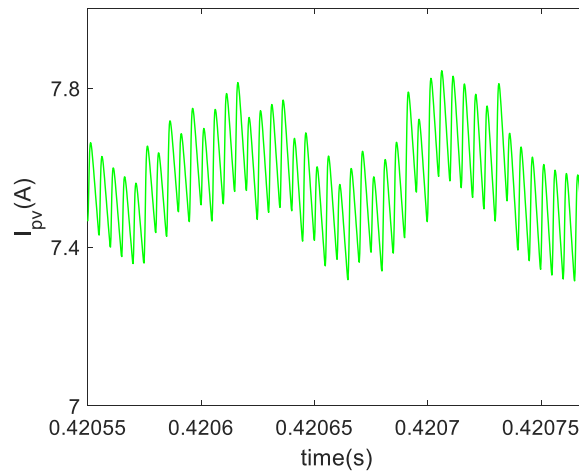


**Figure 5.16.** PV current for pulsating power decoupling and IS circuit.

An excitation signal with 27 different frequencies from 500 Hz to 80 kHz is used to estimate the impedance. Using FFT, the magnitude and the phase of PV voltage and current

are computed for every steady-state condition. The Nyquist diagram of the resulting impedance and the theoretical one computed from (5.32) are plotted in Figure 5.18.

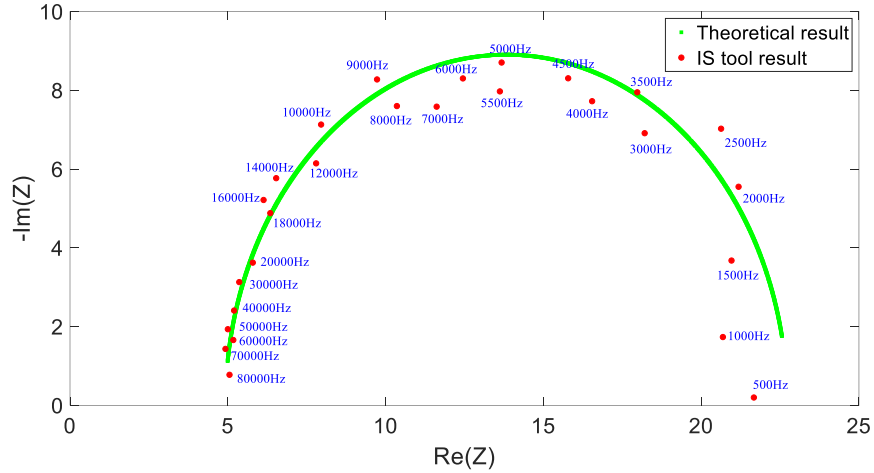


**Figure 5.17.** The Nyquist diagram of the theoretical and IS impedances.

#### 5.2.4.2 Comparison between theoretical and the IS

Curve fitting is used to further analyze the estimated impedance. The result is plotted in Figure 5.19. From Figure 5.19, the extracted series and shunt resistances are

$$\hat{R}_{s\_array} = 4.72\Omega \text{ and } \hat{R}_{p\_array} = 17.13\Omega, \text{ the cut off frequency at } \hat{R}_{s\_array} + \frac{\hat{R}_{p\_array}}{2} = 13.29\Omega$$

is roughly equal to  $f_c = 5500Hz$ , which results in  $\hat{C}_{p\_array} = 1.69\mu F$ . The results in Table 5.4 show that the relative error between model and estimated parameters is less than 5%, mainly due to the computation of FFT magnitudes. The Bode diagram of the estimated PV impedance is displayed in Figure 5.20.

**Table 5.4.** Evaluation of the parameters extraction from impedance spectroscopy.

Parameter	Model	Estimated	Relative error (%)
Series resistance ( $\Omega$ )	4.92	4.72	3.67
Shunt resistance ( $\Omega$ )	17.81	17.13	3,81
Capacitance ( $\mu F$ )	1.78	1.69	5

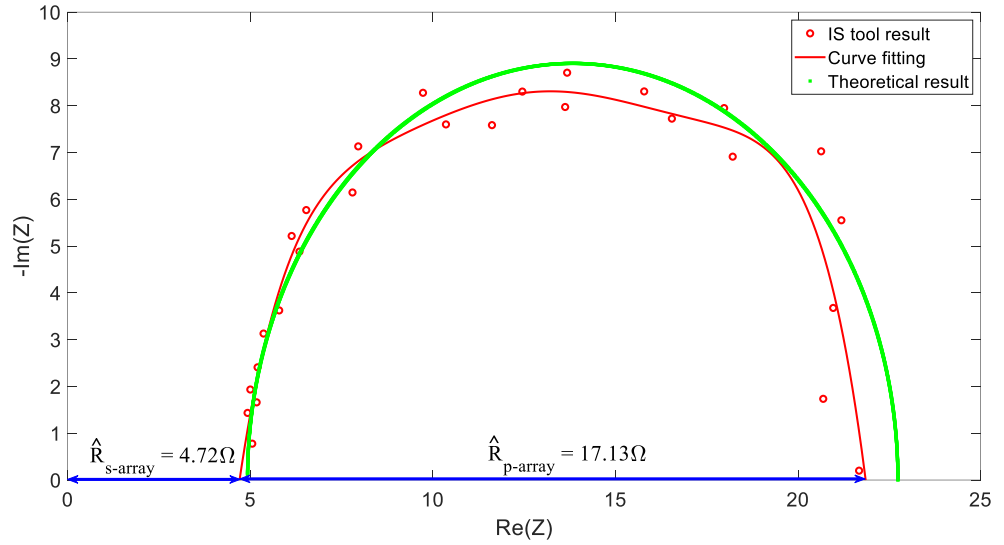


**Figure 5.18.** Nyquist plot of the PV array impedance using curve fitting.

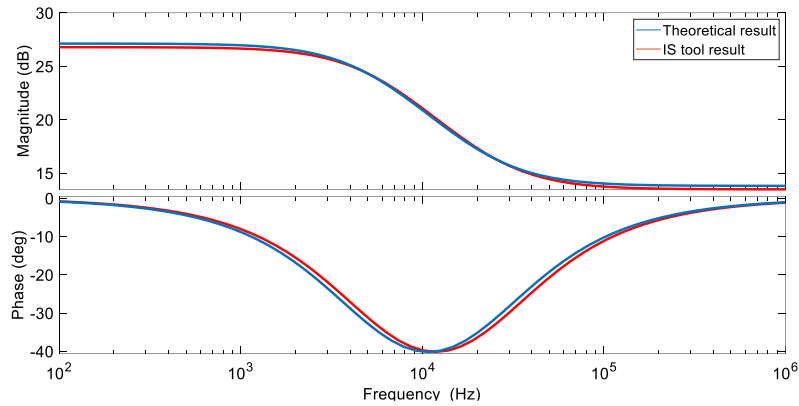


**Figure 5.19.** Bode diagrams of the theoretical and IS impedances.

### 5.2.4.3 Simulation results under 800 W/m<sup>2</sup> solar irradiance

To further evaluate the IS tool, simulation is done for 800 W/m<sup>2</sup> solar irradiance, and a temperature of 25<sup>0</sup>C . In this case, the theoretical parameters become  $R_{s\_array} = 4.9\Omega$  ,  $R_{p\_array} = 24.26\Omega$  , and  $C_{p\_array} = 1.76\mu F$  . The Nyquist diagram of the IS and the theoretical impedance are displayed in Figure 5.21. From this figure,  $\hat{R}_{s\_array} = 4.71\Omega$  ,

$\hat{R}_{p\_array} = 23.19\Omega$ , the cut off frequency at  $\hat{R}_{s\_array} + \frac{\hat{R}_{p\_array}}{2} = 16.3\Omega$  is roughly equal to  $f_c = 4000Hz$ , which results in  $\hat{C}_{p\_array} = 1.71\mu F$ . The results show that the relative error is less than 4.5%.

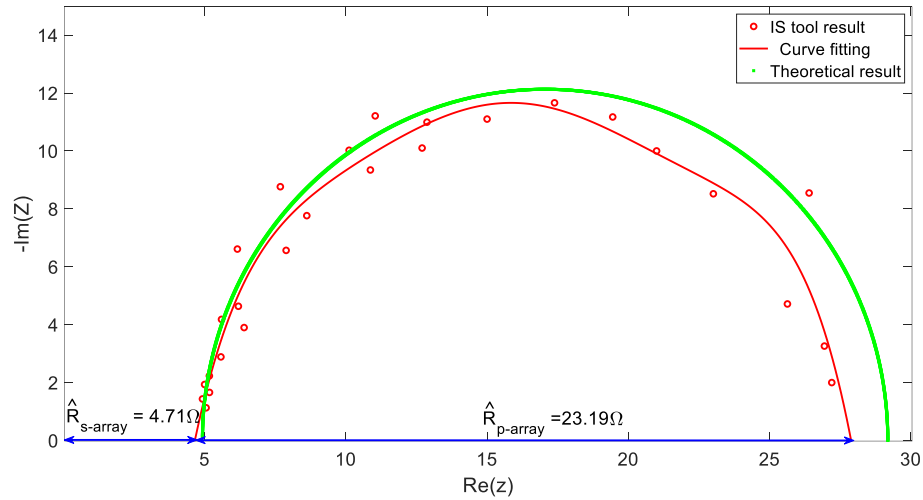


**Figure 5.20.** The Nyquist diagram of the theoretical and IS under 800W/m<sup>2</sup>.

### 5.3 Conclusion

This chapter has proposed the design and control of a dual-function impedance spectroscopy tool and pulsating power compensator for a single-phase grid-connected PV system. We have taken the benefit of pulsating power decoupling circuit without using any additional equipment for impedance spectroscopy, which is a fault diagnosis tool. The proposed circuit is an H-bridge inverter that operates independently from the main inverter and has a much less power rating. An excitation voltage at different frequencies is added to the system using the compensator and the response is used for impedance measurement. The larger is the amplitude of the injected voltage, and the better will be the impedance resolution. However, it may affect the PV panel performance, and thus, there is a tradeoff for setting the magnitude, which has been addressed. Simulation results have shown that the proposed method can reduce up to 81% of the pulsating power and estimate the parameters of the PV array model with a relative error lower than 5%. These estimated parameters can be used for fault detection and diagnosis of PV panels.

## **Chapter 6 Conclusion and perspectives**

Nowadays, renewable energies have gained great importance in providing alternative energy to overcome the energy crisis and mitigate environmental issues. Among RESs, grid-connected photovoltaic systems have been widely developed. It is mainly because PV energy is green, free, inexhaustible, and more available. In addition, PV generation systems are attracting more attention due to government incentives, reduced prices for PV panels and advances in power electronics and semiconductor technologies. The single-phase interface composed of a voltage inverter is usually adopted to connect low power PV plant to the grid. The connection of PV power plant to the grid can be done with single or two-stage power converters. In two-stage PV systems, the interface converter includes a DC/DC converter and an inverter. In single-stage systems, the DC/DC converter has been removed, reducing the size and the cost. However, in this case, the operating voltage range is limited at low irradiation, which leads to loss of output power and reduced efficiency. This issue was not yet addressed.

In this work, the critical issues in the single-stage single-phase grid-connected PV inverter including reliability and efficiency have been addressed.

In the first part of this work, MPPT algorithm and grid-side controller are studied. The proposed controller is a fast terminal sliding mode –direct power controller. The modified MPPT algorithm proposes a P&O algorithm with power output to be adopted with power control method. The effectiveness of the proposed controller was validated using different simulation and experimental tests. The results show a good decoupling capability of the two active and reactive power control loops, a good coordination between the grid and PV controllers, and robustness against parameters' mismatches. The comparisons with other references confirm the fast transient response of the controller and a low THD of grid current.

In the second part, a dual-function compensator has been developed. The proposed compensator can overcome two important issues in single-stage single-phase PV systems; pulsating power, and voltage drop under low irradiance condition. The proposed system uses a flyback converter, and an H-bridge rated at 12% and 15% of the main inverter rated power, respectively. The compensator is connected as a series converter between the inverter and the PV panels. The control and modulation are independent from the main inverter, which

makes it easy to design and control. The system is evaluated under normal and low irradiance conditions. Under normal irradiance condition, the compensator only works in pulsating power mode, which is handled using the H-bridge. However, under low irradiance condition, the circuit compensates for the pulsating power and the voltage drop. Thus, the compensator fed from the PV panel injects active power, which is done with the flyback converter. The control of the proposed hybrid compensator is performed with usual PI, PIR and PR controllers. A comprehensive evaluation of the costs and power losses of the system has been performed and compared to a conventional two-stage system with series active power decoupling. The results show higher efficiency, and lower cost of the proposed system. Even with a severe voltage drop, the efficiency drop is 0.2%, which is much less than the power loss of a conventional boost converter, which is about 2-3%. To evaluate the dynamics of the proposed hybrid compensator, the system has been tested under uniform and non-uniform irradiation. The compensator tracks the voltage variations with a time response lower than 20ms, which is acceptable regarding the dynamics of the PV. Besides, the proposed structure was compared with other methods in different comparisons metrics. The proposed structure exhibits higher metrics including efficiency and reduction in voltage ripple than most of the other active power decoupling proposals in the literature for different rated powers. It also shows the minimum number of components at nominal power and the components of the compensator are rated at 15% of the nominal power.

In the third part of this work, monitoring and fault diagnosis of PV modules in the single-stage single-phase PV system were addressed. The proposed fault diagnosis method is based on online impedance spectroscopy without additional equipment, and does not require to interrupt power production. The idea consists of using a pulsating power decoupling circuit as an impedance spectroscopy tool. This dual-function circuit is a low power high frequency H-bridge, which is located as a series circuit between the PV panels, and the main inverter. It injects a voltage composed of two AC components; the ripple voltage is responsible to mitigate pulsating power and the excitation voltage is devoted to estimate the impedance of the PV panels. The excitation voltage is injected over a range of frequency compliant with the dynamics of the PV panels. The amplitude is tuned to minimize the side effects. The control of the proposed circuit is performed using PR and PI controller

independent from the main inverter. Simulation results are compared to the theoretical analysis of the impedance. The results have shown that the pulsating power was significantly reduced, and the parameters of the PV panels were estimated with a relative error lower than 5%.

Concerning future works, hereafter are several proposals:

- For the design of the power converters:

One could envisage to integrate the pulsating power and the voltage drop compensator in one single converter with reduced number switches and elements. The pulsating power stage could be replaced with new converters that require less semiconductors.

The design of the compensator could also take benefit of wide bandgap (SiC or GaN) semiconductors to increase switching frequency. This may improve the efficiency and reduce the size of the passive elements.

It would also be relevant to evaluate the integration of the IS electronics with the power decoupling and voltage drop compensation.

- On the control of the power converters

At first, the robustness of the proposed control system to model parameters variations should be further evaluated.

It would be interesting to evaluate advanced control methods of the compensator to improve the capability of voltage ripple reduction. This would lead to further reduction of the DC-link capacitor value. Also, high performance Wavelet-Based filters can be developed to extract the voltage ripple with very high dynamic response.

To reduce the cost and increase the reliability, the input DC voltage could be estimated. Therefore, a voltage transducer can be removed.

- Experimental testbed

Experiments with PV emulator and PV panels should be conducted to further assess the performance of the proposal. It could also allow to analyze the effect of the decoupling circuit on the PV panel.

The impedance spectroscopy should be evaluated on the test bed.

The fault diagnosis method should be extended to the classification of different PV faults.

## Résumé en Français

**Titre :** Conception et contrôle d'un nouveau circuit de découplage de puissance pulsée pour les systèmes photovoltaïque connecté au réseau

**Mots clés:** Système PV connecté au réseau, convertisseur à un étage, compensation de la puissance pulsée, compensateur de chute de tension, diagnostic de défaut.

### ➤ Introduction

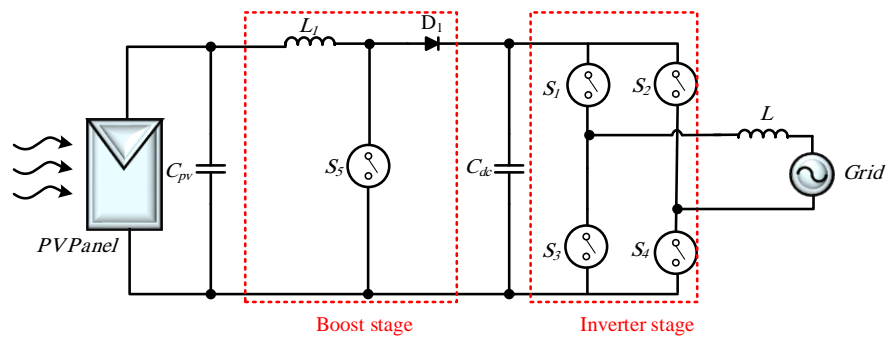
En raison des problèmes environnementaux, les énergies renouvelables devraient être les sources d'énergie qui connaissent la plus forte croissance pour la production d'électricité. Leur contribution devrait être doublée en 2040 par rapport à 2012. Parmi les sources d'énergie renouvelables, les centrales photovoltaïques (PV) ont connu la croissance la plus rapide grâce aux progrès réalisés dans les matériaux semi-conducteurs, le conditionnement et la réduction des coûts. En outre, le module PV ne comporte aucune pièce mobile, ce qui en fait un dispositif à longue durée de vie, robuste et nécessitant peu d'entretien. D'ici la fin du siècle, on s'attend à ce qu'il ait la production la plus importante parmi les sources d'énergie renouvelables, jusqu'à 60 % de l'énergie totale.

La production d'électricité à partir de panneaux photovoltaïques est passée d'un système autonome à un système connecté au réseau car les technologies des convertisseurs électroniques de puissance et les méthodes de contrôle sont devenues plus matures. L'augmentation de la fiabilité, de l'efficacité et la réduction des coûts du système sont des objectifs ambitieux pour chaque système électrique, y compris les systèmes PV connectés au réseau.

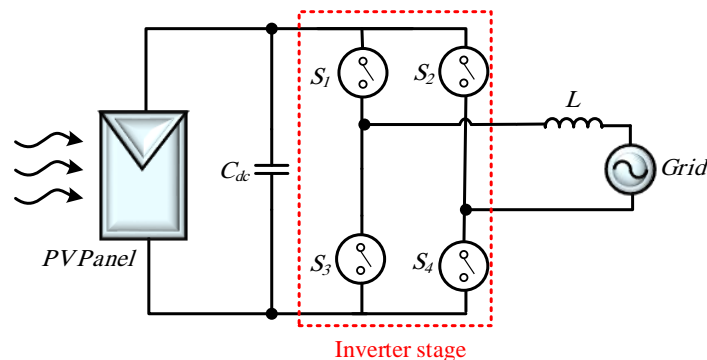
Une étape importante pour augmenter l'efficacité du système PV est de capturer la puissance maximale des panneaux PV et de la transférer au réseau. Par conséquent, l'algorithme de suivi du point de puissance maximale (MPPT) et le contrôleur du convertisseur connecté au réseau sont cruciaux. Pour les applications de faible puissance,

l'onduleur monophasé est le meilleur compromis pour les interfaces de convertisseur de puissance. Cependant, les systèmes d'alimentation monophasés sont confrontés à des oscillations de puissance à une fréquence double de celle du réseau (puissance pulsée) sur le bus continu. Cette perturbation réduit le rendement et la durée de vie des panneaux photovoltaïques. Elle dégrade également les performances de l'algorithme de suivi du point de puissance maximale. Par conséquent, il faut développer un système de contrôle efficace et également l'élimination de la puissance pulsée pour les systèmes PV monophasés connectés au réseau. Il faut aussi mettre en place une maintenance active basée sur la surveillance continue des panneaux PV pour améliorer la fiabilité, la disponibilité et la sécurité du système PV.

Il existe deux configurations principales pour les systèmes photovoltaïques monophasés connectés au réseau : les systèmes à un ou deux étages, illustrés à la Figure 1.



a) Configuration à deux étages



b) Configuration à un étage

**Figure 1.** Configuration des onduleurs PV connectés au réseau.

La centrale PV est connectée au réseau par l'intermédiaire d'un convertisseur DC-DC et d'un onduleur dans une configuration à deux étages. Ainsi, la tension requise pour alimenter le réseau est obtenue par un convertisseur élévateur dimensionné à la puissance nominale. La suppression de cet étage permet de réduire la taille et les coûts en passant à un système à un seul étage. Cependant, la plage de tension de fonctionnement est limitée en cas de faible irradiation, ce qui entraîne une perte de la puissance de sortie. Par conséquent, les structures qui peuvent maintenir la plage de tension de fonctionnement gagnent en intérêt dans les configurations à un étage.

### ➤ Objectifs

Trois principaux sujets ont été traités dans ce travail sur les structures de conversion à un étage:

- La commande de l'onduleur,
- L'atténuation des effets des oscillations de puissance et la compensation de la chute de tension due à la baisse de l'éclairement,
- La surveillance du panneau PV par l'estimation de l'impédance.

#### • *La commande de l'onduleur*

Dans un système PV à un seul étage, l'algorithme MPPT et le contrôleur de courant de réseau pilotent le seul convertisseur de puissance, à savoir l'onduleur. Une réponse transitoire rapide est essentielle pour l'injection de puissance active ou réactive dans le réseau. De plus, une bonne qualité d'énergie avec une faible distorsion harmonique totale (THD) du courant du réseau est requise dans un système connecté au réseau. Ainsi, la coordination efficace entre le réseau et les contrôleurs côté PV permet de supprimer les boucles internes, ce qui augmente la réponse dynamique.

Dans ce travail, nous développons le contrôle de l'onduleur PV connecté en intégrant ces différentes contraintes.

- *Oscillations de puissance et compensation de la chute de tension*

Dans un système monophasé à un étage de conversion, la puissance instantanée peut s'écrire:

$$p_{ac}(t) = P_o + P_o \cos(2\omega t) \quad (1)$$

Où  $P_o$  est la puissance moyenne. La composante oscillante va être transmise sur le bus continu et se traduire par une composante oscillante sur la tension.

$$v_{dc}(t) = V_{dc} + v_{ripple}(t) \quad (2)$$

Il convient de mentionner que pour les applications photovoltaïques, cette ondulation de la tension réduit l'efficacité du panneau solaire.

Les solutions pour résoudre ce problème sont principalement divisées en deux catégories : les méthodes de découplage passif et actif.

Les méthodes de découplage passif consistent à augmenter l'inductance ou la capacité du bus continu. Récemment, une plus grande attention a été accordée au stockage d'énergie capacitif pour réduire le coût et le volume par rapport au stockage d'énergie inductif. En outre, les inductances peuvent augmenter les pertes de puissance en raison de la résistance série équivalente élevée. Par conséquent, la solution habituelle consiste à connecter un condensateur électrolytique sur le bus continu pour atténuer cette perturbation.

Cependant, ces condensateurs souffrent d'un volume et d'un poids élevés ainsi que d'une faible fiabilité. En général, la durée de vie des condensateurs électrolytiques à des températures de 40-105°C est d'environ 1000-7000 heures. Cette durée de vie est courte comparée à celle des modules photovoltaïques qui est de plus de 20 ans. En outre, pour une augmentation de 10°C, la durée de vie des condensateurs électrolytiques sera réduite de moitié, selon l'équation d'Arrhenius.

Une solution consiste donc à remplacer les condensateurs électrolytiques par des condensateurs à film, dont la durée de vie est plus longue. Cependant, à capacité égale, les condensateurs à film sont plus grands et plus chers que les condensateurs électrolytiques.

L'idée derrière les topologies de découplage actif est de dévier la puissance pulsée vers un autre dispositif de stockage d'énergie combiné à un convertisseur statique. Ainsi, puisque

le dispositif de stockage d'énergie ne compense que la puissance pulsée, des condensateurs à film à longue durée de vie et à faible volume peuvent être utilisés.

D'autre part, les systèmes PV à un seul étage souffrent d'une plage de fonctionnement réduite en raison des variations d'irradiation et de la température. Ainsi, la tension de fonctionnement (du point de puissance maximale) peut se situer en dehors de la plage limitée, ce qui réduit le rendement de conversion de puissance de 4 %. Ainsi, l'absence d'un convertisseur boost dans ces systèmes à un étage peut diminuer le rendement de conversion dans des conditions de faible irradiation. Dans cette configuration, il faut trouver le moyen de compenser la chute de tension et la limitation de la plage de fonctionnement de l'onduleur.

- ***Surveillance de l'état du panneau PV***

La maintenance des panneaux PV est devenue cruciale avec la croissance exponentielle des centrales PV. Les modules PV souffrent de diverses défaillances dues à des raisons endogènes (vieillissement, court-circuit, circuit ouvert, ...) et exogènes (transport, ombrage, encrassement, ...). Ces défaillances peuvent entraîner une réduction de l'efficacité de la conversion de l'énergie, un endommagement du module ou même un incendie. Par conséquent, la surveillance et le diagnostic des défauts des modules PV sont essentiels pour augmenter la fiabilité, l'efficacité et la sécurité du système. Différentes méthodes ont été proposées pour la détection et le diagnostic des défauts des modules PV. Ces méthodes peuvent être classées en deux grandes familles : l'inspection visuelle (assistée par l'homme ou par une caméra) et l'analyse automatique.

L'inspection visuelle humaine ne convient qu'aux petites installations photovoltaïques et peut souffrir d'erreurs d'interprétation. L'inspection assistée par caméra repose sur l'utilisation d'images capturées par des drones ou des UAV. Outre leur coût élevé, les images doivent être corrigées par des techniques lourdes de traitement afin d'éliminer/compenser les nuisances dues aux conditions environnementales. L'analyse automatique consiste à traiter les données brutes d'entrée pour extraire les caractéristiques des défauts. Les données d'entrée sont généralement la tension et le courant PV, l'éclairement énergétique et la température. L'un des principaux problèmes est de surveiller les modules PV sans interrompre la production d'énergie, et d'utiliser uniquement les mesures déjà disponibles. Notre étude a

développé une méthode de surveillance qui tire profit de notre structure de conversion de puissance et de son contrôle. Elle devrait fonctionner en ligne sans équipement supplémentaire et sans interruption de la production d'énergie.

Les principales contributions de ce travail sont :

- le développement de commande comprenant un algorithme MPPT, et un contrôleur côté réseau,
- le développement d'un circuit électronique qui permet de compenser la puissance pulsée et la chute de tension due à une faible irradiation,
- le développement d'un circuit électronique qui compense la puissance pulsée et permet simultanément d'estimer l'impédance du panneau PV.

Le système avec le contrôleur proposé est illustré à la Figure 2.

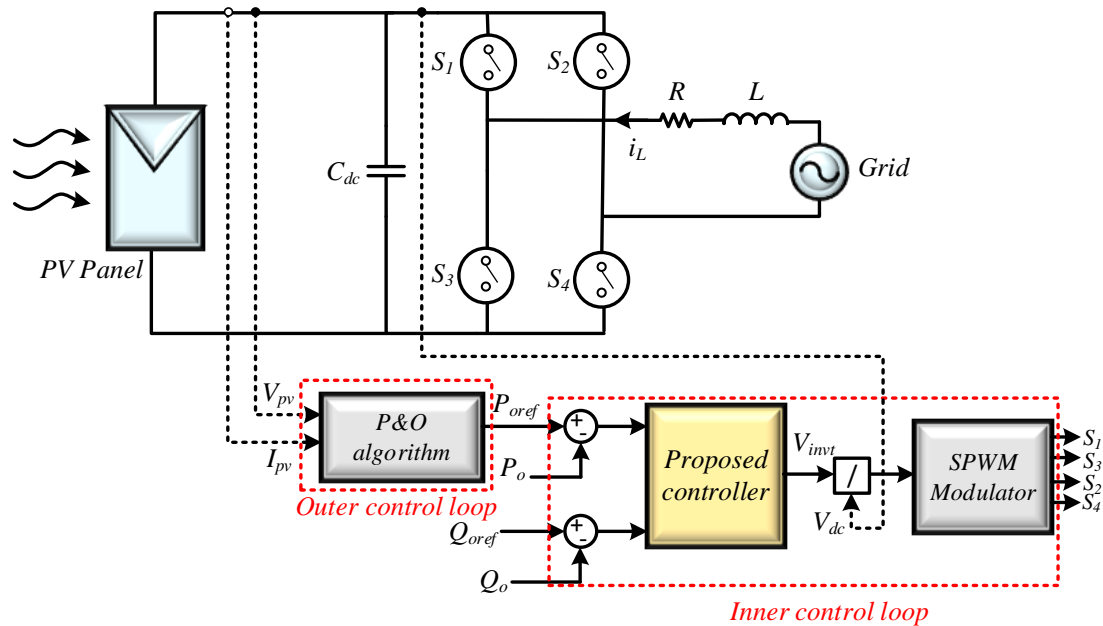


**Figure 2.** Structure du convertisseur à un étage et de sa commande

Le banc d'essai expérimental est représenté sur la Figure 3. Une source de courant continu réglable alimentée par un redresseur triphasé est utilisée pour émuler la source PV et son algorithme MPPT. L'onduleur à un étage est composé de commutateurs de puissance IGBT IKW40N120H3 (40A/1200V) pilotés par des pilotes de porte à optocoupleur

HCPL3120. L'algorithme de contrôle est implémenté dans un TMS320F28335, un DSP de Texas Instruments. Cette carte à base de DSP fournit plusieurs modulateurs de largeur d'impulsion améliorés à haute résolution avec des buffers de sortie et des convertisseurs analogiques-numériques 12 bits à haute vitesse multicanaux, ce qui la rend très pratique pour les applications d'électronique de puissance. Un prototype de carte de pilotage via un optocoupleur HCPL3120 et un courant de crête maximum de 2,5A a été conçu pour contrôler les interrupteurs de puissance. Des capteurs à effet Hall, LTS25NP et LV25P, sont utilisés pour mesurer le courant et la tension, respectivement.

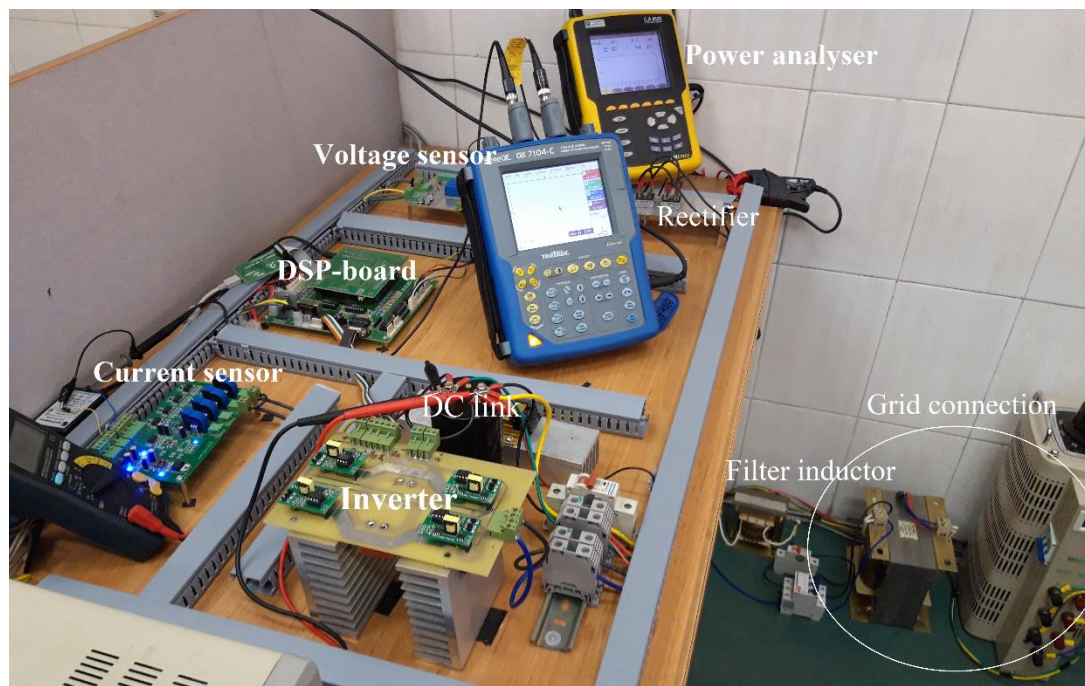


**Figure 3.** Structure du banc expérimental

Les résultats expérimentaux en régime permanent sont présentés sur la Figure 4. La puissance active est égale à 1kW tandis que la puissance réactive est presque nulle (étant donné la valeur réelle qui n'est pas nulle comme on peut l'observer à partir du facteur de puissance). On peut également remarquer les formes d'onde sinusoïdales de la tension et du courant du réseau. La Figure 5 représente le spectre du courant du réseau. Elle montre un THD égal à 3,5 % conforme à la norme internationale.

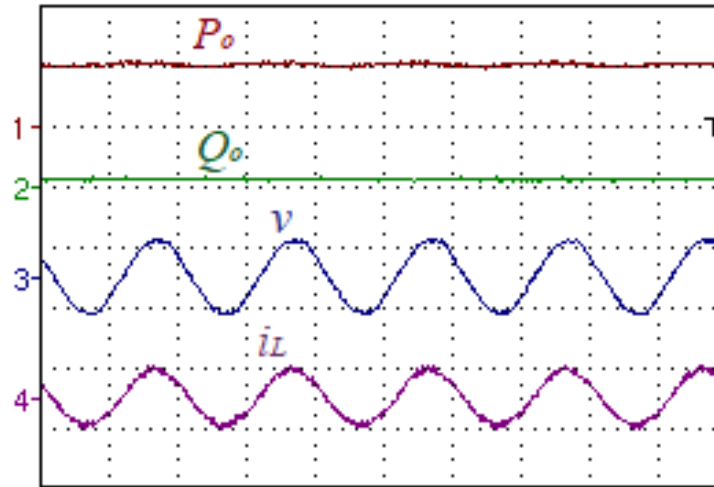


**Figure 4.** Résultats expérimentaux en régime permanent;  $t$ , (10ms/div),  $P_o$  (1000 W/div),  $Q_o$  (500 VAr/div),  $v$  (500V/div), and  $i_L$  (26A/div).

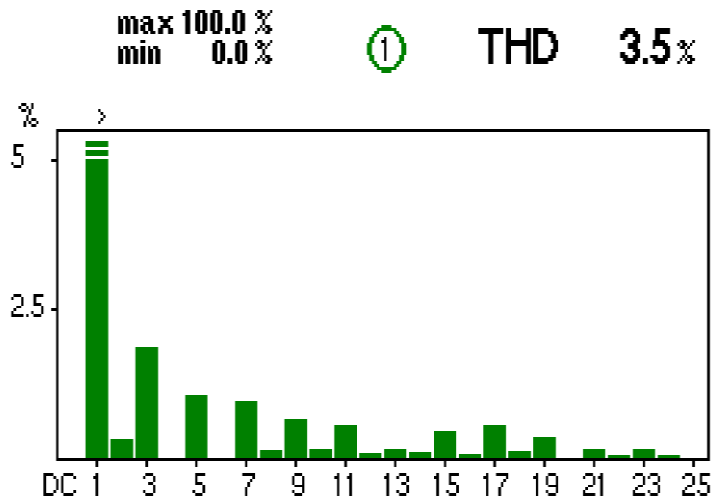


**Figure 5.** Spectre du courant de ligne

Pour évaluer les performances du régulateur en cas de variations du rayonnement solaire dues, par exemple, à la présence de nuages, on introduit des variations par paliers de

50 % à 100 % et de retour à 50 % de la valeur nominale de la référence de puissance active. Les résultats sont représentés sur la Figure 6. Les performances de suivi de la puissance sont très bonnes, avec un dépassement quasi nul et une réponse temporelle de 10 ms. Le transitoire sur le courant du réseau est négligeable et il n'y a pas de perturbation de la tension du réseau.

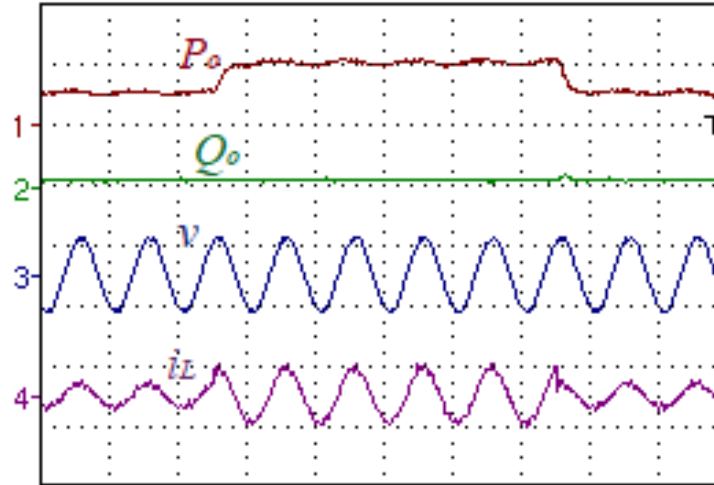


**Figure 6.** Résultats expérimentaux en régime dynamique;  $t$ : (10ms/div),  $P_o$  (1000 W/div),  $Q_o$  (500 VAr/div),  $v$  (500V/div), and  $i_L$  (26A/div).

Le compensateur hybride proposé est illustré à la Figure 7. Il est constitué d'un convertisseur DC/DC isolé à deux ports et d'un convertisseur DC/AC.

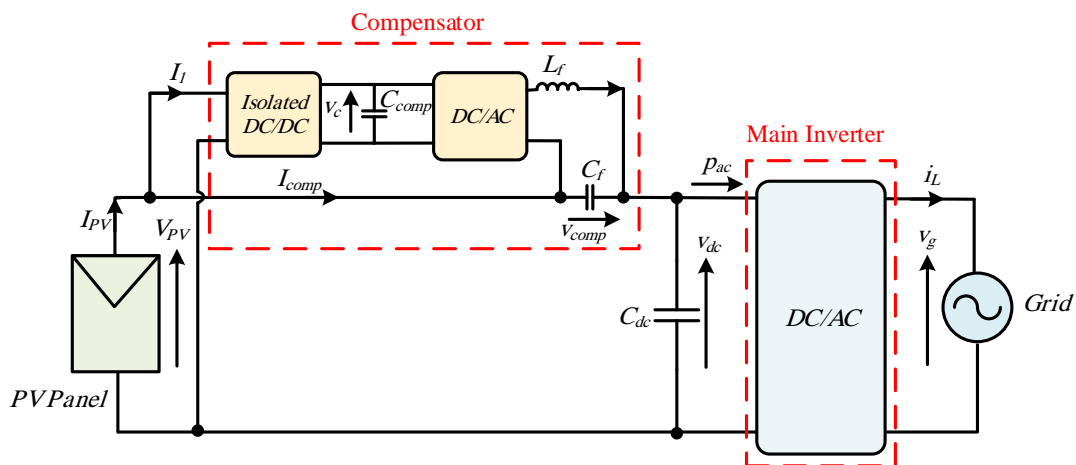
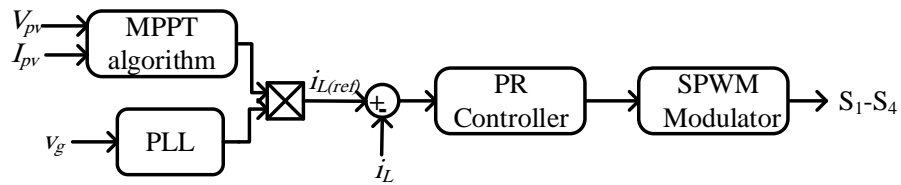
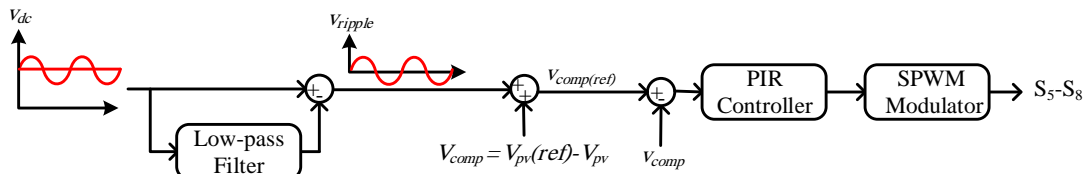


**Figure 7.** Structure du convertisseur hybride connecté au réseau.

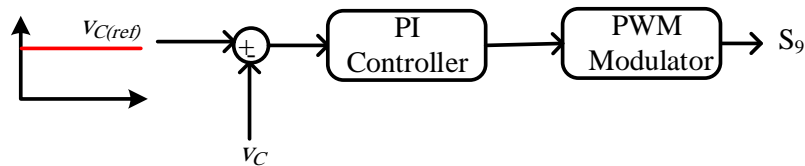
La commande du compensateur hybride, qui se compose de trois parties, est illustrée à la Figure 8 : la commande de l'onduleur principal, la commande du pont en H et la commande du convertisseur Flyback.



a) Commande de l'onduleur



b) Commande du pont H



c) Commande du Flyback

**Figure 8.** Structure de commande du convertisseur hybride connecté au réseau.

Le banc expérimental est représenté sur la Figure 9.

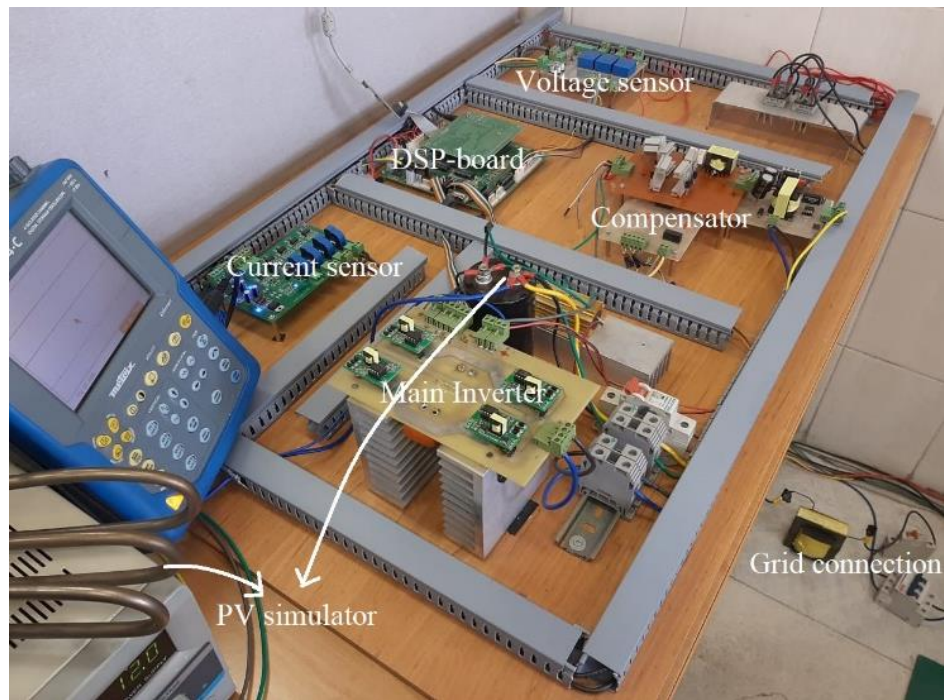


**Figure 9.** Banc expérimental du compensateur hybride.

L'expérience suivante a consisté à évaluer les performances du système dans des conditions d'irradiation nominales. La Figure 10 montre présente la tension du réseau, la tension PV, la tension du bus continu et la tension du compensateur. La tension continue moyenne de l'onduleur est égale à 200V, et les ondulations de tension à deux fois la fréquence du réseau ont une valeur crête à crête de 82V. Comme on peut l'observer, le compensateur suit parfaitement les ondulations de la tension. Par conséquent, les oscillations de tension crête à crête du côté PV ne sont plus que de 12,5 V, ce qui correspond à une réduction de 85% par rapport aux ondulations de la tension du bus continu. Ainsi, comme prévu, la tension PV est lissée, et la puissance pulsée est atténuée du côté du panneau PV.

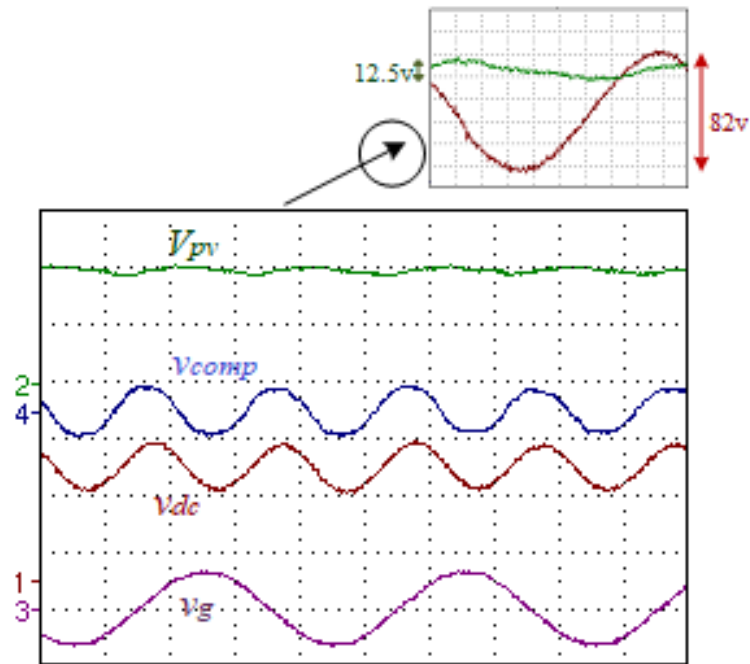


**Figure 10.** Résultats expérimentaux de la compensation des oscillations de puissance sous irradiation nominale.

La dernière expérience est réalisée avec une charge capacitive ayant un facteur de puissance de 0,9. Le courant et la tension du réseau, la tension du lien CC et la tension PV sont représentés sur la Figure 11. Les résultats montrent la capacité du circuit à échanger de la puissance réactive.

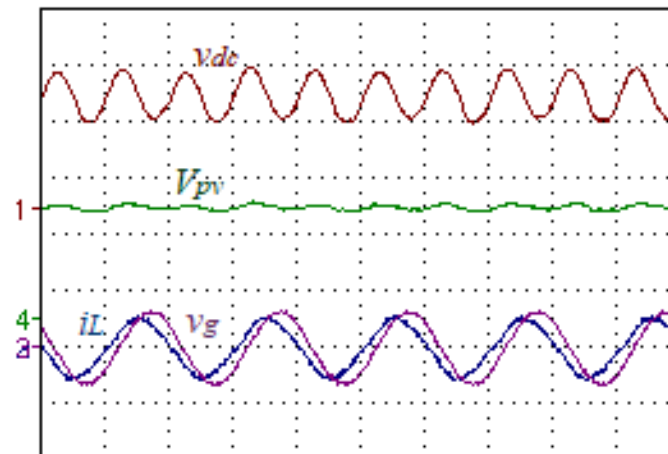


**Figure 11.** Résultats expérimentaux de la compensation des oscillations de puissance avec facteur de puissance non unitaire.

Le compensateur proposé pour l'impédance spectroscopique est illustré à la Figure 12.

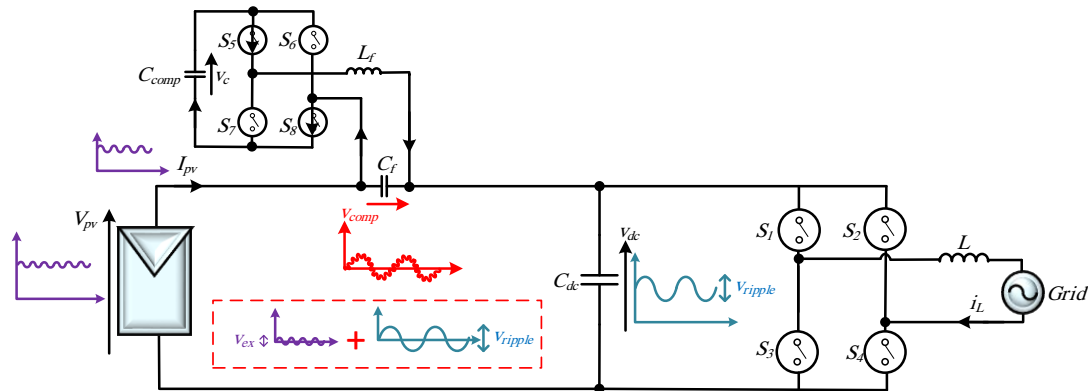


**Figure 12.** Compensateur et injection de tension pour l'impédance spectroscopique.

Un signal d'excitation avec 27 fréquences différentes de 500 Hz à 80 kHz est utilisé pour estimer l'impédance. A l'aide de la FFT, l'amplitude et la phase de la tension et du courant PV sont calculées pour chaque condition d'équilibre. Les diagrammes de Nyquist de l'impédance résultante et l'impédance théorique sont représentés sur la Figure 13.

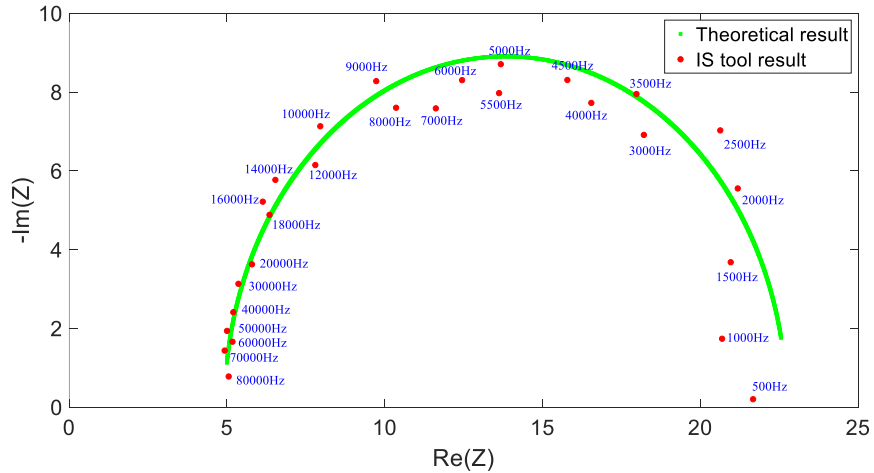


**Figure 13.** Diagramme de Nyquist de l'impédance.

### ➤ Conclusion

Dans ce travail, nous avons proposé des solutions pour améliorer la fiabilité et l'efficacité des onduleurs PV monophasés à un seul étage connecté au réseau.

Dans la première partie de ce travail, l'algorithme MPPT et le contrôleur côté réseau ont été étudiés. Le régulateur proposé est un régulateur de puissance direct à mode glissant dit à mode terminal rapide. L'algorithme MPPT modifié propose un algorithme P&O avec la puissance en grandeur de sortie. L'efficacité du contrôleur proposé a été validée par différents résultats obtenus en simulation et sur un banc expérimental. Les résultats montrent une bonne capacité de découplage des deux boucles de contrôle des puissances active et réactive, une bonne coordination entre le réseau et les contrôleurs PV, et une robustesse contre les variations paramétriques. Les comparaisons avec d'autres travaux de la littérature confirment les bonnes performances en régime transitoire du contrôleur et le faible THD du courant de réseau.

Dans la deuxième partie, un compensateur à double fonction a été développé. Le compensateur proposé permet simultanément de compenser la puissance pulsée et la chute de tension dans des conditions de faible irradiation. Le système proposé utilise un convertisseur flyback, et un pont complet dimensionnés respectivement à 12% et 15% de la puissance nominale de l'onduleur principal. Le compensateur est connecté en série entre l'onduleur et les panneaux PV. Le contrôle et la modulation sont indépendants de l'onduleur principal, ce qui facilite sa conception et son contrôle. Le système est évalué dans des conditions d'irradiation normale et faible. Dans des conditions d'irradiation normales, le compensateur ne fonctionne qu'en mode de compensation de la puissance pulsée, grâce au pont en H. Dans des conditions de faible irradiation, le circuit compense la puissance pulsée et la chute de tension. Ainsi, le compensateur alimenté par le panneau PV injecte de la puissance active, ce qui est fait avec le convertisseur flyback. Le contrôle du compensateur hybride est effectué avec des usuels que sont le PI, le PIR et le PR. Une évaluation complète des coûts et des pertes de puissance du système a été réalisée, et comparée à un système conventionnel à deux étages avec découplage de la puissance active en série. Les résultats montrent que le système proposé est plus efficace et moins coûteux. Même avec une chute de tension importante, la baisse de rendement est de 0,2 %, ce qui est bien inférieur à la perte de puissance d'un convertisseur élévateur classique, qui est d'environ 2 à 3 %. Pour évaluer la dynamique du compensateur hybride proposé, le système a été testé sous irradiation uniforme et non uniforme. Le compensateur suit les variations de tension avec un temps de

réponse inférieur à 20 ms, ce qui est acceptable au regard de la dynamique du PV. En outre, la structure proposée a été comparée à d'autres méthodes avec différents critères. La structure proposée offre un meilleur rendement et une meilleure réduction de l'ondulation de tension que la plupart des autres propositions de la littérature pour différentes puissances nominales. Elle a également le nombre minimum de composants à la puissance nominale et les constituants du compensateur sont dimensionnés à 15% de la puissance nominale.

Dans la troisième partie de ce travail, la surveillance et le diagnostic des défauts des modules PV ont été abordés. La méthode de diagnostic des défauts proposée est basée sur la spectroscopie d'impédance en ligne, sans équipement supplémentaire, et sans interrompre la production d'électricité. L'idée consiste à utiliser le circuit de découplage de puissance pulsée comme outil de spectroscopie d'impédance. Ce circuit à double fonction est un pont en H placé en série entre les panneaux photovoltaïques et l'onduleur principal. Il injecte une tension composée de deux composantes alternatives ; la tension d'ondulation responsable de l'atténuation de la puissance pulsée et la tension d'excitation destinée à l'estimation de l'impédance des panneaux PV. La tension d'excitation est injectée sur une plage de fréquence conforme à la dynamique des panneaux PV. L'amplitude est réglée pour minimiser les effets secondaires. Le contrôle du circuit proposé est effectué en utilisant des correcteurs PR et PI indépendants de l'onduleur principal. Les résultats ont montré que la puissance pulsée a été réduite de manière significative, et les paramètres des panneaux PV ont été estimés avec une erreur relative inférieure à 5%. Les résultats de la simulation ont également été comparés à l'analyse théorique de l'impédance. Ils ont montré que les paramètres des panneaux PV peuvent être estimés avec une erreur relative inférieure à 5%.

Concernant les travaux futurs, voici plusieurs propositions :

- Pour la conception des convertisseurs de puissance :

On pourrait envisager d'intégrer la puissance pulsée et le compensateur de chute de tension dans un seul convertisseur avec un nombre réduit de commutateurs et d'éléments. L'étage de puissance pulsée pourrait être remplacé par de nouveaux convertisseurs qui nécessitent moins de semi-conducteurs. La conception du compensateur pourrait également tirer parti de semi-

conducteurs à large bande interdite (SiC ou GaN) pour augmenter la fréquence de commutation. Cela pourrait améliorer le rendement et réduire la taille des éléments passifs.

Il serait également pertinent d'évaluer l'intégration de l'électronique IS avec le découplage de puissance et la compensation de chute de tension.

➤ Sur la commande des convertisseurs de puissance

Dans un premier temps, la robustesse du système de contrôle proposé aux variations des paramètres du modèle doit être évaluée plus en détail.

Il serait intéressant d'évaluer des méthodes de contrôle avancées du compensateur pour améliorer la capacité de réduction de l'ondulation de la tension. Cela conduirait à une réduction supplémentaire de la valeur du condensateur du lien continu. De plus, des filtres à base d'ondelettes à haute performance peuvent être développés pour extraire l'ondulation de tension avec une réponse dynamique très élevée.

Pour réduire le coût et augmenter la fiabilité, la tension continue d'entrée pourrait être estimée. Par conséquent, un capteur de tension peut être supprimé.

➤ Banc d'essai expérimental

Des expériences avec un émulateur PV et des panneaux PV doivent être menées pour évaluer plus précisément les performances de la proposition. Elles pourraient également permettre d'analyser l'effet du circuit de découplage sur le panneau PV.

La spectroscopie d'impédance pourrait également être évaluée sur le banc d'essai.

La méthode de diagnostic des défauts pourra être étendue à la classification de différents défauts du panneau PV.

## References

- [1] J. Conti, P. Holtberg, J. Diefenderfer, A. LaRose, J.T. Turnure, and L. Westfall, International energy outlook 2016 with projections to 2040, USDOE Energy Information Administration (EIA), Washington, DC United States, 2016.
- [2] M. Islam, S. Mekhilef, and M. Hasan, “Single phase transformerless inverter topologies for grid-tied photovoltaic system: A review,” *Renewable and Sustainable Energy Reviews*, vol. 45, pp. 69-86, 2015.
- [3] Y. Sun, Y. Liu, M. Su, W. Xiong, and J. Yang, “Review of active power decoupling topologies in single-phase systems,” *IEEE Transactions on Power Electronics*, vol. 31, no. 7, pp. 4778-4794, 2015.
- [4] T.F. Wu, C.H. Chang, L.C. Lin and C.L. Kuo, “Power loss comparison of single-and two-stage grid-connected photovoltaic systems,” *IEEE Transactions on Energy Conversion*, vol. 26, no. 2, pp. 707-715, 2011.
- [5] H.Wang, M. Liserre, and F. Blaabjerg, “Toward reliable power electronics: Challenges, design tools, and opportunities,” *IEEE Industrial Electronics Magazine*, vol. 7, no. 2, pp. 17-26, 2013.
- [6] M. H. Zare, M. Mohamadian, and R. Beiranvand, “A single-phase grid-connected photovoltaic inverter based on a three-switch three-port flyback with series power decoupling circuit,” *IEEE Transactions on Industrial Electronics*, vol. 64, no. 3, pp. 2062-2071, 2016.
- [7] M. K. Alam, F. Khan, J. Johnson and J. Flicker, “A comprehensive review of catastrophic faults in PV arrays: types, detection, and mitigation techniques,” *IEEE Journal of Photovoltaics*, vol. 5, no. 3, pp. 982-997, 2015.
- [8] Y. Zhao, J.-F. De Palma, J. Mosesian, R.Lyons, and B.Lehman, “Line–line fault analysis and protection challenges in solar photovoltaic arrays,” *IEEE transactions on Industrial Electronics*, vol. 60, no. 9, pp. 3784-3795, 2012.
- [9] S. Fadhel, “Efficacité énergétique et surveillance d’un microgrid à courant continu alimenté par des panneaux photovoltaïques,” Université Paris-Saclay; Ecole Nationale d’Ingénieurs de Sousse (Tunisie), 2020.

- [10] B. Li, "Health monitoring of photovoltaic modules using electrical measurements. Electric power," Université Paris-Saclay, 2021.
- [11] L. Hassaine, E. OLias, J. Quintero, and V. Salas, "Overview of power inverter topologies and control structures for grid connected photovoltaic systems," *Renewable and Sustainable Energy Reviews*, vol. 30, pp. 796-807, 2014.
- [12] R. A. Mastromauro, M. Liserre, and A. Dell'Aquila, "Control issues in single-stage photovoltaic systems: MPPT, current and voltage control," *IEEE Transactions on Industrial Informatics*, vol. 8, no. 2, pp. 241-254, 2012.
- [13] A. R. Reisi, M. H. Moradi, and S. Jamasb, "Classification and comparison of maximum power point tracking techniques for photovoltaic system: A review," *Renewable and sustainable energy reviews*, vol. 19, pp. 433-443, 2013.
- [14] B. Subudhi and R. Pradhan, "A comparative study on maximum power point tracking techniques for photovoltaic power systems," *IEEE transactions on Sustainable Energy*, vol. 4, no. 1, pp. 89-98, 2012.
- [15] T. T. Khatib, A. Mohamed, N. Amin, and K. Sopian, "An efficient maximum power point tracking controller for photovoltaic systems using new boost converter design and improved control algorithm," *WSEAS Transactions on power systems*, vol. 5, no. 2, pp. 53-63, 2010.
- [16] M. A. Masoum, H. Dehbonei, and E. F. Fuchs, "Theoretical and experimental analyses of photovoltaic systems with voltage and current-based maximum power-point tracking," *IEEE Transactions on energy conversion*, vol. 17, no. 4, pp. 514-522, 2002.
- [17] J. Schoeman and J. Van Wyk, "A simplified maximal power controller for terrestrial photovoltaic panel arrays," *In 1982 IEEE Power Electronics Specialists conference*, pp. 361-367. *IEEE*, 1982.
- [18] J.A. Jiang, T.L. Huang, Y.T. Hsiao, and C.H. Chen, "Maximum power tracking for photovoltaic power systems," *Journal of Applied Science and Engineering*, vol. 8, no. 2, pp. 147-153, 2005.
- [19] O. López-Lapeña, M. T. Penella, and M. Gasulla, "A new MPPT method for low-power solar energy harvesting," *IEEE Transactions on industrial electronics*, vol. 57, no. 9, pp. 3129-3138, 2009.

- [20] V. Salas, E. Olias, A. Lazaro, and A. Barrado, "Evaluation of a new maximum power point tracker (MPPT) applied to the photovoltaic stand-alone systems," *Solar energy materials and solar cells*, vol. 87, no. 1-4, pp. 807-815, 2005.
- [21] K. Tse, M. Ho, H.-H. Chung, and S. Hui, "A novel maximum power point tracker for PV panels using switching frequency modulation," *IEEE transactions on power electronics*, vol. 17, no. 6, pp. 980-989, 2002.
- [22] C. Hua, J. Lin, and C. Shen, "Implementation of a DSP-controlled photovoltaic system with peak power tracking," *IEEE transactions on industrial electronics*, vol. 45, no. 1, pp. 99-107, 1998.
- [23] C. W. Tan, T. C. Green, and C. A. Hernandez-Aramburo, "An improved maximum power point tracking algorithm with current-mode control for photovoltaic applications," In *2005 International Conference on Power Electronics and Drives Systems* (Vol. 1, pp. 489-494). IEEE.
- [24] V. Salas, E. Olias, A. Lazaro, and A. Barrado, "New algorithm using only one variable measurement applied to a maximum power point tracker," *Solar energy materials and solar cells*, vol. 87, no. 1-4, pp. 675-684, 2005.
- [25] Y. C. Kuo, T. J. Liang, and J. F. Chen, "Novel maximum-power-point-tracking controller for photovoltaic energy conversion system," *IEEE transactions on industrial electronics*, vol. 48, no. 3, pp. 594-601, 2001.
- [26] Y. Zhang, J. Long, Y. Zhang, T. Lu, Z. Zhao, and L. Jin, "Table-based direct power control for three-level neutral point-clamped pulse-width modulated rectifier," *IET Power Electronics*, vol. 6, no. 8, pp. 1555-1562, 2013.
- [27] M. Monfared, M. Sanatkar, and S. Golestan, "Direct active and reactive power control of single-phase grid-tie converters," *IET Power Electronics*, vol. 5, no. 8, pp. 1544-1550, 2012.
- [28] W. Song, J. Ma, L. Zhou, and X. Feng, "Deadbeat predictive power control of single-phase three-level neutral-point-clamped converters using space-vector modulation for electric railway traction," *IEEE Transactions on power electronics*, vol. 31, no. 1, pp. 721-732, 2015.

- [29] B. Liu, W. Song, J. Ma, X. Feng, and W. Li, "Dynamic performance improvement of single-phase PWM converters with power hysteresis control scheme," *IET Power Electronics*, vol. 11, no. 12, pp. 1894-1902, 2018.
- [30] J. Hu, L. Shang, Y. He, and Z. Zhu, "Direct active and reactive power regulation of grid-connected DC/AC converters using sliding mode control approach," *IEEE transactions on power electronics*, vol. 26, no. 1, pp. 210-222, 2010.
- [31] M. Ciobotaru, R. Teodorescu, and F. Blaabjerg, "A new single-phase PLL structure based on second order generalized integrator," *In 2006 37th IEEE Power Electronics Specialists Conference*, pp. 1-6. IEEE, 2006.
- [32] V. Vapnik, *The nature of statistical learning theory*, Springer-Verlag, New York, 1995.
- [33] M. A. Fnaiech, M. Trabelsi, S. Khalil, M. Mansouri, H. Nounou, and H. Abu-Rub, "Robust sliding mode control for three-phase rectifier supplied by non-ideal voltage," *Control Engineering Practice*, vol. 77, pp. 73-85, 2018.
- [34] M. Pichan and H. Rastegar, "Sliding-mode control of four-leg inverter with fixed switching frequency for uninterruptible power supply applications," *IEEE Transactions on Industrial Electronics*, vol. 64, no. 8, pp. 6805-6814, 2017.
- [35] M. Zhihong, A. P. Paplinski, and H. R. Wu, "A robust MIMO terminal sliding mode control scheme for rigid robotic manipulators," *IEEE transactions on automatic control*, vol. 39, no. 12, pp. 2464-2469, 1994.
- [36] S. K. Gudey and R. Gupta, "Recursive fast terminal sliding mode control in voltage source inverter for a low-voltage microgrid system," *IET Generation, Transmission & Distribution*, vol. 10, no. 7, pp. 1536-1543, 2016.
- [37] X. Yu and M. Zhihong, "Fast terminal sliding-mode control design for nonlinear dynamical systems," *IEEE Transactions on Circuits and Systems I: Fundamental Theory and Applications*, vol. 49, no. 2, pp. 261-264, 2002.
- [38] X. Yu, M. Zhihong, and Y. Wu, "Terminal sliding modes with fast transient performance," *In Proceedings of the 36th IEEE Conference on Decision and Control*, vol. 2, pp. 962-963. IEEE, 1997.
- [39] A. R. Gautam, D. M. Fulwani, R. R. Makineni, A.K. Rathore, and D. Singh, "Control strategies and power decoupling topologies to mitigate  $2\omega$ -ripple in single-phase inverters: a review and open challenges," *IEEE Access*, vol. 8, pp. 147533-147559, 2020.

- [40] P. T. Krein, R. S. Balog, and M. Mirjafari, "Minimum energy and capacitance requirements for single-phase inverters and rectifiers using a ripple port," *IEEE Transactions on Power Electronics*, vol. 27, no. 11, pp. 4690-4698, 2012.
- [41] R.J. Wai and C.Y. Lin, "Active low-frequency ripple control for clean-energy power-conditioning mechanism," *IEEE Transactions on Industrial Electronics*, vol. 57, no. 11, pp. 3780-3792, 2010.
- [42] R. Wang, F.Wang, D. Boroyevich, R. Burgos, R. Lai, P. Ning, and K. Rajashekara , "A high power density single-phase PWM rectifier with active ripple energy storage," *IEEE Transactions on Power Electronics*, vol. 26, no. 5, pp. 1430-1443, 2010.
- [43] M. Jang and V. G. Agelidis, "A minimum power-processing-stage fuel-cell energy system based on a boost-inverter with a bidirectional backup battery storage," *IEEE Transactions on Power Electronics*, vol. 26, no. 5, pp. 1568-1577, 2010.
- [44] M. Jang, M. Ciobotaru, and V. G. Agelidis, "A single-stage fuel cell energy system based on a buck--boost inverter with a backup energy storage unit," *IEEE transactions on power electronics*, vol. 27, no. 6, pp. 2825-2834, 2011.
- [45] H. Valipour, G. Rezaadeh, and M. R. Zolghadri, "Flicker-free electrolytic capacitor-less universal input offline LED driver with PFC," *IEEE Transactions on Power Electronics*, vol. 31, no. 9, pp. 6553-6561, 2015.
- [46] A. Kyritsis, N. Papanikolaou, and E. Tatakis, "A novel parallel active filter for current pulsation smoothing on single stage grid-connected AC-PV modules." In *2007 European Conference on Power Electronics and Applications*, pp. 1-10. IEEE, 2007.
- [47] S.Y. Lee, Y.L. Chen, Y.M. Chen, and K.H Liu, "Development of the active capacitor for PFC converters." In *2014 IEEE Energy Conversion Congress and Exposition (ECCE)*, pp. 1522-1527. IEEE, 2014.
- [48] W. Cai, B. Liu, S. Duan, and L. Jiang, , "An active low-frequency ripple control method based on the virtual capacitor concept for BIPV systems," *IEEE Transactions on Power Electronics*, vol. 29, no. 4, pp. 1733-1745, 2013.
- [49] P. Nandi, and R. Adda, "Integration of boost-type active power decoupling topology with single-phase switched boost inverter," *IEEE Transactions on Power Electronics*, vol. 35, no. 11, pp. 11965-11975, 2020.

- [50] S. Wang, X. Ruan, K. Yao, S.C. Tan, , Y. Yang, and Z. Ye, "A flicker-free electrolytic capacitor-less AC–DC LED driver," *IEEE Transactions on Power Electronics*, vol. 27, no. 11, pp. 4540-4548, 2011.
- [51] X. Cao, Q.-C. Zhong, and W.-L. Ming, "Ripple eliminator to smooth DC-bus voltage and reduce the total capacitance required," *IEEE Transactions on Industrial Electronics*, vol. 62, no. 4, pp. 2224-2235, 2014.
- [52] S. Xu, L. Chang, and R. Shao, "Single-phase voltage source inverter with voltage boosting and power decoupling capabilities," *IEEE Journal of Emerging and Selected Topics in Power Electronics*, vol. 8, no. 3, pp. 2977-2988, 2019.
- [53] S. K. Mazumder, R. K. Burra, and K. Acharya, "A ripple-mitigating and energy-efficient fuel cell power-conditioning system," *IEEE Transactions on Power Electronics*, vol. 22, no. 4, pp. 1437-1452, 2007.
- [54] Y. Tang, Z. Qin, F. Blaabjerg, and P. C. Loh, "A dual voltage control strategy for single-phase PWM converters with power decoupling function," *IEEE Transactions on Power Electronics*, vol. 30, no. 12, pp. 7060-7071, 2014.
- [55] W. Liu, K. Wang, H. S.-h. Chung, and S. T.-h. Chuang, "Modeling and design of series voltage compensator for reduction of DC-link capacitance in grid-tie solar inverter," *IEEE Transactions on Power Electronics*, vol. 30, no. 5, pp. 2534-2548, 2014.
- [56] H. Wang, H. S.-H. Chung, and W. Liu, "Use of a series voltage compensator for reduction of the DC-link capacitance in a capacitor-supported system," *IEEE Transactions on Power Electronics*, vol. 29, no. 3, pp. 1163-1175, 2013.
- [57] R. Chen, Y. Liu, and F. Z. Peng, "DC capacitor-less inverter for single-phase power conversion with minimum voltage and current stress," *IEEE Transactions on Power Electronics*, vol. 30, no. 10, pp. 5499-5507, 2014.
- [58] H. Li, K. Zhang, H. Zhao, S. Fan, and J. Xiong, "Active power decoupling for high-power single-phase PWM rectifiers," *IEEE Transactions on Power Electronics*, vol. 28, no. 3, pp. 1308-1319, 2012.
- [59] Y. Tang and F. Blaabjerg, "A component-minimized single-phase active power decoupling circuit with reduced current stress to semiconductor switches," *IEEE Transactions on Power Electronics*, vol. 30, no. 6, pp. 2905-2910, 2014.

- [60] W. Cai, L. Jiang, B. Liu, S. Duan, and C. Zou, "A power decoupling method based on four-switch three-port DC/DC/AC converter in DC microgrid," *IEEE Transactions on Industry Applications*, vol. 51, no. 1, pp. 336-343, 2014.
- [61] I. Serban, "Power decoupling method for single-phase H-bridge inverters with no additional power electronics," *IEEE Transactions on Industrial Electronics*, vol. 62, no. 8, pp. 4805-4813, 2015.
- [62] T. Shimizu, T. Fujita, G. Kimura, and J. Hirose, "A unity power factor PWM rectifier with DC ripple compensation," *IEEE Transactions on industrial electronics*, vol. 44, no. 4, pp. 447-455, 1997.
- [63] T. Fuyuki, and A. Kitiyanan, "Photographic diagnosis of crystalline silicon solar cells utilizing electroluminescence," *Applied Physics A*, vol. 96, no. 1, pp. 189-196, 2009.
- [64] D. Hinken, K. Ramspeck, K. Bothe, B. Fischer, and R. Brendel, "Series resistance imaging of solar cells by voltage dependent electroluminescence," *Applied Physics Letters*, vol. 91, no. 18, pp. 182104, 2007.
- [65] F. Ancuta, and C. Cepisca, "Fault analysis possibilities for PV panels." In *Proceedings of the 2011 3rd International Youth Conference on Energetics (IYCE)*, pp. 1-5. IEEE, 2011.
- [66] B. Du, Y. He, Y. He, and C. Zhang, "Progress and trends in fault diagnosis for renewable and sustainable energy system based on infrared thermography: A review," *Infrared Physics & Technology*, vol. 109, pp. 103383, 2020.
- [67] V. Sharma, O. Sastry, A. Kumar, B. Bora, and S.S. Chandel, "Degradation analysis of a-Si, (HIT) hetero-junction intrinsic thin layer silicon and mC-Si solar photovoltaic technologies under outdoor conditions," *Energy*, vol. 72, pp. 536-546, 2014.
- [68] D. S. Pillai, and N. Rajasekar, "A comprehensive review on protection challenges and fault diagnosis in PV systems," *Renewable and Sustainable Energy Reviews*, vol. 91, pp. 18-40, 2018.
- [69] S. Fadhel, C. Delpha, D. Diallo, I. Bahri, A. Migan, M. Trabelsi, and M.F. Mimouni, "PV shading fault detection and classification based on IV curve using principal component analysis: Application to isolated PV system," *Solar Energy*, vol. 179, pp. 1-10, 2019.

- [70] B. Li, A. Migan-Dubois, C. Delpha, and D. Diallo, "Evaluation and improvement of IEC 60891 correction methods for IV curves of defective photovoltaic panels," *Solar Energy*, vol. 216, pp. 225-237, 2021.
- [71] T. Takashima, J. Yamaguchi, and M. Ishida, "Fault detection by signal response in PV module strings." In *2008 33rd IEEE Photovoltaic Specialists Conference*, pp. 1-5. IEEE, 2008.
- [72] M. K. Alam, F. H. Khan, J. Johnson and J. Flicker, "PV arc-fault detection using spread spectrum time domain reflectometry (SSTDR)." In *2014 IEEE energy conversion congress and exposition (ECCE)* (pp. 3294-3300). IEEE.
- [73] A. Y. Appiah, X. Zhang, B. B. K. Ayawli and F. Kyeremeh, , "Review and performance evaluation of photovoltaic array fault detection and diagnosis techniques," *International Journal of Photoenergy*, vol. 2019, 2019.
- [74] E. Barsoukov, and J. R. Macdonald, *Impedance spectroscopy: theory, experiment, and applications: John Wiley & Sons*, 2018.
- [75] I. Mora-Sero, G. Garcia-Belmonte, P. P. Boix, M.A. Vazquez, and J. Bisquert, "Impedance spectroscopy characterisation of highly efficient silicon solar cells under different light illumination intensities," *Energy & Environmental Science*, vol. 2, no. 6, pp. 678-686, 2009.
- [76] M. Suresh, "Measurement of solar cell parameters using impedance spectroscopy," *Solar Energy Materials and Solar Cells*, vol. 43, no. 1, pp. 21-28, 1996.
- [77] N. Katayama, S. Osawa, S. Matsumoto, T. Nakano, and M. Sugiyama, "Degradation and fault diagnosis of photovoltaic cells using impedance spectroscopy," *Solar Energy Materials and Solar Cells*, vol. 194, pp. 130-136, 2019.
- [78] C.H. Huang, Y.H. Liao, C.M. Chu, J.C. Chou, Y.J. Lin, and Y.H. Nien, "Analysis of different dye-sensitized solar cell models by electrochemical impedance spectroscopy." In *2015 IEEE International Conference on Electron Devices and Solid-State Circuits (EDSSC)*, pp. 29-32. IEEE, 2015.
- [79] T. Yeow, J. Sun, Z. Yao et al., "Evaluation of impedance spectroscopy as a tool to characterize degradation mechanisms in silicon photovoltaics," *Solar Energy*, vol. 184, pp. 52-58, 2019.

- [80] O. I. Olayiwola, and P. S. Barendse, "Photovoltaic Cell/Module Equivalent Electric Circuit Modeling Using Impedance Spectroscopy," *IEEE Transactions on Industry Applications*, vol. 56, no. 2, pp. 1690-1701, 2019.
- [81] D. Chenvidhya, K. Kirtikara, and C. Jivacate, "A new characterization method for solar cell dynamic impedance," *Solar Energy Materials and Solar Cells*, vol. 80, no. 4, pp. 459-464, 2003.
- [82] D. Chenvidhya, K. Kirtikara, and C. Jivacate, "PV module dynamic impedance and its voltage and frequency dependencies," *Solar Energy Materials and Solar Cells*, vol. 86, no. 2, pp. 243-251, 2005.
- [83] M. Shanmugam, and M. F. Baroughi, "Characterization of interfacial charge transport and recombination by impedance spectroscopy on SiO<sub>2</sub> coated TiO<sub>2</sub> based dye sensitized solar cells." In *2011 37th IEEE Photovoltaic Specialists Conference*, pp. 002656-002660. IEEE, 2011.
- [84] C.-H. Huang, Y.-H. Liao, C.-M. Chu, J.C. Chou, Y.J. Lin, and Y.H. Nien, "Analysis of different dye-sensitized solar cell models by electrochemical impedance spectroscopy." In *2015 IEEE International Conference on Electron Devices and Solid-State Circuits (EDSSC)*. IEEE. pp. 29-32.
- [85] M. A. Varnosfaderani, and D. Strickland, "Online Electrochemical Impedance Spectroscopy (EIS) estimation of a solar panel," *Vacuum*, vol. 139, pp. 185-195, 2017.
- [86] M. Shahparasti, M. Mohamadian, A. Yazdian, AA. Ahmad, M. Amini, "Derivation of a stationary-frame single-loop controller for three-phase standalone inverter supplying nonlinear loads," *IEEE transactions on power electronics*, vol. 29, no. 9, pp. 5063-5071, 2013.
- [87] V. I. Utkin, *Sliding modes in control and optimization*. Springer Science & Business Media, 2013.
- [88] J.J. E. Slotine and W. Li, *Applied nonlinear control* (no. 1). Prentice hall Englewood Cliffs, NJ, 1991.
- [89] M. Pichan, A. A. Ahamad, A. Arishamifar, and M. E. Jamarani, "A straightforward procedure to select passive elements in single-phase pulse-width modulation rectifiers with developed resonant current controller," *Electric Power Components and Systems*, vol. 44, no. 4, pp. 379-389, 2016.

- [90] C.-T. Lee, Y.-M. Chen, L.-C. Chen, and P.-T. Cheng, "Efficiency improvement of a DC/AC converter with the power decoupling capability," in 2012 Twenty-Seventh Annual IEEE Applied Power Electronics Conference and Exposition (APEC), 2012: IEEE, pp. 1462-1468.
- [91] A. A. Ahmad, M. Pichan, and A. Abrishamifar, "A new simple structure PLL for both single and three phase applications," *International Journal of Electrical Power & Energy Systems*, vol. 74, pp. 118-125, 2016.
- [92] D.-H. Hwang, J.-Y. Lee, and Y. Cho, "Single-phase single-stage dual-buck photovoltaic inverter with active power decoupling strategy," *Renewable energy*, vol. 126, pp. 454-464, 2018.
- [93] S. Xie, Y. Sun, J. Lin, X. Li, M. Su, Y. Liu, and W. Xiong, "Adaptive Power Decoupling Control for Single-Phase Converter with Unbalanced DC-Split-Capacitor Circuit," *IEEE Transactions on Power Electronics*, 2021.
- [94] J. Xu, T. B. Soeiro, F. Gao, H. Tang, and P. Bauer, "Carrier-based Generalized Discontinuous PWM Strategy for Single-Phase Three-Legs Active Power Decoupling Converters," *IEEE Transactions on Industrial Electronics*, 2020.
- [95] H. Tian, F. Mancilla-David, K. Ellis, E. Muljadi, and P. Jenkins, "A cell-to-module-to-array detailed model for photovoltaic panels," *Solar energy*, vol. 86, no. 9, pp. 2695-2706, 2012.
- [96] M. G. Villalva, J. R. Gazoli, and E. Ruppert Filho, "Comprehensive approach to modeling and simulation of photovoltaic arrays," *IEEE Transactions on power electronics*, vol. 24, no. 5, pp. 1198-1208, 2009.
- [97] K. A. Kim, C. Xu, L. Jin, and P. T. Krein, "A dynamic photovoltaic model incorporating capacitive and reverse-bias characteristics," *IEEE Journal of photovoltaics*, vol. 3, no. 4, pp. 1334-1341, 2013.